Modes, transient dynamics and forced response of circular jets

Xavier Garnaud

École Polytechnique
Laboratoire d'Hydrodynamique

Thèse présentée pour obtenir le grade de

DOCTEUR DE L'ÉCOLE POLYTECHNIQUE

Spécialité : Mécanique

par

Xavier GARNAUD

Modes, transient dynamics and forced response of circular jets*

*Modes, dynamique transitoire et réponse forcée dans les jets circulaires

Thèse soutenue le 28 juin 2012 devant le jury composé de

Peter Monkewitz	rapporteur	EPFL
Nigel Peake	rapporteur	University of Cambridge
Dan Henningson	président du jury	KTH
Laurette Tuckerman	examinatrice	ESPCI
Patrick Huerre	directeur de thèse	Ecole Polytechnique
Peter Schmid	directeur de thèse	Ecole Polytechnique
Lutz Lesshafft	directeur de thèse	Ecole Polytechnique
François Gallaire	invité	EPFL

Summary

The linear stability of axisymmetric jets is studied in a global framework, such that the geometry and the non-parallelism of the base flow are fully accounted for. In order to characterize the "preferred mode" of the jet, which is consistently observed in experiments and numerical simulations, different types of analyses are carried out. As a well-known conjecture ascribes the existence of this "preferred mode" to a resonance between external noise and the least-stable eigenmode, a modal study is first performed. This analysis prompted the development of a new numerical method allowing an efficient treatment of compressible flows; however, the results indicate that a modal representation is not well-suited for a description of the dynamics of convection-dominated stable flows. Studies of simplified model problems are presented that underpin this conclusion. Instead, the instability dynamics of such flows are characterized in a consistent manner in terms of optimal initial perturbations and optimal harmonic forcing. The latter approach robustly reproduces experimental observations with regard to the frequency and the spatial structure of the jet "preferred mode". Furthermore, the results allow an interpretation of this global wavepacket structure as a cooperation of different families of local instability modes. The present analysis demonstrates that the "preferred mode" does not arise from resonance with an eigenmode, but rather is to be interpreted as a pseudo-resonance.

Résumé

La stabilité linéaire des jets axisymétriques est étudiée dans un contexte global, c'est à dire en prenant en compte sans approximation la géométrie et le non-parallélisme de l'écoulement. Afin de caractériser le mode préféré du jet observé expérimentalement et numériquement, différentes analyses ont été mises en oeuvre. Une conjecture étant que ces structures à une résonance entre des perturbations extérieures et le mode propre le moins atténué, une analyse modale de l'écoulement a tout d'abord été effectuée. Cette étude a demandé la mise au point d'une méthode numérique spécifique pour pouvoir traiter les écoulements compressibles de manière efficace. Cependant, les résultats ont montré qu'une représentation modale n'est pas adaptée pour décrire la dynamique des écoulements stable dominés par l'advection. Des modèles simplifiés permettant de mieux comprendre les limites de cette approche sont présentés. Cette dynamique peut cependant tre caractérisée par le calcul des perturbations optimales et du forage harmonique optimal. Cette dernière approche reproduit de manière robuste les observations expérimentales concernant la fréquence et la structure spatiale du mode préféré. La structure de ce paquet d'onde global est interprétée comme provenant de la coopération entre différentes familles de modes locaux. L'analyse présentée dans cette thèse montre que le mode préféré du jet ne vient pas de la résonance d'un mode propre, mais qu'il s'agit en fait d'une pseudo-résonance.

Remerciements

Je souhaite tout d'abord remercier mes directeurs de thèse qui m'ont accueilli au LadHyX pour effectuer cette thèse. Patrick a toujours été disponible et impliqué au cours de ces trois années et demie, et est resté positif même quand je m' enfonçais toujours plus profondément dans ce qui ressemblait fort à des impasses. A chacune de mes tentatives, Peter m'a soutenu par son fameux "sounds good"! Et enfin Lutz a été présent pour discuter et m'aider lors des mes doutes et des mes espoirs quasi-quotidiens; c'est aussi essentiellement grâce à lui que j'ai pu me cultiver sur la mécanique des fluides à Stockholm, Munich, Los Angeles, Bad Reicheinhall, Honolulu, Besançon, Orsay, Montestigliano et Pékin.

Durant cette thèse j'ai aussi bénéficié de l'aide de Jean-Marc, sans qui je n'aurais sûrement pas pu calculer de modes compressibles (rétrospectivement, ca n'aurait pas été très grave) et de François, qui m'a expliqué la stabilité et guidé à plusieurs reprises, et qui a relu toutes les lignes de cette thèse.

Je remercie aussi Peter Monkewitz, Nigel Peake, Dan Henningson, Laurette Tuckermann et François Gallaire d'avoir accepté de faire partie de mon jury.

Merci à Miguel de m'avoir montré qu'on ne va pas loin avec un programme 100 % fait maison, et de m'avoir fait utiliser des bibliothèques modernes... Comme quoi on peut quand même faire confiance à un adepte de la gonflette. Pour rester dans le registre de l'informatique (mais sans les gros bras), je souhaite remercier Daniel dont l'un des multiples talents est de nous permettre de faire tourner nos calculs.

J'aimerais aussi remercier ceux pour qui j'ai enseigné: Sabine Ortiz à l'ENSTA et Olivier Gicquel, Thierry Schuller, Franck Richecoeur, Marc Massot et Frédérique Laurent à Centrale.

Je garderai un très bon souvenir de l'ambiance au LadHyX. Je tiens donc à remercier toutes les personnes que j'y ai croisé et qui ne sont pas déjà mentionnées: celles font de l'escalade (Philippe, Cristóbal, Rémi, Diego, Jon, Clément, Dimitry et Nicolas), celles qui font tourner le laboratoire (Antoine, Thérèse, Sandrine, Judith, Delphine et Alexandre) et les autres (Fabien, Cécile, Franz, Gianluca, Sébastien et Christophe pour ne citer qu'eux).

Enfin merci à ma famille et *Silvia, obrigado pelo apoio.*

Contents

Chapter 1

Introduction.

1.1 Forced and natural isothermal jets.

Isothermal jet flows are typical noise amplifiers, meaning that in an ideal situation the flow would be steady but in practice external perturbations even at low levels are amplified by the flow. These disturbances may be hydrodynamic, e.g. coming from the fan in an experiment, acoustic, or produced by the vibrations of the jet pipe. For a given configuration, if the velocity of a jet U_0 is gradually increased, the behavior of the structures excited in the jet varies. The flow is initially laminar, with large-scale oscillations, as schematically represented in figure 1.1($a-d$). As the Reynolds number based on the initial jet radius R increases, the initially laminar flow experiences a transition to turbulence further downstream, as shown in figure 1.1(e). For even higher jet velocities it becomes difficult to identify coherent flow structures in unforced (or natural) jets where perturbations are driven by the background noise. "Orderly structure in jet turbulence" (Crow and Champagne 1971) can however be observed for Reynolds numbers of the order of 10^4 to 10^6 when a low level of controlled forcing is applied to the flow, as also demonstrated by Moore (1977).

Perturbations in jet flows develop on top of a strongly non-parallel mean velocity profile characterized by several length scales. The jet issues from a cylindrical pipe of radius R, and the flow inside this pipe is characterized by a boundary layer momentum thickness θ_0. In practice, θ_0 is tens or hundreds of times smaller than R. The mean flow in the free-jet region, schematically described in figure 1.2, is such that the thickness θ of the shear layer, which is initially of the order of θ_0 at the nozzle, increases linearly in the streamwise direction over approximately eight jet radii. This region where the centerline velocity remains approximately equal to the exit velocity U_0 is referred to as

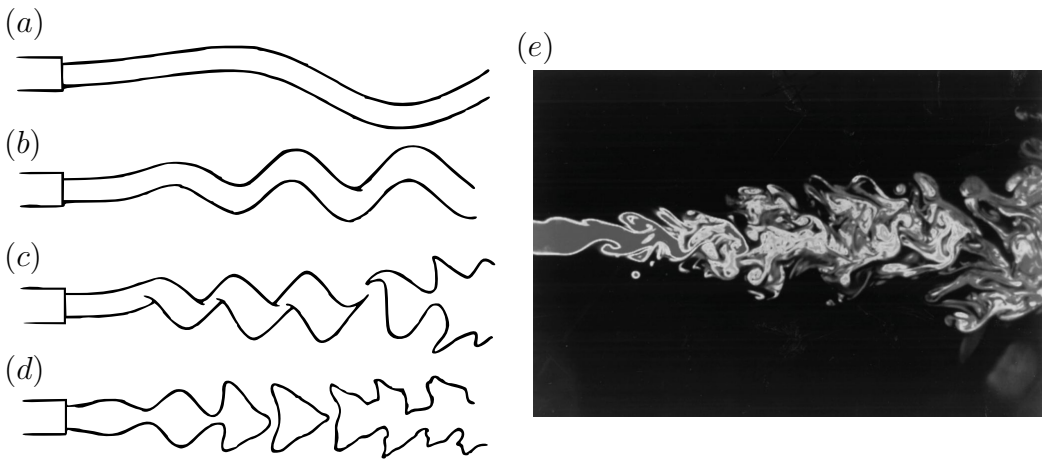

Figure 1.1: $(a-d)$: Schematic evolution of the jet instability as Re increases from values of the order of 100 to values of the order of 1000. Picture taken from Crow and Champagne (1971). (e): dye visualization of a water jet at $Re \approx 2000$. Image taken from Prasad and Sreenivasan (1990).

the *potential core*. At the end of the potential core the shear layer thickness is of order R, and further downstream velocity profiles are approximately Gaussian and the centerline velocity begins to decrease.

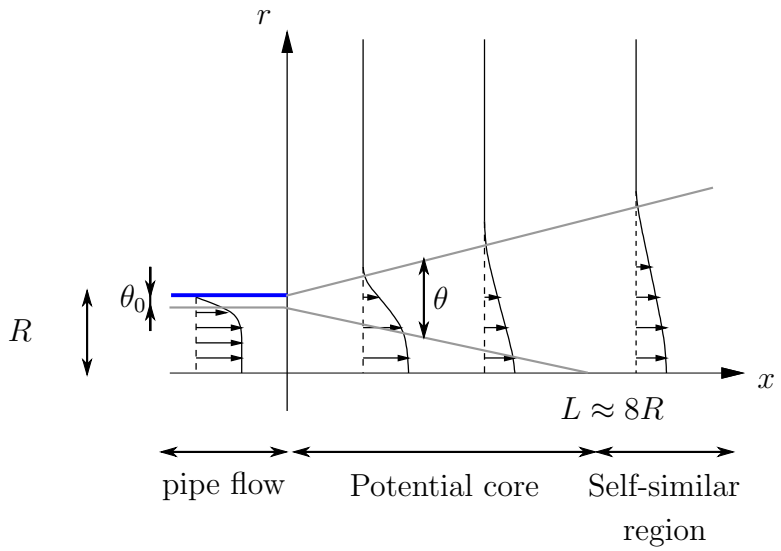

Figure 1.2: Schematic representation of a mean turbulent jet flow. The jet pipe, of radius R, is represented by the thick blue line. Gray lines represent the limits of the boundary layer in the pipe and of the shear layer in the free-jet.

As described by Crighton (1981), two main types of instabilities, characterized by different time and space scales, are usually found in isothermal jet flows. First is the shear-layer instability that develops on the scale of the shear layer momentum thickness θ. Michalke (1971) showed that the typical frequency f of this instability (the frequency at which the associated spatial growth rate is maximum) is characterized by a Strouhal number based on the shear layer thickness $St_{\theta_0} \equiv f\theta_0/U_0 \approx 0.017$, and that the corresponding wave length is of the order of θ. In natural jets, the size of these structures in the azimuthal direction may range from the order of θ_0 to the order of R. Due to the rapid variation of the shear layer thickness, such an instability wave can only be sustained near the exit of the pipe. This mechanism may however generate large scale oscillations through non-linear processes. Kibens (1980) performed an experiment where a jet is forced at a frequency close to that of the most amplified shear-layer instability at the nozzle. The vortex passage frequency at different streamwise locations is displayed in figure 1.3. It appears that successive vortex pairings cause the frequency to be halved several times until the Strouhal number based on the jet diameter, $St_D = fD/U_0$, is of the order 0.4. The frequency decreases through discrete steps roughly as $1/x$, i.e. as $1/\theta$, so that the local Strouhal number St_θ remains of the same order of magnitude through the potential core.

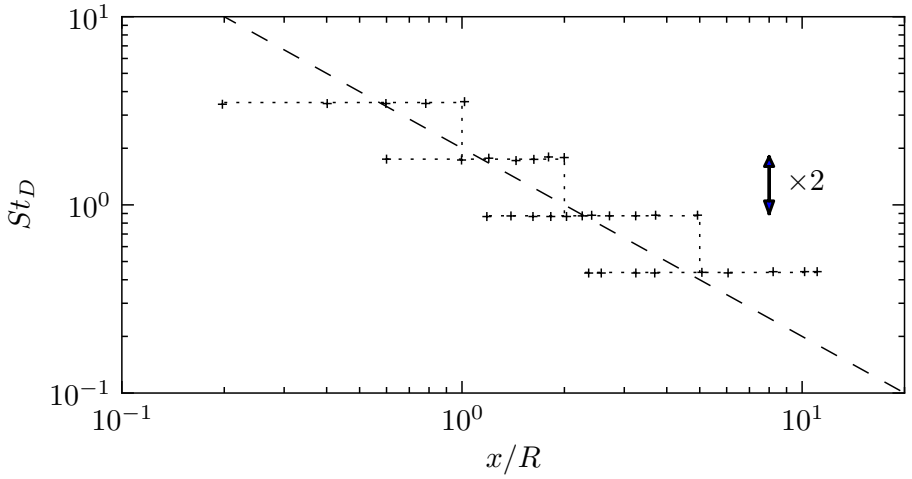

Figure 1.3: Vortex passage frequency in the shear layer in the forced jet experiment performed by Kibens (1980), as a function of the downstream direction (+ symbols). The dashed line, $St_D = D/x$, corresponds to the vortex pairing model of Laufer and Monkewitz (1980). Data taken from Ho and Huerre (1984).

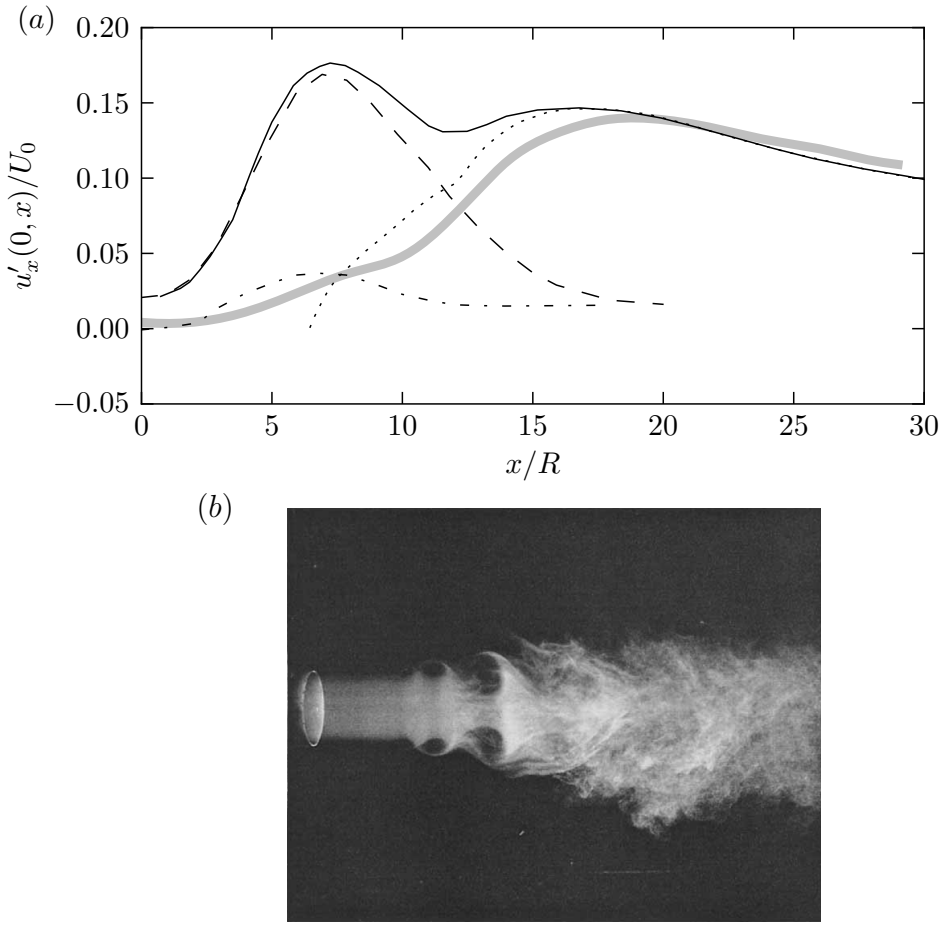

Figure 1.4: (a): Velocity fluctuations on the centerline of an incompressible jet: comparison between an unforced case (thick gray line) and a forced case at $St_D = 0.3$ (thin solid line). For the latter case, the dashed line corresponds to the fluctuations at $St_D = 0.3$, the dash-dotted line to the fluctuations at $St_D = 0.6$ and the dotted line to the rest. (b): smoke visualization of the flow response to a forcing at $St_D = 0.3$. Data taken from Crow and Champagne (1971).

A different behavior has been observed in the experiments of Crow and Champagne (1971). In this case forcing is applied at lower frequencies, for Strouhal numbers based on the jet diameter ranging from 0.15 to 0.6. The amplitude of velocity fluctuations measured on the jet axis is displayed in figure 1.4(a) for a forcing at $St_D = 0.3$. Results indicate that the dominant frequency of the flow response, shown in figure 1.4(b), remains equal to the forcing frequency throughout the potential core. The authors report that

optimal excitation of these flow structures occurs for $St_D \approx 0.3$. This type of unstable structures is referred to as the *preferred mode* or *jet-column* mode. The preferred frequency varies depending on the experimental conditions as well as on the physical quantity measured to evaluate the amplification: Moore (1977), who performed experiments at low forcing levels so that non-linear effects are weak, reports an optimal Strouhal number of 0.5 for velocity fluctuations and 0.45 for pressure fluctuations. Gutmark and Ho (1983) review results from a dozen of experiments that find values ranging from 0.3 to 0.6. Figure 1.5 shows that the preferred Strouhal number is also observed in natural jets, i.e. when no controlled forcing is applied and only the incoming noise is amplified. The azimuthal distribution of this jet column mode is dominated by azimuthal wavenumbers $m = 0, 1$ and 2 as the typical size of the vortical structures is of the order of the jet radius (see Parekh et al. (1988) for helical forcing).

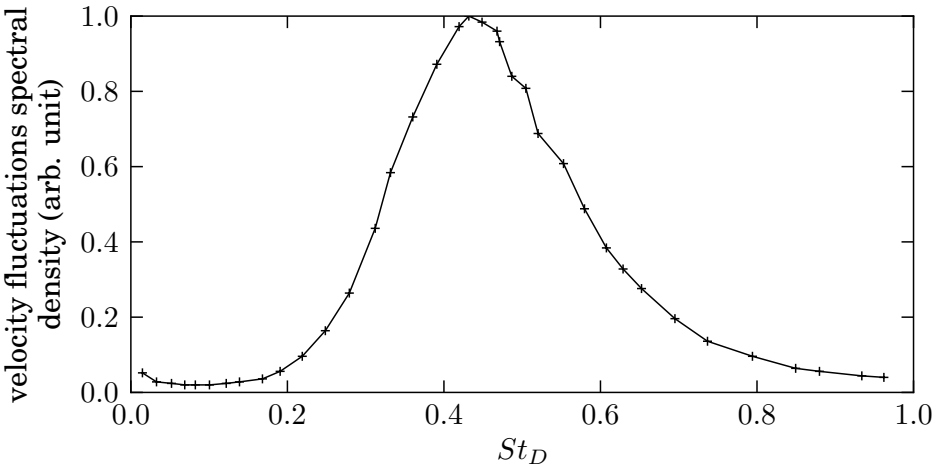

Figure 1.5: Fourier spectrum of velocity fluctuations in an incompressible natural jet on the centerline at $x = 8R$. Data taken from Crow and Champagne (1971).

1.2 Sound radiation from subsonic jets.

Acoustic radiation from subsonic jets has extensively been studied both experimentally and numerically. Figure 1.6 displays instantaneous contours of the acoustic field radiated by natural subsonic jets obtained in numerical simulations. The acoustic far-field exhibits a wide variety of wave-lengths as

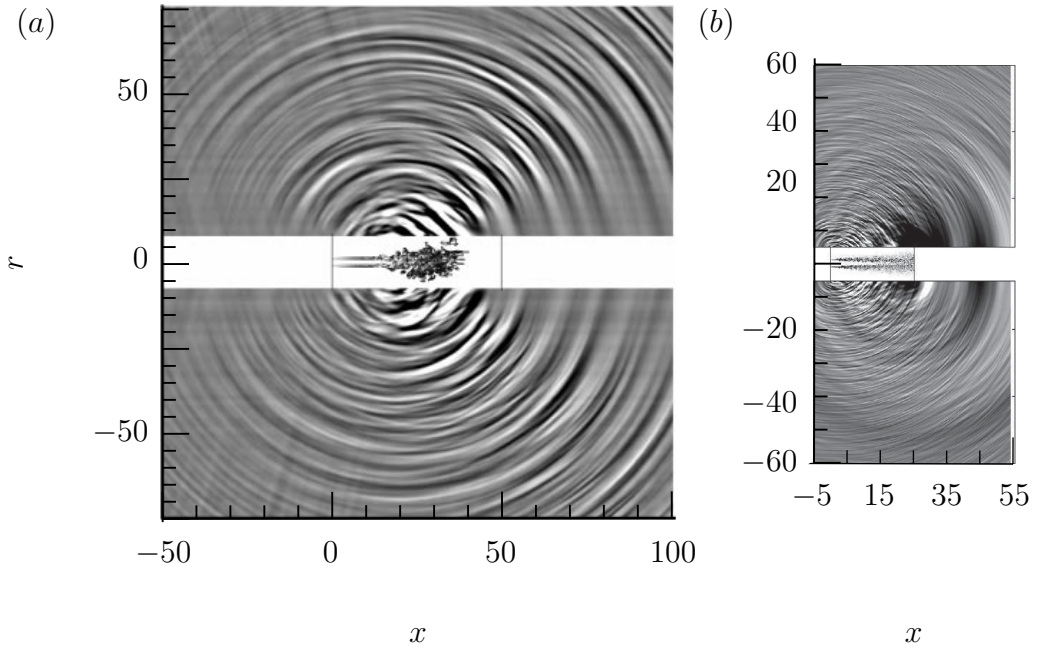

Figure 1.6: Vortical structures and acoustic far-field for two simulations of $Ma = 0.9$ jets. (a): DNS result from Freund (2001), $Re = 1800$ and $\theta \approx R/60$. (b): LES result from Bogey and Bailly (2010), $Re = 5 \cdot 10^4$ and $\theta \approx R/173$.

well as a strong dependence on the angle of observation with respect to the jet axis, ϑ, as shown in figure 1.7(b) ($\vartheta = 0$ corresponds to the downstream direction). As reviewed by Karabasov (2010), these features are associated with the presence of two sound generation mechanisms. First, fine scale turbulent fluctuations in the near-field radiate a broad-band sound that dominates for large values of ϑ. Closer to the jet axis, acoustic waves mostly come from large scale structures and are characterized by a more peaky spectrum. A typical frequency spectrum of the sound pressure level is displayed in figure 1.7(a): it exhibits a maximum at a Strouhal number $St_D \approx 0.2$, thereby confirming the relevance of the jet-column oscillations in sound generation processes.

1.3 *Local* and *global* stability

Flow stability has traditionally been studied within the assumption that the wavelength of the instability mechanism is short compared to the typical scale of the streamwise flow development. This allows the stability problem

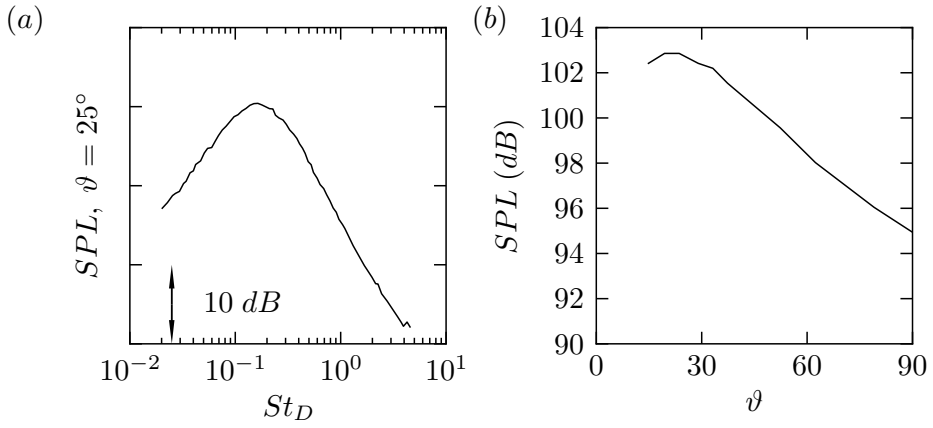

Figure 1.7: Experimentally measured sound pressure levels for an isothermal jet at $Ma = 0.75$ and $Re = 6.6 \cdot 10^5$. (a): frequency spectrum at an angle $\vartheta = 20°$ from the jet axis. (b): SPL as a function of the observation angle ϑ. Data taken from Bogey et al. (2007).

to be Fourier-decomposed in the streamwise and azimuthal (or spanwise) directions, so that only the cross-stream direction remains to be discretized. This assumption results in numerical calculations small enough that they have been performed since the 60's. Several types of problems may be treated within this framework, and they are referred to in this thesis as *local* stability analyses:

- in temporal stability problems the long time behavior of perturbations with a prescribed real streamwise wavenumber is considered (Michalke 1964).
- the signaling problem, i.e. the response of the flow to a time-harmonic localized perturbation, is described in terms of spatial eigenmodes at a given real frequency (Michalke 1965).
- the analysis of the dispersion relation between complex frequencies and wavenumbers also allows to study the response of the flow to a spatially and temporally localized impulse, and to distinguish between convective and absolute instabilities (Huerre and Monkewitz 1985).
- the short-term temporal amplification of spatially distributed perturbations is described within the optimal perturbation formalism (Reddy and Henningson 1993)

- the receptivity to external forcing is analyzed in terms of the resolvent of the flow equations for a given real frequency and real wavenumber (Trefethen et al. 1993).

Non-parallel effects in the signaling problem may be approximately accounted for while still considering the discretization of one-dimensional problems. In the WKB approximation (Crighton and Gaster 1976), the cross-stream distribution of the perturbation is assumed to be that of the k^+ spatial instability branch (in the sense of e.g. Huerre and Monkewitz (1990)), and its downstream evolution is solved forward in x. The Parabolized Stability Equations (Herbert 1997) also involve the solution of a series of one-dimensional problems by neglecting upstream traveling information, but they consider a general distribution of perturbations in the cross-stream direction.

It is now possible to treat linear stability problems in a framework where no assumption is made regarding the order of magnitude of the perturbation wavelength by discretizing all the non-homogeneous directions. Such approaches are referred to as *global*, in contrast with the *local* analyses described above. This distinction does not correspond to a difference in the methodology or mathematical concepts involved, but to the investigation of different situations. Using a two- or three-dimensional discretization, the temporal eigenmodes, optimal perturbations and optimal forcing (receptivity) can be analyzed by using exactly the same formalism as in the local approach. The modal analysis of the linearized flow equations gives access to the growth or decay rate, to the frequency and to the spatial structures of the eigenmodes. As finite domains are considered in the streamwise direction, the presence of unstable modes characterizes situations where perturbations grow exponentially in time at each location, in the same way as the absolute instability introduced in a local framework. On the contrary, in a local approach, temporally unstable modes may reflect either convectively or absolutely unstable behavior. Temporal eigenmodes in a global framework allow the characterization of flow bifurcations (Barkley et al. 2002) and, when the adjoint equations are also considered, of their variation with respect to the base flow (Marquet et al. 2008). The computation of eigenmodes for 2D problems may also be used to study the coupling between instability mechanisms in different flow regions (Mack et al. 2008). The meaning of optimal perturbation and optimal forcing results obtained in a global framework (Monokrousos et al. 2010) also differs from their counterparts in a local approach. In a global framework, the optimal initial condition is streamwise localized, in contrast to the local approach where it is extended in the streamwise direction. In a sense, the global optimal perturbation analysis contains the impulse response problem. The same holds for the global optimal analysis: it contains the signaling

problem. The local and global approaches are therefore complementary to describe and understand the dynamics of perturbations in non-parallel flows.

1.4 Objectives

The main objective of this thesis is to provide a description of the instability mechanisms that lead to the development of the preferred mode of a jet while still in a linear regime, as experimentally observed by Moore (1977). The local spatial problem, solved by Michalke (1971), exhibits at most one unstable mode associated with the shear layer instability. In order to provide an understanding of the large-scale instability structures, Crighton and Gaster (1976) and Strange and Crighton (1983) treated the signaling problem using a WKB approximation, which amounts to considering that the perturbation continually evolves in the streamwise direction in the form of a local shear layer mode. Such an analysis gives results that are in reasonable agreement with measurements by Crow and Champagne (1971). Piot et al. (2006) and Gudmundsson and Colonius (2009) treated this problem for compressible jets using PSE, and found good agreement with experimental data obtained in natural jets. Global approaches have been used in the context of laminar supersonic isothermal jet flows by Nichols and Lele (2011b). Two families of stable modes were identified: downstream traveling Kelvin-Helmholtz waves and upstream traveling disturbances linked to acoustic waves in the outer flow. The optimal perturbations of the jet were also computed, and very high amplification levels were reached. In another study (Nichols and Lele 2011a) the authors report the presence of unstable Kelvin-Helmholtz modes at low frequencies in a heated jet configuration.

By analogy with the Ginzburg–Landau model, Monkewitz (1989) and Huerre and Monkewitz (1990) described the preferred mode as a "slightly damped global mode" maintained by a low-level of forcing. This hypothesis is investigated in this thesis in terms of the linearized Navier–Stokes equations. Following the recent stability analyses in a global framework by for example Mack et al. (2008), Nichols and Lele (2011b) and Monokrousos et al. (2010), modal and non-modal linear stability concepts are applied to jet flows. In order to consider both near field fluctuations and acoustic radiation, these studies are carried out in both compressible and incompressible settings.

1.5 Outline

The linear stability computations in this study require a discretization of the linearized Navier–Stokes equations and a way to perform adjoint-based optimization. Chapter 2 describes the tools used throughout this thesis for the modeling of compressible and incompressible flows.

Krylov subspace methods allow the computation of selected eigenmodes of linear operators. Standard algorithms that target inner modes require either large memory resources when they are used with direct linear solvers, or a suitable preconditioning when an iterative solver is chosen. These approaches did not allow the satisfactory solution of the compressible eigenvalue problems encountered in the present study. Instead, the *shift-relax* method described in chapter 3 was developed for precisely this purpose.

As no experimentally or numerically obtained turbulent mean flow was available to perform the stability analysis, a model developed by Sohn (1986) was adapted to fit the configuration displayed in figure 1.2, as described in chapter 4.

Chapter 5 considers the global modal analysis necessary to identify the least stable of the jet eigenmodes. This study leads to a more general discussion about the modal representation of convection-dominated stable dynamics. It is demonstrated that in a globally stable situation the computation of optimal perturbations, which bypasses the global mode problem, provides a robust description of the flow dynamics.

The receptivity of incompressible jet flows to external forcing is treated in chapter 6. The analyses of Crighton and Gaster (1976) and Strange and Crighton (1983), that respectively treated the signaling problems for axisymmetric and helical perturbations, are considered from the point of view of optimal forcing. The response to boundary and body forcing is considered.

Compressibility effects on the receptivity analysis are investigated in chapter 7, in particular acoustic radiation by wave-packets and the excitation of vortical structures by acoustic waves. The spatial distribution of the forcing terms is not only optimized with respect to the energy of the flow response but also with respect to its acoustic power.

Concluding remarks are given in chapter 8.

Chapter 2

Numerical methods

The flow configuration used for the present study is that of a cylindrical jet exiting a circular pipe. Due to the axisymmetric geometry, the flow is conveniently described in terms of cylindrical coordinates (x, r, θ) (respectively, the axial, radial and azimuthal directions), and all variables can be Fourier decomposed in the azimuthal direction θ:

$$f(x, r, \theta; t) = \sum_m f_m(x, r; t) \exp(\mathrm{i}m\theta).$$

Base flows are assumed to be axisymmetric, so only the $m = 0$ component needs to be considered, and a two-dimensional discretization is therefore sufficient. Perturbations however can be helical, and different values of m should be considered. In a linear framework all the Fourier modes are independent and can be treated separately using 2D simulations.

The present chapter describes how these 2D computations are carried out in the case of compressible and incompressible flows.

2.1 Compressible flow

One of the reasons why compressible flows are considered here is to study the acoustic radiation associated with the instability structures in the near field of the jet. The first stage in Computational Aero-Acoustics (CAA) studies is the resolution of the near field flow structures. This can be done through Direct Numerical Simulation (see e.g. Freund (2001), Sandberg et al. (2012)) or Large Eddy Simulation (see e.g. Bogey et al. (2011), Bogey and Bailly (2006)). RANS or u-RANS methods are less suited for jet flows (see Georgiadis and DeBonis (2006)). Different numerical methods can be used for the simulation of compressible flows. A first approach, derived initially

for hyperbolic systems, consists of splitting the flow variables at each location into characteristics, which are then treated differently depending on the propagation direction. These methods, implemented in a Finite Volumes (e.g. in Johnsen and Colonius (2006)) or Finite Differences (FD) framework (e.g. in Sesterhenn (2000), Yee et al. (1999)), can be coupled with explicit time marching algorithms (e.g. Runge-Kutta schemes) to produce stable discretizations for subsonic and/or supersonic flows. In such computations, stability is achieved by introducing numerical dissipation through the use of decentered schemes. Other methods, such as Entropy Viscosity (Guermond et al. 2011), explicitly add viscosity at locations where entropy is created in order to stabilize the simulation. These methods are well suited for the computation of complex flows, but may be very costly for the direct computation of acoustic propagation in the far field. Indeed, their numerical dissipation requires a fine mesh in order to treat the propagation of acoustic waves. To avoid excessive numerical costs, near-field solvers can be coupled with an acoustic solvers in either the time or frequency domain through an acoustic analogy or an integral method: this is the type of approach used in industrial applications.

On the other hand acoustic propagation in the far field can be directly computed together with the near field (Bailly et al. 2010). This approach, referred to as Direct Noise Computation, is taken here. For this purpose, the numerical scheme is designed for the accurate treatment of sound radiation. The numerical code derives from an ONERA code (AJAX), which in particular has been used in Lesshafft et al. (2006), Lesshafft (2007).

2.1.1 Non-dimensional equations

We consider a jet issuing from of a semi-infinite cylindrical duct of radius R^*, with a velocity U_0^* on the jet axis. The jet exits into fluid at rest, characterized by its density ρ_∞^* and its temperature T_∞^*. The fluid is assumed to be a perfect Newtonian gas; furthermore, its adiabatic index $\gamma = 1.4$, thermal conductivity κ^*, specific heat at constant pressure C_p^* and viscosity μ^* are assumed to be constant.

Non-dimensional variables, denoted without asterisks, are defined with respect to R^*, U_0^*, ρ_∞^* and T_∞^* as reference length, velocity, density and temperature scales. With this normalization, natural choices for the Reynolds, Mach and Prandtl numbers are

$$Re = \frac{U_0^* R^* \rho_\infty^*}{\mu^*}, \qquad Ma = \frac{U_0^*}{c_\infty^*}, \qquad Pr = \frac{\mu^* C_P^*}{\kappa^*},$$

where $c_\infty^* = \sqrt{\gamma r^* T_\infty^*}$ denotes the ambient speed of sound. In terms of

dimensionless variables, the equation of state becomes

$$p = \frac{\rho T}{\gamma Ma^2}$$

and the internal energy e is given by

$$e = \frac{T}{\gamma(\gamma-1)Ma^2}.$$

Entropy may be defined as

$$s = \frac{1}{\gamma(\gamma-1)Ma^2}\left[\log(p) - \gamma\log(\rho)\right].$$

Frequencies f^* can be non-dimensionalized either in form of a Strouhal number (based on the jet diameter) or a dimensionless circular frequency ω, according to

$$St = \frac{2f^*R^*}{U_0^*} = \frac{\omega}{\pi}.$$

The flow is described in cylindrical coordinates r, x, θ, with $x = 0$ corresponding to the nozzle exit. Using the above non-dimensionalization, the compressible Navier–Stokes equations are given by Sandberg (2007). The characteristic formulation is used: the evolution of the flow field $\boldsymbol{q} = (\rho, \rho u_x, \rho u_r, \rho u_\theta, \rho E)^1$ is given by

$$\frac{\partial \boldsymbol{q}}{\partial t} + \frac{\partial F_e^x - F_v^x}{\partial x} + \frac{\partial F_e^r - F_v^r}{\partial r} + \frac{1}{r}\frac{\partial F_e^\theta - F_v^\theta}{\partial \theta} + \frac{F_e - F_v}{r} = 0. \tag{2.1}$$

The inviscid fluxes, denoted by the subscript $_e$, are given by

$$\begin{aligned}
F_e^x(\boldsymbol{q}) &= (\rho u_x \;, \rho u_x u_x + p \;, \rho u_x u_r \;, \rho u_x u_\theta \;, (\rho E + p)u_x),\\
F_e^r(\boldsymbol{q}) &= (\rho u_r \;, \rho u_r u_x \;, \rho u_r u_r + p \;, \rho u_r u_\theta \;, (\rho E + p)u_r),\\
F_e^\theta(\boldsymbol{q}) &= (\rho u_\theta \;, \rho u_\theta u_x \;, \rho u_\theta u_r \;, \rho u_\theta u_\theta + p \;, (\rho E + p)u_\theta),\\
F_e(\boldsymbol{q}) &= (\rho u_r \;, \rho u_r u_x \;, \rho u_r u_r - \rho u_\theta u_\theta \;, 2\rho u_r u_\theta \;, (\rho E + p)u_r).
\end{aligned}$$

The viscous terms depend on the both the state variables and viscous stresses $\boldsymbol{s} = (\tau, \boldsymbol{q}_h)$:

$$\begin{aligned}
F_v^x(\boldsymbol{q}, \boldsymbol{s}) &= (0 \;, \tau_{xx} \;, \tau_{rx} \;, \tau_{\theta x} \;, \tau_{xx}u_x + \tau_{rx}u_r + \tau_{\theta x}u_\theta - q_x),\\
F_v^r(\boldsymbol{q}, \boldsymbol{s}) &= (0 \;, \tau_{rx} \;, \tau_{rr} \;, \tau_{\theta r} \;, \tau_{rx}u_x + \tau_{rr}u_r + \tau_{\theta r}u_\theta - q_r),\\
F_v^\theta(\boldsymbol{q}, \boldsymbol{s}) &= (0 \;, \tau_{\theta x} \;, \tau_{r\theta} \;, \tau_{\theta\theta} \;, \tau_{\theta x}u_x + \tau_{r\theta}u_r + \tau_{\theta\theta}u_\theta - q_\theta),\\
F_v(\boldsymbol{q}, \boldsymbol{s}) &= (0 \;, \tau_{rx} \;, \tau_{rr} - \tau_{\theta\theta} \;, 2\tau_{\theta r} \;, \tau_{rx}u_x + \tau_{rr}u_r + \tau_{\theta r}u_\theta - q_r).
\end{aligned}$$

[1] $E = e + \frac{1}{2}\boldsymbol{u}^2$ is the total energy.

The components of the stress tensor τ are given by

$$\begin{aligned}
\tau_{xx} &= \frac{2}{3Re}\left[2\frac{\partial u_x}{\partial x} - \frac{\partial u_r}{\partial r} - \frac{1}{r}\left(\frac{\partial u_\theta}{\partial \theta} + u_r\right)\right], \\
\tau_{rr} &= \frac{2}{3Re}\left[-\frac{\partial u_x}{\partial x} + 2\frac{\partial u_r}{\partial r} - \frac{1}{r}\left(\frac{\partial u_\theta}{\partial \theta} + u_r\right)\right], \\
\tau_{\theta\theta} &= \frac{2}{3Re}\left[-\frac{\partial u_x}{\partial x} - \frac{\partial u_r}{\partial r} - \frac{2}{r}\left(\frac{\partial u_\theta}{\partial \theta} + u_r\right)\right], \\
\tau_{rx} &= \frac{1}{Re}\left[\frac{\partial u_x}{\partial r} + \frac{\partial u_r}{\partial x}\right], \\
\tau_{\theta x} &= \frac{1}{Re}\left[\frac{\partial u_\theta}{\partial x} + \frac{1}{r}\frac{\partial u_x}{\partial \theta}\right], \\
\tau_{\theta r} &= \frac{1}{Re}\left[\frac{\partial u_\theta}{\partial r} + \frac{1}{r}\left(\frac{\partial u_r}{\partial \theta} - u_\theta\right)\right]
\end{aligned}$$

and the heat flux $\boldsymbol{q}_h$ by

$$\begin{aligned}
\boldsymbol{q}_{h,x} &= -\frac{1}{(\gamma-1)PrReMa^2}\frac{\partial T}{\partial x}, \\
\boldsymbol{q}_{h,r} &= -\frac{1}{(\gamma-1)PrReMa^2}\frac{\partial T}{\partial r}, \\
\boldsymbol{q}_{h,\theta} &= -\frac{1}{(\gamma-1)PrReMa^2}\frac{1}{r}\frac{\partial T}{\partial \theta}.
\end{aligned}$$

2.1.2 Spatio-temporal discretization

Mesh

The compressible Navier–Stokes equations are discretized using finite differences (FD) on a rectilinear grid. The mesh is designed as follows: let the discretization points be denoted (x_i), (r_j). With $\delta x_i = x_i - x_{i-1}$, the stretching is given by

$$S_i = 2\frac{\delta x_{i+1} - \delta x_i}{\delta x_{i+1} + \delta x_i} = 2\frac{x_{i+1} - 2x_i + x_{i-1}}{x_{i+1} - x_{i-1}}.$$

If the grid stretching is prescribed as a function of the position and the mesh size, then the discretization points satisfy

$$\frac{x_{i+1} - x_{i-1}}{2} S(x_i, x_{i+1} - x_{i-1}) - (x_{i+1} - 2x_i + x_{i-1}) = 0$$

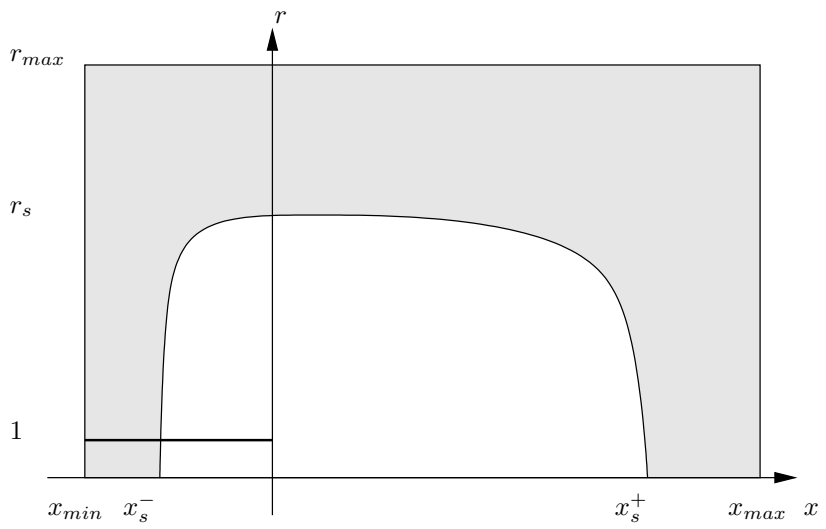

Figure 2.1: Numerical domain used for compressible computations. Sponge layers are displayed as shaded regions.

which corresponds to the FD discretization of

$$S(x(\eta), Nx'(\eta))x'(\eta) + Nx''(\eta) = 0$$

with $0 \leq \eta \leq 1$ and $N+1$ discretization points. This non-linear differential equation together with the boundary conditions $x_0 = X_0$ and $x_N = X_1$ is solved iteratively on successively finer grids as a steady solution of

$$\dot{x} = S(x, Nx')x' + Nx''.$$

The stretching function S is prescribed in order to match the geometry of the problem while keeping both the mesh size and the stretching within controlled bounds. For example in the radial direction the following stretching is imposed:

$$S(r, Nr') = \begin{cases} S_{max} f_1(r) f_2(Nr') & r \leq R_s \text{ and } Nr' \leq \delta_{max} \\ 0 & r \leq R_s \text{ and } Nr' \geq \delta_{max} \\ S_{max} f_3(r) & r \geq R_s \end{cases} \tag{2.2}$$

with

$$f_1(r) = \frac{r}{r+1} \tanh\left(r - \frac{1}{r}\right),$$
$$f_2(z) = 1 + \tanh\left(0.05 \frac{\delta_{max}}{z - \delta_{max}}\right),$$
$$f_3(r) = 1 - \tanh\left(\frac{10}{R_s - r}\right).$$

Function f_1 ensures that the mesh is refined around $r = 1$ and that it is smooth on the axis. The maximum mesh size inside the physical domain ($r \leq R_s$) is set to δ_{max} using function f_2, and f_3 allows a smooth stretching throughout the sponge layers. A similar approach is used for the axial mesh, resulting in the typical meshes displayed in figure 2.2.

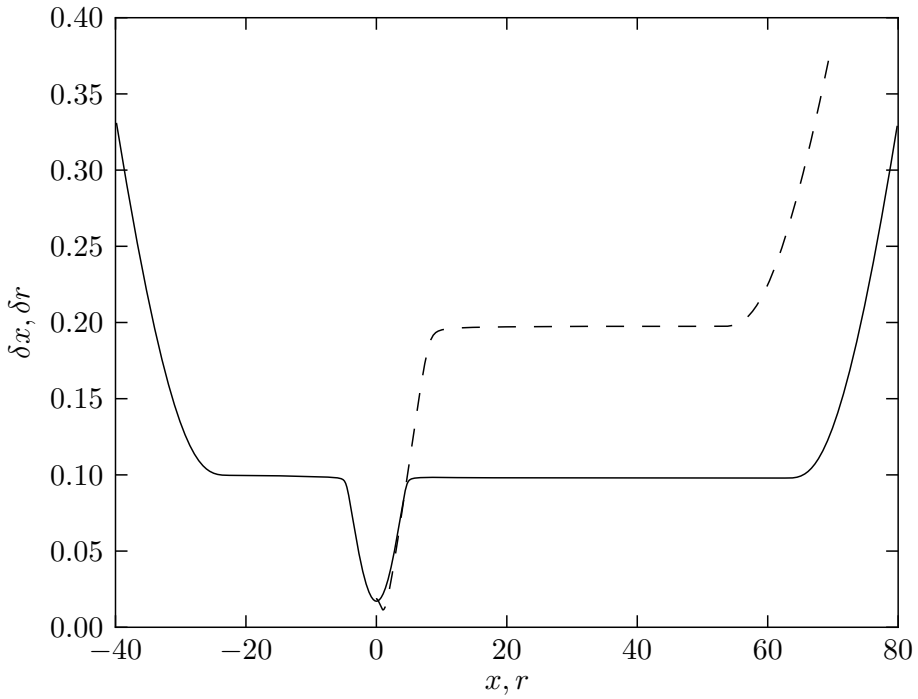

Figure 2.2: Typical grid size found as a function of the position for the axial (solid line) and radial (dashed line) directions. The maximum stretching allowed is 4% for the axial mesh and 5% for the radial mesh.

Spatial schemes

For a given stencil width, different approaches can be used for the design of accurate FD schemes. In standard schemes the FD coefficients are chosen such that the scheme is of maximum order, i.e. the scheme that will better approximate the derivatives in the limit of arbitrarily small mesh size. One can also derive numerical schemes that optimally approximate the dispersion relation of the physical problem: these schemes are called Dispersion Relation Preserving (Tam and Webb 1993). The FD schemes used here, derived

by Berland et al. (2007) are optimized in order to maximize, for a given order, the resolution of the scheme: in this approach, originally described by Lele (1992), the focus is not only on well-resolved structures. For this, the derivatives of functions of the type $f(x) = \exp(\mathrm{i}kx)$ are considered. In discrete form, one has $f_j = \exp(\mathrm{i}kj\delta x)$ and, as the discretization scheme is linear, the FD approximation of $f'(x)$ is of the form $f'_j = \mathrm{i}k'\delta x \exp(\mathrm{i}kj\delta x)$: the discretization error is therefore measured in terms of the difference $k\delta x - k'\delta x$ as a function of $k\delta x$ (see figure 2.3 for the dispersion error of different schemes). The idea is to best approximate the derivative of functions with typical wavelengths that are of the order of the size of the discretization, i.e. $k\delta x \sim 1$, rather than focusing only on $k\delta x \ll 1$. The schemes of Berland et al. (2007) are designed such that the error in approximating the derivative is less than 10^{-5} with as low as four points per wavelength.

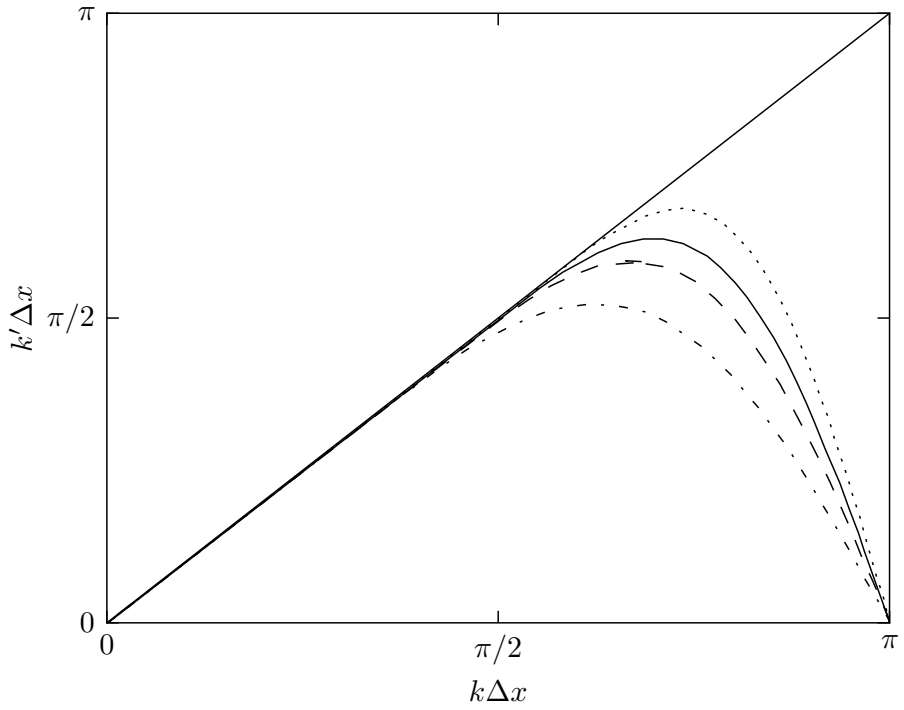

Figure 2.3: Effective wavenumber k' versus wavenumber k for different FD schemes used in aero-acoustics: DPR scheme of Tam and Webb (1993) for a 7-point stencil (dash-dot line), and of the optimized schemes of Bogey and Bailly (2004) with 9-, 11- and 13-point stencils (resp. dashed, solid and dotted lines). Data taken from Bogey and Bailly (2004).

Central schemes are used (except on boundary points) for the approximation of the derivatives for both convective and diffusive terms in the Navier–Stokes equations. Such a discretization is unstable, as small wavelengths are amplified. In order to maintain the stability for temporal simulations a selective low-pass filter (also given in Berland et al. (2007)) is used which adds additional damping at very small scales to counteract the "under-dissipation" of centered schemes for advection problems.

Boundary conditions

Jet pipe The jet pipe is modeled as an infinitely thin adiabatic surface. Although this approximation introduces a singularity, it allows us to eliminate the pipe thickness as an additional length scale of the problem. The pipe wall is placed between two discretization points (the mesh designed as described above is slightly modified such that $r = 1$ is exactly between two discretization points) so that different values for the pressure and density fields do not have to be considered on the inner and outer side of the jet pipe. No-slip and no-heat-flux boundary conditions are imposed on the pipe wall ($x \leq 0$ and $r = 1$) directly through FD schemes that take into account homogeneous Dirichlet or Neumann boundary conditions exactly at the pipe wall location (i.e. between two discretization points).

Axis Ghost points are used for the treatment of the axis. As explained in Tuckerman (2012), smooth scalar functions described in polar coordinates should be such that

$$f(r,\theta) = \sum_{m\in\mathbb{Z}} \sum_{j\geq m,\ j+m \text{ even}} \alpha_{j,m} r^j \exp(\mathrm{i}m\theta).$$

Consequently, one can impose that, depending on the parity of the azimuthal wave number m, flow fields are either even or odd with respect to the axis.

m	odd	even
ρ, ρE, u_x	odd	even
u_r, u_θ	even	odd

For this purpose, ghost points are used for $r < 0$. Note that in order to avoid problems arising from the $1/r$ terms in the cylindrical formulation of the differential operators, the radial location $r = 0$ is chosen to fall between two discretization points.

Outer boundaries Different types of boundary conditions are used for the treatment of far-field conditions ($x = x_{min}$, $x = x_{max}$ and $r = r_{max}$) for the different studies. For eigenmode computations outflow boundary condition play a crucial role, so the non-reflecting boundary treatment of Bogey and Bailly (2002) is used together with sponge layers. For other studies, perturbations are assumed to vanish at the outflow, and acoustic waves are damped as they travel through the sponge regions. A more recent version of the code now uses the Local One DImensional conditions of Poinsot and Lele (1992).

Parallelism

For parallel computations, a domain decomposition approach is used using MPI. In its most recent form, the code uses PETSc for this purpose.

2.1.3 Adjoint equations

Linear stability analyses often benefit from an implementation of the adjoint Navier–Stokes equations. Two approaches can be used, referred to as the continuous and discrete adjoint. The first method consists in first deriving the adjoint equations for the continuous problem (Linearized Navier–Stokes equations and boundary conditions) and for a given inner product, and then discretizing them. This is for example the approach used in Meliga et al. (2010): it has the advantage of giving results that are less sensitive to the numerical discretization. But deriving the adjoint equations can be a very tedious task, in particular for boundary conditions. In contrast, one can first discretize the LNS equations and then compute its adjoint via the Hermitian transpose (denoted by †) : if Q is the mass matrix, then

$$\langle \boldsymbol{q}|\boldsymbol{q}\rangle = \boldsymbol{q}^\dagger Q \boldsymbol{q}, \tag{2.3}$$

so the adjoint L^* of an operator L satisfies

$$\langle \boldsymbol{p}|L\boldsymbol{q}\rangle = \boldsymbol{p}^\dagger Q L \boldsymbol{q} = \overline{\boldsymbol{q}^\dagger L^\dagger Q \boldsymbol{p}} = \overline{\boldsymbol{q} Q Q^{-1} L^\dagger Q \boldsymbol{p}} = \overline{\langle \boldsymbol{q}|L^*\boldsymbol{p}\rangle} = \langle L^*\boldsymbol{p}|vq\rangle \tag{2.4}$$

where overbar $\bar{\cdot}$ denotes the complex conjugate, so $L^* = Q^{-1}L^\dagger Q$. If the matrices corresponding to the LNS equations are available, this method is straightforward to apply and has two advantages over the continuous adjoint approach. First, it results in operators that are truly Hermitian, for example in the context of optimal forcing or optimal perturbation studies. This ensures fast and robust convergence of iterative algorithms. Then, changing the inner product can be done very simply by modifying operators Q and

Q^{-1}, which is easily computed by hand when using FD discretizations. Since in this approach one performs optimization on the discrete system, numerical artifacts may be present in the results. This can be argued to be a drawback, but can also be seen as an advantage as it shows the possible limitations of the discretization. For a discussion on this subject, see Sirkes and Tziperman (1997).

Assembling and storing the discretization matrices in the present application would require significant storage (due to both the mesh size and the large stencil of the FD schemes, see chapter 3). Instead the matrix-free framework of de Pando et al. (2012) is used.

Let L be the linearized Navier–Stokes equations and $\boldsymbol{q}$ the discrete state vector, containing the values of ρ, ρu_u, ρu_x, ρu_θ and ρE at each discretization point. Using the formulation (2.1), the inviscid part of L can be written as :

$$M_e = A_e + D_x A_e^x + D_r A_e^x$$

where A^e, A_x^e and A_r^e are block diagonal matrices [2] given by

$$A_e^x = \boldsymbol{\nabla}_{\boldsymbol{q}} F_e^x(\boldsymbol{q}) \qquad A_e^r = \boldsymbol{\nabla}_{\boldsymbol{q}} F_e^r(\boldsymbol{q}) \qquad A_e = \frac{1}{r}\left(im\boldsymbol{\nabla}_{\boldsymbol{q}} F_e^\theta(\boldsymbol{q}) + \boldsymbol{\nabla}_{\boldsymbol{q}} F_e(\boldsymbol{q})\right)$$

and operators D_x and D_r correspond to the discrete derivatives in the axial and radial directions. Numerically, A^e, A_x^e and A_r^e are built (and stored in CSR format), but D_x and D_r are applied in a matrix free manner, resulting in low memory requirements. The main advantage of this decomposition lies in the ease of taking the transpose conjugate without assembling the full discretization matrices:

$$M_e{}^\dagger = A_e{}^\dagger + A_e^{x\dagger} D_x^\dagger + A_e^{r\dagger} D_r^\dagger.$$

Operators $A^{e\dagger}$ $A_x^{e\,\dagger}$ and $A_r^{e\dagger}$ are applied by taking the Hermitian transpose of the block diagonal matrices, while $D_x^\dagger$ and $D_r^\dagger$ are still applied in a matrix-free framework.

Viscous terms are treated similarly: let us introduce a vector $\widetilde{\boldsymbol{q}}$ which contains, at each discretization point, the approximations the flow variables as well as the viscous stresses and heat fluxes. It can be written as

$$\widetilde{\boldsymbol{q}} = M_\tau \boldsymbol{q} = \left(A_\tau + D_x A_\tau^x + D_r A_\tau^r\right)\boldsymbol{q}.$$

Using this vector, the viscous part of the LNS operator can be expressed as

$$L_v \boldsymbol{q} = A_v + D_x A_v^x + D_r A_v^x = M_v M_\tau \boldsymbol{q}.$$

The adjoint of L is therefore computed as

$$L^\dagger = M_e{}^\dagger + M_\tau{}^\dagger M_v{}^\dagger.$$

[2] Their 5×5 blocks correspond to linear combinations of the flow variable at the same discretization point.

Boundary conditions Vector $\boldsymbol{q}$ contains ghost points used to impose symmetry boundary conditions on the axis. Consequently, not all components of $\boldsymbol{q}$ are degrees of freedom. Let $\boldsymbol{q}'$ correspond to the components of $\boldsymbol{q}$ that are actual degrees of freedom. It is related to $\boldsymbol{q}$ by

$$\boldsymbol{q} = P\boldsymbol{q}'.$$

In practice, the action of P is applied matrix-free. One should however notice that $P^\dagger \neq P$. The operator $P^\dagger$ has no obvious continuous interpretation. For example in 1D, one may impose that the function is odd using

$$P = \begin{pmatrix} -1 & 0 & \cdots & 0 \\ 1 & 0 & \cdots & 0 \\ 0 & \ddots & & \vdots \\ \vdots & & \ddots & 0 \\ 0 & \cdots & 0 & 1 \end{pmatrix},$$

in which case one would have

$$P^\dagger = \begin{pmatrix} -1 & 1 & 0 & \cdots & 0 \\ 0 & 0 & \ddots & & \vdots \\ \vdots & \vdots & & \ddots & 0 \\ 0 & 0 & \cdots & 0 & 1 \end{pmatrix}.$$

The same applies to ghost points used to communicate values between processes.

Summary In order to apply the LNS operator, the code successively

- applies boundary conditions (P),
- communicate ghost points around each subdomain (MPI parallelism) and updates ghost points (BCs on the axis) (C),
- computes inviscid fluxes (M_e) and viscous stresses (M_τ),
- communicates viscous stresses and updates ghost points ($\widetilde{C}$),
- computes viscous fluxes (M_v),

so the operator can formally be decomposed as

$$L = (M_e + M_v\widetilde{C}M_\tau)CP$$

and

$$L^\dagger = P^\dagger C^\dagger (M_e^\dagger + M_\tau^\dagger \widetilde{C}^\dagger M_v^\dagger).$$

The above expression shows that when applying the adjoint operator, applying BCs and communicating ghost points occur *in a modified manner* ($P^\dagger \neq P$ *and* $C^\dagger \neq C$) and *after* computing the derivatives.

Free propagator Let us focus on the propagation in time of unforced linear dynamical system of the form $\dot{\boldsymbol{q}} = A\boldsymbol{q}$ using a Euler or Runge-Kutta scheme. At each time step, the state is updated using[3]

$$\boldsymbol{q}_{i+1} = \underbrace{\sum_{j=0}^{k} \frac{(\delta t L)^j}{j!}}_{A_q} \boldsymbol{q}_i \tag{2.5}$$

such that the state after N time steps is $\boldsymbol{q}_N = A_q^N \boldsymbol{q}_0$. We can then formally write the direct propagator as

$$\mathcal{P} = A_q^N.$$

Its adjoint is then

$$\mathcal{P}^\dagger = A_q^{\dagger N}.$$

The adjoint of the propagator is therefore applied by substituting L for $L^\dagger$ in the time stepping algorithm. If a filter is applied to the state after each time step, however, slight changes have to be made. Let F denote the filter. (2.5) becomes

$$\boldsymbol{q}_{i+1} = F A_q \boldsymbol{q}_i$$

such that the propagator is $\mathcal{P}' = (F A_q)^N$ and $\mathcal{P}'^\dagger = (A_q^\dagger F^\dagger)^N$. This shows that in the adjoint algorithm, the adjoint of the filtering routine should be applied *before* each time step.

Forced propagator In order to integrate $\dot{\boldsymbol{q}} = A\boldsymbol{q} + \boldsymbol{f}$, the operation at each time step is

$$\boldsymbol{q}_{i+1} = \underbrace{\sum_{j=0}^{k} \frac{(\delta t L)^j}{j!}}_{A_q} \boldsymbol{q}_i + \underbrace{\sum_{j=1}^{k} \delta t \frac{(L\delta t)^{j-1}}{j!}}_{A_f} \boldsymbol{f}. \tag{2.6}$$

[3]This is the case of standard schemes of order k.

If $\boldsymbol{q}_0 = 0$, this yields

$$\boldsymbol{q}_i = \sum_{j=0}^{i-1} A_q^j A_f \boldsymbol{f}.$$

The adjoint of the discrete propagator

$$\mathcal{P}_f = \left[\sum_{j=0}^{N-1} A_q^j\right] A_f$$

which takes $\boldsymbol{f}$ as an input and returns $\boldsymbol{q}_N$ after N time steps, is formally

$$\mathcal{P}_f^\dagger = A_f^\dagger \left[\sum_{j=0}^{i-1} A_q^{\dagger j}\right].$$

The above expresses how the adjoint of the forced propagator is taken: if $\boldsymbol{f}$ is the input, it should return $\boldsymbol{q}^*$ such that

$$\begin{aligned} \boldsymbol{q}_0^* &= 0, \\ \boldsymbol{q}_{i+1}^* &= A_q^\dagger \boldsymbol{q}_i^* + \boldsymbol{f} \quad \text{for } i = 1 \dots N-1, \\ \boldsymbol{q}^* &= A_f^\dagger \boldsymbol{q}_N^*. \end{aligned}$$

The same remark as in the previous paragraph about the effect of the filter also applies here.

Local time step If δt is a scalar, applying $A_q^\dagger$ simply amounts to propagating operator $L^\dagger$ forward in time with the same algorithm as in the direct case. If a local time step is applied, however, care should be taken as δt is an operator that does not commute with L. If (2.6) still applies for the direct time stepper[4], we formally have

$$A_q^\dagger = \sum_{j=0}^{k} \frac{\left(L^\dagger \delta t\right)^j}{j!}$$

which means that the state should be multiplied by the local time step before the increment is computed.

[4]This depends on the actual implementation, and corresponds to the fact that the increment is computed and then multiplied by the local time step

2.2 Incompressible flow

2.2.1 Equations

Using the same convention as for the compressible case, and replacing the pressure p by p/ρ, the incompressible Navier–Stokes equations in cylindrical coordinates are given by

$$\frac{1}{r}\frac{\partial(ru_r)}{\partial r} + \frac{1}{r}\frac{\partial u_\theta}{\partial \theta} + \frac{\partial u_x}{\partial x} = 0,$$

$$\frac{\partial u_x}{\partial t} + u_r\frac{\partial u_x}{\partial r} + \frac{u_\theta}{r}\frac{\partial u_x}{\partial \theta} + u_x\frac{\partial u_x}{\partial x} = - \frac{\partial p}{\partial x} + \frac{1}{Re}\left[\frac{1}{r}\frac{\partial}{\partial r}\left(r\frac{\partial u_x}{\partial r}\right) + \frac{1}{r^2}\frac{\partial^2 u_x}{\partial \theta^2} + \frac{\partial^2 u_x}{\partial x^2}\right],$$

$$\frac{\partial u_r}{\partial t} + u_r\frac{\partial u_r}{\partial r} + \frac{u_\theta}{r}\frac{\partial u_r}{\partial \theta} + u_x\frac{\partial u_r}{\partial x} - \frac{u_\theta^2}{r} = - \frac{\partial p}{\partial r} + \frac{1}{Re}\left[\frac{1}{r}\frac{\partial}{\partial r}\left(r\frac{\partial u_r}{\partial r}\right) + \frac{1}{r^2}\frac{\partial^2 u_r}{\partial \theta^2} + \frac{\partial^2 u_r}{\partial x^2} - \frac{u_r}{r^2} - \frac{2}{r^2}\frac{\partial u_\theta}{\partial \theta}\right],$$

$$\frac{\partial u_\theta}{\partial t} + u_r\frac{\partial u_\theta}{\partial r} + \frac{u_\theta}{r}\frac{\partial u_\theta}{\partial \theta} + u_x\frac{\partial u_\theta}{\partial x} + \frac{u_r u_\theta}{r} = - \frac{1}{r}\frac{\partial p}{\partial \theta} + \frac{1}{Re}\left[\frac{1}{r}\frac{\partial}{\partial r}\left(r\frac{\partial u_\theta}{\partial r}\right) + \frac{1}{r^2}\frac{\partial^2 u_\theta}{\partial \theta^2} + \frac{\partial^2 u_\theta}{\partial x^2} + \frac{2}{r^2}\frac{\partial u_r}{\partial \theta} - \frac{u_\theta}{r^2}\right].$$

2.2.2 Spatio-temporal discretization

Incompressible computations were also performed. In this case, the far field does not need to be resolved and acoustic propagation is not an issue. The Finite Element Method is used for the discretization of the Navier–Stokes equations. Classical $P2 - P1$ elements are used (using FreeFEM++ Hecht (2011)) and no stabilization (e.g. SUPG) was required for the current computations. A penalty method is employed for the treatment of the continuity equation. The geometry used in this situation is slightly different from the compressible situation and is shown in figure 2.4: a solid wall Γ_w now extends for $(r = 1, x \leq 0)$ and $(x = 0, r \geq 1)$.

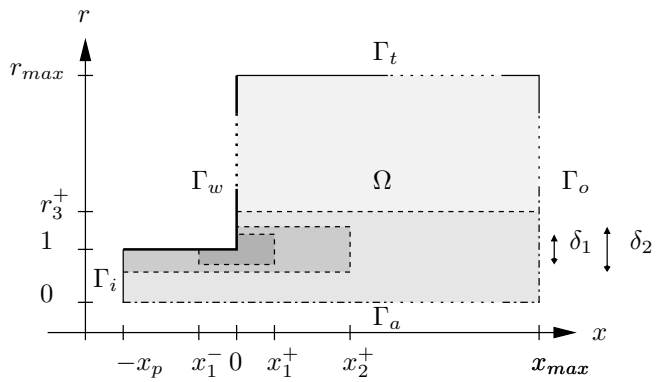

Figure 2.4: Numerical domain used for incompressible computations. Gray shades correspond to different mesh densities.

Treatment of the axis

Imposing symmetry conditions on the different flow variables (as was the case for the FD discretization of compressible flows) is not convenient with FreeFEM++. Instead on can impose the following homogeneous BCs:

	$m = 0$	$m = \pm 1$	$\lvert m\rvert \geq 2$
ρ, ρE, u_x	Neumann	Dirichlet	Dirichlet
u_r, u_θ	Dirichlet	Neumann	Dirichlet

Terms $1/r$ (resp. $1/r^2$) in the equations given above do not correspond to actual singularities, as the smoothness of the solution requires that the terms they are multiplying decay at least as fast as r (resp. r^2). However, in order to avoid numerical problems the equations are multiplied by r^2 before integrating by parts to obtain the variational formulation.

Adjoint equations

As for compressible flows, the discrete adjoint is used in incompressible computations. After the matrices corresponding to the FE discretization are assembled, taking the Hermitian transpose of matrices is straightforward.

Steady state solver

As discretization matrices are reasonably small, direct solvers are used. Therefore, steady states for the NS equations are computed within FreeFEM++ using Newton's method, and UMFPACK (Davis 2009) or MUMPS (Amestoy et al. 2000) are used for the solution of linear systems. This approach is computationally cheaper than advancing an initial guess forward in time until a

steady solution is reached. Starting from a parallel flow (given by the inflow condition) it takes ~ 15 Newton iterations to converge to a steady state with a precision of 10^{-10}.

Linear studies

As mentioned previously, discretization matrices are sufficiently small such that direct linear solvers can be used. These matrices are exported from FreeFEM++ and loaded into python to use solvers provided by PETSc (Balay et al. 2008) and SLEPc (Roman et al. 2010) through petsc4py and slepc4py (see § 2.3.1). This allows us to perform efficient parallel computations using MUMPS as a linear solver. Systems with up to one million DOFs can be handled on a regular desktop computer with $\sim$ 10GB of memory.

2.3 External packages

Computations performed for this study heavily rely on external libraries. In addition to FreeFEM++ mentioned above for incompressible analyses, the libraries PETSc and SLEPc are used. The input/output library HDF5 has also been used and allowed easy manipulation of data between the different computer architectures and between the different programs and programming languages.

2.3.1 PETSc (Portable, Extensible Toolkit for Scientific Computation)

Many PETSc features have been used. Recent versions of the compressible code use PETSc for managing the parallel computations through distributed arrays, for storing and using the block matrices resulting from the linearization and for time stepping. Incompressible computations rely on the implementation of parallel sparse matrices (CSR storage) and on the interfaces to linear solvers, both direct and iterative. Among the different direct solvers, MUMPS turned out to be more efficient than UMFPACK, SuperLU (sequential and distributed versions) and SPOOLES, both in terms of CPU time and memory usage.

2.3.2 SLEPc (Scalable Library for Eigenvalue Problem Computations)

SLEPc contains implementations of various iterative algorithms for eigenvalue computations. In particular, the Krylov-Schur solver appeared to be more robust than the Implicitly Restarted Arnoldi Method, implemented in ARPACK. The Lanczos algorithm was also used for Hermitian problems[5].

[5] using discrete adjoints given truly Hermitian discrete problems.

Chapter 3

Eigenvalue solver for compressible flows

3.1 Introduction

As described in § 2.1, using high-order schemes is necessary for the Direct Noise Computation. With such schemes on a $n_x \times n_r$ mesh, the discretization matrix for the inviscid terms would contain $\sim 5 \times 5 \times n_x \times n_r \times 2(2S+1)$ non-zero elements, where S is the half-width of the finite-difference stencil (see figure 3.1). The $2(2S+1)$ factor stems from the first-order derivatives in x and r, and the 5×5 from the dependence of each of the five flow variables $(\rho, \rho u_x, \rho u_r, \rho u_t, \rho E)$ on the other variables (this term is slightly over-estimated). With a typical mesh of $n_x = 1356$ and $n_r = 768$ grid points and the schemes of Berland et al. (2007), this would correspond to $\sim 5 \cdot 10^8$ non-zero elements. The discretization matrix for the viscous terms, on the other hand, would contain second-order cross derivatives, so the number of non-zero elements would be $\sim (3 \times 2 + 5) \times n_x \times n_r \times (4S + (2S+1)^2)$. Consequently, the total number of entries in the complete discretization matrix would be $\sim 1.6 \cdot 10^9$, and, in double precision complex arithmetic, storing the matrix would require ~ 25GB of memory, which is still affordable.

The costly part of standard linear algebra algorithms used in stability analyses, however, is not the assembly or the storage of the discretization matrix, but rather the computation of LU decompositions for the solution of the linear systems. The number of elements in a sparse LU factorization of a sparse matrix M is indeed not related to the number of elements in M. One of the few guarantees is that the bandwidth or the skyline structure of the L and U factors is not larger than that of M (Golub and Loan 1996). The structure of sparse matrices depends on the ordering of the degrees of

freedom and, consequently, so does the cost of the LU decomposition. In our applications with $n_x \geq n_r$, a natural ordering that reduces the bandwidth is to index of the flow variable $1 \leq i_q \leq n_q$ at position (i, j) in the grid as $i_q + n_q(j-1) + n_q n_r(i-1)$. Using such a numbering, the bandwidth of the matrix would be $2Sn_q n_r$[1], and therefore one could estimate that the L and U factors would contain $\sim n_x n_r n_q \times 2Sn_q n_r \sim 2 \cdot 10^{11}$ non-zero elements, which is untractable. The alternative proposed by Mack and Schmid (2010) is to use instead a preconditioned iterative solver. For the present problems, the robustness of this approach was poor, and a new solver had to be developed.

3.2 Paper: *A relaxation method for large eigenvalue problems, with an application to flow stability analysis*

[1] A factor of two could be gained by using specific schemes for second-order derivatives.

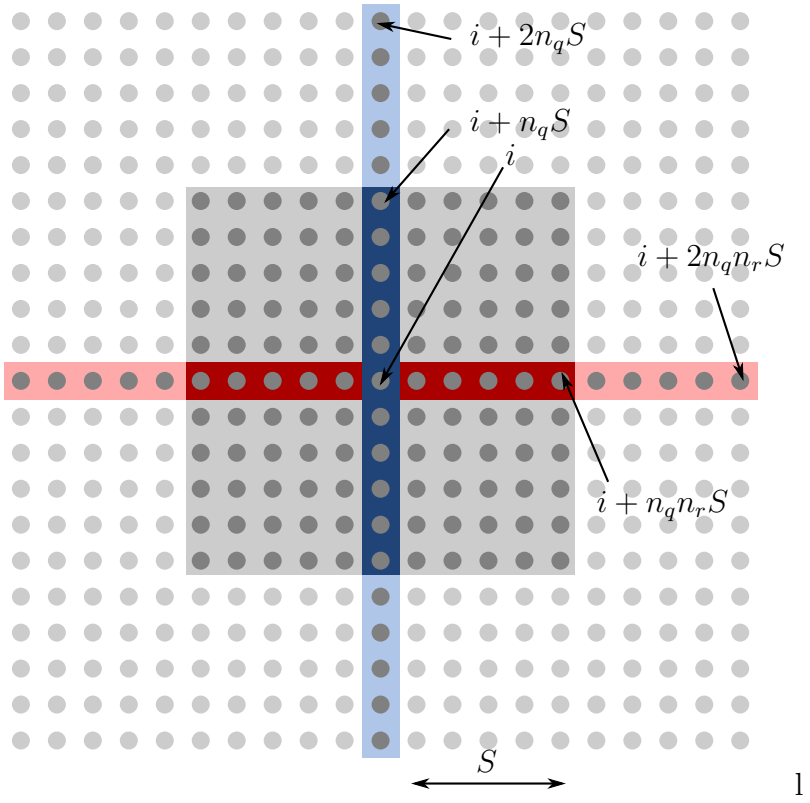

Figure 3.1: Schematic view of the stencil for finite-difference computations. Dark blue and red regions correspond to points used for the computations of first derivatives in the x and r directions. Lighter blue and red areas correspond to the stencil for second derivatives in x and r, and the gray area to the cross derivatives. The degrees of freedom (DOFs) are numbered such that the index of the flow variable $1 \leq i_q \leq n_q$ at position (i, j) in the grid is $i_q + n_q(j-1) + n_q n_r(i-1)$. In the present application $S = 5$ and $n_q = 5$.

A relaxation method for large eigenvalue problems, with an application to flow stability analysis

X. Garnaud, L. Lesshafft, P.J. Schmid, J.-M. Chomaz[a]

[a] *Laboratoire d'Hydrodynamique, Ecole Polytechnique – CNRS, Palaiseau, France*

Abstract

Linear stability analysis of fluid flows usually involves the numerical solution of large eigenvalue problems. We present a spectral transformation allowing the computation of the least stable eigenmodes in a prescribed frequency range, based on the filtering of the linearized equations of motion. This "shift-relax" method has the advantage of low memory requirements and is therefore suitable for large two- or three-dimensional problems. For demonstration purposes, this new method is applied to compute eigenmodes of a compressible jet.

Keywords: eigenvalue solver, spectral transformation, Krylov method, matrix-free, global modes

1. Introduction

The stability of fluid flow is a fundamental question in fluid dynamics, which has significant implications on the design, operation and control of flow devices. Consequently, hydrodynamic stability theory has taken a central role in fluid dynamics research, and remarkable progress has been made over the past decades. Early investigations of generic flow configurations, such as channel flows or boundary layers, have recently given way to more complex two- and three-dimensional geometries and more complex flow physics. The resulting eigenvalue problems from simple configurations were sufficiently small to allow their solution by direct techniques (such as the QR-algorithm). For more complex stability problems, however, direct techniques no longer provide a feasible solution; iterative eigenvalue algorithms have to be employed to compute a subset of the full spectrum that effectively describes the essential dynamics of small disturbances superposed on a steady base flow. Many of these algorithms for large-scale eigenvalue problems have been developed within the linear-algebra community and are readily available through several public domain libraries [12]. Among them, the two most commonly used in fluid-flow problems are the Arnoldi [16] and the Krylov-Schur [23] algorithms. These methods can, in principle, extract any portion of the full spectrum through the repeated application of a restarting step. In practice, however, only the dominant modes (i.e. those associated with the eigenvalues of largest magnitude) can be computed in many applications; yet, these modes may not provide relevant information about the physics of the problem and, in some cases, may even be spurious. As far as the asymptotic stability behavior is concerned, the least stable modes (i.e., the modes with the largest exponential growth rate) are far more important. They can be computed by coupling an iterative eigenvalue algorithm to a time-stepping routine for the linearized equations of motion (abbreviated by the linear operator L) over a given time interval Δt[10]. This way, the iterative eigenvalue solver will efficiently extract the modes that are most amplified over a time interval Δt, that is to say, it extracts the least stable modes of L. The propagation time Δt, in general, affects the speed of convergence of the iterative solver, but does not influence which modes the solver will converge to.

This technique is generally sufficient for bounded flows that are governed by a limited number of (or even a single) dominant instability mechanism, since the associated spectrum consists of eigenvalues that are well separated. In this case, the principal eigenvalues are easy to isolate by the iterative algorithm. When multiple and competing mechanisms are at play, the spectrum is far more complicated, and physically relevant modes are more difficult to extract. In particular, eigenvalue clusters near the neutral axis, stemming from

continuous branches or even numerical artifacts, pose a great challenge to the convergence of the iterative algorithm. Even though unstable modes may still be extracted, the stable part of the spectrum quickly moves beyond the reach of the iterative algorithm; in this case, a different strategy is called for.

The region of convergence may be manipulated and adjusted by a rational transformation of the complex eigenvalue plane. The "shift-invert" method [16] allows the computation of the modes whose eigenvalues are closest to a complex shift parameter σ. But at each iteration of the eigenvalue solver, the method requires the solution of a linear system of the form $(L-\sigma \mathrm{I})x = b$. Most studies accomplish the latter solution using a direct LU decomposition which has to be performed once at the start and is used for all successive iterations, until the shift parameter σ is changed to access different parts of the spectrum. A variant of the shift-invert method, known as the Cayley transformation, yields better convergence, if an iterative solution of the linear system is chosen [18].

The LU decomposition is based on a matrix representation of the linear stability operator. Some global stability investigations used spectral discretization methods which resulted in a dense matrix of moderate size [2]. Later studies took advantage of a sparse representation, in particular, when the operator arises from a finite-element or finite-difference discretization [5]. In this case, the number of non-zero elements is proportional to the number of degrees of freedom N, making a sparse matrix representation convenient to handle computationally. Highly efficient multi-frontal LU solvers for large-scale sparse matrices are readily available (see e.g. [9, 3, 4]), but the sparsity of the output matrices is not always guaranteed. Even though the bandwidth of the factorization is not greater than that of the original matrix [11, p.152], all elements between the upper and lower band may be non-zero. Computing and storing the decomposition thus results in substantial memory requirements. For example, for the discretization of a two-dimensional problem with N degrees of freedom on a structured mesh, the bandwidth scales with $N^{1/2}$, in which case the LU decomposition would contain up to $\mathcal{O}(N^{3/2})$ non-zero elements. In three dimensions, as the bandwidth increases to $N^{2/3}$, the memory requirements go up as $N^{5/3}$. For a discretization of the compressible Navier-Stokes equations on a two-dimensional domain with 256×512 points using a finite-differences scheme with a six-points stencil, one can estimate that storing the LU decomposition requires about 80 GB of memory (work space requirements during the decomposition tend to be even larger), thus illustrating the limitation of this method for larger-scale problems. In some cases, appropriate reordering of the matrix entries can somewhat alleviate the problem by improving the sparsity of the factorization; this approach, however, does not provide a viable and extendable solution for large-scale problems.

An alternative that avoids the computation of the LU decomposition of the operator L consists of iterative algorithms [24] to solve the linear system arising from the shift-invert or Cayley transformation. Together with ILU-type preconditioners, this approach has been applied to incompressible [15] and compressible flows [18]; in [22], the authors use un-preconditioned iterative solvers for the computation of unstable modes in plasma flows. These methods yield a reduction of computational costs associated with the solution of the linear system, but they do not provide the same level of versatility as direct methods do. Indeed, if one chooses the shift parameter σ close to the spectrum of L, then $(L - \sigma Id)$ becomes ill-conditioned. In this case, the cost of preconditioning as well as the number of iterations for the linear solver to converge have to be assessed critically. In contrast, if σ is selected farther from the spectrum, the iterative linear solver is more likely to converge with a "cheap" preconditioner, but at the same time the focusing effect of the shift-invert transformation is rather weak; consequently, it may not be possible to extract the desired modes.

The present paper presents a method for selectively extracting modal information from a linear operator L without relying on the (iterative or direct) solution of a linear system. This approach has been inspired both by the "shift-invert" technique for the solution of eigenvalue problems [16] and by the selective frequency damping method of [1] for the computation of unstable steady flow. Similar to the latter method, we propose to use a relaxation procedure to selectively stabilize parts of the spectrum away from a chosen frequency shift, after which a standard Krylov method is employed to obtain the least stable modes of the relaxed system. Although the spectral transformation involved in the present "shift-relax" technique is somewhat less flexible than the "shift-invert" technique, its low memory requirement and ease of implementation make it suitable and attractive for large-scale stability computations of two- or three-dimensional flows.

2. Description of the method

2.1. Definition of the problem

Let the dynamics of the problem under consideration be governed by a set of non-linear equations of the form

$$\dot{\boldsymbol{q}} = F(\boldsymbol{q}), \tag{1}$$

where $\boldsymbol{q}$ is the state vector and F denotes a discrete integro-differential operator with appropriate boundary conditions. For simplicity, only finite-dimensional operators (which arise after spatial discretization) will be considered in this paper. We assume that this operator has a fixed point $\boldsymbol{q}_0$, such that $F(\boldsymbol{q}_0) = 0$. If this *base state* is stable to finite-amplitude perturbations, it can be computed by integrating the dynamical system (1) over a sufficiently long time. Algorithms such as the Newton-Krylov method [10] or Selective Frequency Damping (SFD) [1] can be used to obtain a base state even in unstable situations. The SFD method relies on low-pass filtering of the equations of motion in order to suppress high-frequency instabilities. The present method generalizes this approach in order to compute modes of a linear operator in a selected frequency band.

Let $L = \nabla_{\boldsymbol{q}} F(\boldsymbol{q}_0)$ be the linearization of F about the steady base state $\boldsymbol{q}_0$. Based on the decomposition $\boldsymbol{q} = \boldsymbol{q}_0 + \boldsymbol{q}'$, the dynamics of small perturbations $\boldsymbol{q}'$ is governed by the linear system

$$\dot{\boldsymbol{q}}' = L\boldsymbol{q}'. \tag{2}$$

Temporal modes of (2) are sought in the form

$$\boldsymbol{q}'(\boldsymbol{x}; t) = \widetilde{\boldsymbol{q}}(\boldsymbol{x}) \exp(-\mathrm{i}\omega t),$$

such that the spatial structure $\widetilde{\boldsymbol{q}}$ satisfies

$$-\mathrm{i}\omega\widetilde{\boldsymbol{q}} = L\widetilde{\boldsymbol{q}}. \tag{3}$$

A *complex* eigenfrequency ω is associated with the eigenmode $\widetilde{\boldsymbol{q}}$.

If an iterative solver is used to compute the least stable modes of (3) using an iterative eigenvalue solver, it is of advantage to consider the operator that takes a state $\boldsymbol{q}'(0)$ as an initial condition for (2) and returns the state $\boldsymbol{q}'(\Delta t)$ after a given time Δt. This operator is referred to as the *propagator* and can be formally written as

$$P = \exp(\Delta t L).$$

Krylov-based iterative eigenvalue solvers identify a subset of the eigenvalues $\lambda = \lambda_r + \mathrm{i}\lambda_i$ with the largest absolute value $|\lambda|$ (in the following, the subscript $_r$ and $_i$ respectively denote the real and imaginary parts of a complex number). Modes of P with the largest $|\lambda|$ are identical to modes of L with the largest *growth rate* ω_i. Even though the explicit computation of the matrix P would be an onerous task, its application to vectors can be easily performed by a standard time marching method; this makes the use of P appropriate for an iterative solver.

For some flows however, it may be interesting to investigate modes that belong to different frequency ranges, as these may correspond to different physical mechanisms (see for example the case of the flow around a leading edge [19] or that of supersonic jet flows [20]). In this case the objective is to compute the least stable modes with a real frequency ω_r close to a given value ω_0. The present method achieves this goal by applying a bandpass temporal filter to the propagator, such that modes with real frequency ω_r far from the target frequency $\omega_{0,r}$ are attenuated.

2.2. Filtering

In this section we recall standard filtering results applied to a signal $\boldsymbol{y}(t)$ with $t \in \mathbb{R}$. Its Fourier transform reads

$$\boldsymbol{y}(t) = \int_{-\infty}^{\infty} \hat{\boldsymbol{y}}(\omega) \exp(-\mathrm{i}\omega t)\, \mathrm{d}\omega.$$

We proceed by damping out the components of $\boldsymbol{y}(t)$ with frequencies far from a given value ω_0 using a standard first-order bandpass filter whose transfer function is given by

$$H(\omega) = \frac{1}{1 - \mathrm{i}\dfrac{\omega - \omega_0}{\tau}}. \tag{4}$$

The filtered signal $\bar{\boldsymbol{y}}(t)$ is then given by the convolution

$$\bar{\boldsymbol{y}}(t) = \int_{-\infty}^{\infty} H(\omega)\hat{\boldsymbol{y}}(\omega)\exp(-\mathrm{i}\omega t)\,\mathrm{d}\omega,$$

which satisfies the filtered ordinary differential equation

$$\dot{\bar{\boldsymbol{y}}} = -\mathrm{i}\omega_0\bar{\boldsymbol{y}} - \tau(\bar{\boldsymbol{y}} - \boldsymbol{y}). \tag{5}$$

The above bandpass filter is centered about the target frequency ω_0 and has a half width at half maximum of $\sqrt{3}\tau$.

The presented analysis applies to signals defined for all times. If one wants to use the differential equation (5) to filter a signal defined only for $t \geq 0$, initial conditions have to be specified. The overall frequency selection effect, however, will prevail independent of initial conditions, if the differential equations have been sufficiently advanced in time. In this way, the differential equation (5) provides a way to filter a signal without having to store its entire history.

2.3. Selective frequency damping of a linear dynamical system

Following [1], let us consider the following linear dynamical system:

$$\dot{\boldsymbol{q}}' = L\boldsymbol{q}' - \chi(\boldsymbol{q}' - \overline{\boldsymbol{q}}'), \tag{6a}$$

$$\dot{\overline{\boldsymbol{q}}}' = -\mathrm{i}\omega_0\overline{\boldsymbol{q}}' - \tau(\overline{\boldsymbol{q}}' - \boldsymbol{q}'). \tag{6b}$$

Equation (6b) represents a differential equation corresponding to the bandpass filter introduced above. The signal $\overline{\boldsymbol{q}}'$ is therefore a filtered version of $\boldsymbol{q}'$, in which frequency components far from the target frequency ω_0 are damped.

The right-hand side of (6a) is a sum of two terms. The first one represents the linear operator, while the second part acts as a proportional controller that drives the variable $\boldsymbol{q}$ towards its filtered counterpart $\overline{\boldsymbol{q}}$.

The SFD procedure of [1] applies the same filtering with $\omega_0 = 0$ to a non-linear operator instead of L in (6). In this case, any fixed point of F corresponds to a fixed point of the extended system, the filtered state $\overline{\boldsymbol{q}}'$ being then equal to the full state. However, the stability of the fixed point of the extended system is modified and trajectories differ. Our shift-relax (SR) approach relies on the observation that the frequency selection procedure not only preserves the fixed points of non-linear operators, but also the eigenmodes of linear systems, as will be demonstrated next.

In order to study the relationship between the spectra associated with the original linear dynamical system (2) and the SR extension (6), we introduce the composite filtered operator $\mathcal{F}$ defined as

$$\mathcal{F} \equiv \left(\begin{array}{c|c} L - \chi\mathrm{Id} & \chi\mathrm{Id} \\ \hline \tau\mathrm{Id} & (-\mathrm{i}\omega_0 - \tau)\mathrm{Id} \end{array}\right) \tag{7}$$

such that (6) can be rewritten as

$$\begin{pmatrix} \dot{\boldsymbol{q}}' \\ \dot{\overline{\boldsymbol{q}}}' \end{pmatrix} = \mathcal{F}\begin{pmatrix} \boldsymbol{q}' \\ \overline{\boldsymbol{q}}' \end{pmatrix}.$$

If the state vector $\boldsymbol{q}'$ contains N elements, then a $2N$-dimensional eigenvector of $\mathcal{F}$ associated with the complex eigen-frequency Ω, i.e.

$$\mathcal{F}\widetilde{\boldsymbol{Q}} = -\mathrm{i}\Omega\widetilde{\boldsymbol{Q}},$$

can be decomposed into two N-dimensional components, $\widetilde{\boldsymbol{Q}} = (\widetilde{\boldsymbol{q}}, \widetilde{\widetilde{\boldsymbol{q}}})^T$. According to (6b), these two components are related by

$$\widetilde{\widetilde{\boldsymbol{q}}} = \frac{1}{1 - \mathrm{i}\dfrac{\Omega - \omega_0}{\tau}} \widetilde{\boldsymbol{q}}.$$

Consistent with the design of the filter, the scalar factor between $\widetilde{\widetilde{\boldsymbol{q}}}$ and $\widetilde{\boldsymbol{q}}$ can be related to the transfer function (4). We can substitute this result back into (6a) to obtain

$$L\widetilde{\boldsymbol{q}} = -\mathrm{i}\omega(\Omega)\widetilde{\boldsymbol{q}} \tag{8}$$

with

$$\omega(\Omega) = \Omega + \mathrm{i}\chi \left(1 - \frac{1}{1 - \mathrm{i}\dfrac{\Omega - \omega_0}{\tau}} \right). \tag{9}$$

Equation (8) shows that $\widetilde{\boldsymbol{q}}$, i.e. the vector corresponding to the first N elements of $\widetilde{\boldsymbol{Q}}$, is an eigenvector of L. This justifies the use of the SR system (6) as a spectral transformation, as the modes of L can be recovered from those of $\mathcal{F}$.

Equation (9) characterizes the mapping between the spectra of L and $\mathcal{F}$. For any eigenvector $\widetilde{\boldsymbol{Q}} = (\widetilde{\boldsymbol{q}}, \widetilde{\widetilde{\boldsymbol{q}}})^T$ of $\mathcal{F}$ with complex frequency Ω, $\widetilde{\boldsymbol{q}}$ is an eigenvector of L with complex frequency $\omega(\Omega)$ given by (9). This latter equation can be re-arranged as a second-order polynomial in Ω where ω appears as a parameter. This shows that two values of Ω correspond to a single value of ω, which is consistent with the fact that the dimension of $\mathcal{F}$ is twice the dimension of L.

Proceeding with the analysis of the mapping between the spectra of the original operator L and its SR extension $\mathcal{F}$, let us introduce the following scaled variables

$$(\omega', \Omega', \chi') = \frac{1}{\tau}(\omega - \omega_0, \Omega - \omega_0, \chi).$$

Equation (9) can then be simplified as follows

$$\omega' = \Omega' + \mathrm{i}\chi' \left(1 - \frac{1}{1 - \mathrm{i}\Omega'} \right). \tag{10}$$

It therefore appears that after a shift of origin (given by the parameter ω_0) and a scaling (given by the factor τ) of the complex-frequency plane, the transformation can be studied in terms of one single parameter $\chi' = \chi/\tau$.

Effect of χ'. The parameter χ' measures the gain of the proportional controller relative to the frequency scale τ. The analysis (given in detail in Appendix A) shows how χ' influences the spectral transformation. We observe that the transformation is self-similar with respect to two transformations of ω' and Ω' : first, by different shifts of origins of these two variables and, second, by a scaling by the factor ${\chi'}^{-1/2}$. The shift of origin for Ω' has no influence on the frequency selection effect of the filter, as it changes neither the order in which modes will be extracted nor the separation between the eigenvalues of the filtered propagator. The scaling is more relevant, but its effect on the transformation is the same as that of τ. Acting on χ' therefore adds no additional flexibility to the method. In an effort to keep the scaling of the complex plane and the shift of origin as two parameters, we choose $\chi' = 1$ throughout our study and only use ω_0 and τ as changing parameters.

Study of the transformation for $\chi' = 1$. For a given value of ω', (10) is a second-order polynomial in Ω'. As mentioned previously, this results in two solution branches, for which an analytic expression can easily be obtained. We note that the distinction between the two branches is not unique, as it depends on the location of the branch cut for the square root function with complex arguments. In the following representation we chose the common branch cut for negative real arguments of the square root.

Figure 1a, b illustrates the mapping between the original spectral plane ω' and the two associated values of $\Omega'_{1,2}$ by the SR transformation, respectively indicated by blue and black lines, together with the transformation of several sample values of ω' represented by colored symbols. These values are chosen arbitrarily for illustration purposes. The solid and dashed lines in figure 1b are, respectively, the images of iso-ω'_i- and iso-ω'_r-lines in the ω'-plane represented in figure 1a. The mapping (with the chosen branch cut) defines two regions of the complex Ω'-plane. Values of Ω' inside the unit circle centered at $\Omega' = -\mathrm{i}$ correspond to the first root Ω'_1 while values outside the circle correspond to the second root Ω'_2. Accordingly, the sample values represented by colored symbols in figure 1a has two images in the Ω'-plane. We notice, however, that neither the mapping $\omega' \to \Omega'_1$ nor the mapping $\omega' \to \Omega'_2$ is continuous.

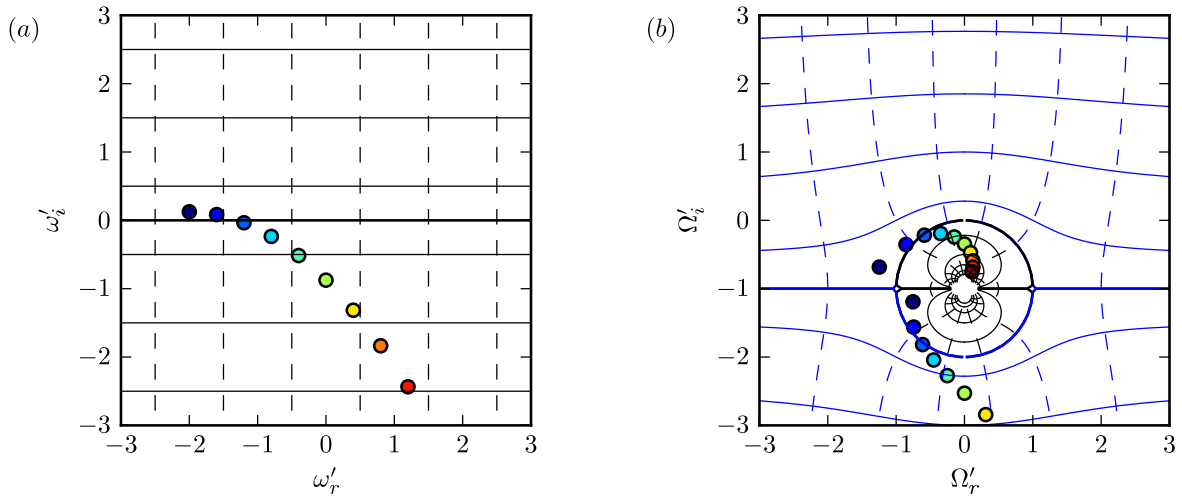

Figure 1: Mapping between the original spectral plane ω' (a) and its SR-transformed image Ω' (b). The colored symbols correspond to sample values.

The images of the sample values in figure 1b suggest another distinction between the two images of ω'. We respectively define ${\Omega'}^+$ and ${\Omega'}^-$ as the images of ω' such that the following relation involving the transformed growth rates is satisfied

$$ {\Omega'}_i^-(\omega') \leq -1 \leq {\Omega'}_i^+(\omega'). $$

See Appendix A for a proof. As τ is real and positive, the above distinction between the two branches results in

$$ \Omega_i^- \leq \omega_{0,i} - \tau \leq \Omega_i^+, $$

expressed in terms of the non-scaled variables.

The least stable modes of the SR operator $\mathcal{F}$ (given in (7)) will then be extracted by applying an eigenvalue solver to the filtered propagator

$$ \mathcal{P} = \exp(\mathrm{i}\Delta t \mathcal{F}) \tag{11} $$

as motivated in § 2.1. This will extract the least stable modes of the filtered operator $\mathcal{F}$. Consequently, we can restrict our attention to the ${\Omega'}^+$ branch. Furthermore, as only the growth rate rather than the frequency decides which modes will be extracted, the relevant features of the transformation can be studied in terms of the single-valued real function $\omega' \to {\Omega'}_i^+$. This function is represented in figure 2.

Three regions of the ω'-plane can be identified:

- For $1 \lesssim \omega'_i$, the transformed growth rate ${\Omega'}_i^+$ behaves similar to the un-transformed growth rate ω'_i. No significant dependency with ω'_r is observed, indicating that no noticeable frequency selection occurs.

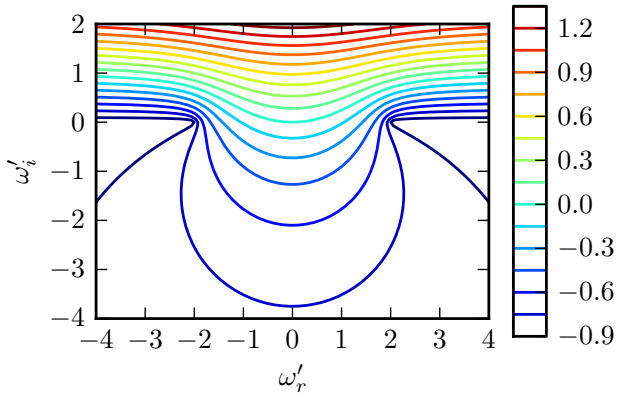

Figure 2: Imaginary part of the eigenvalue of the SR operator $\Omega_i'^{+}(\omega')$ as a function of the eigenvalue ω' of the origin for $\chi' = 1$.

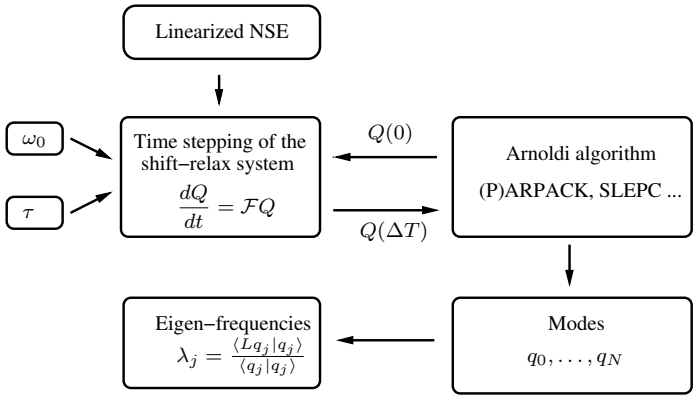

Figure 3: Practical implementation of the method

- For $-2 \lesssim \omega_i' \lesssim 1$, the value of $\Omega_i'^{+}(\omega')$ exhibits strong dependency on the real frequency ω_r'. Along a line of constant ω_i, the value of $\Omega_i'^{+}(\omega')$ reaches a maximum for $\omega_r = 0$, confirming that the filter plays the expected role of stabilizing modes with real frequencies far from $\omega_{0,r}$.
- For $\omega_i' \lesssim -2$, $\Omega_i'^{+}(\omega')$ is approximately constant. The dynamics of the SR system is dominated by the control term in (6a) which conceals the dynamics of the linear operator L.

The above representation allows to determine the behavior of the proposed method. For $\omega_i \gtrsim \omega_{0,i} + \tau$, the spectral transformation produces results similar to that of the propagator approach (see § 2.1 and [10]). The frequency selection effect is insignificant in this region. Strong frequency selection is achieved in the range of frequencies $\omega_{0,i} - 2\tau \lesssim \omega_i \lesssim \omega_{0,i} + \tau$, as the effect of the bandpass filter is clearly present. Modes with real frequencies outside a bandwidth of order τ centered around $\omega_{0,r}$ are damped. In this range of growth rates, modes with real frequencies close to $\omega_{0,r}$ will be extracted first. All modes with a growth rate $\omega_i \lesssim \omega_{0,i} - 2\tau$ will map to essentially the same growth rate for the SR operator. These modes will be difficult to distinguish with an iterative eigenvalue solver.

2.4. Numerical considerations

Implementation. A practical implementation of the present method requires only few additions to a standard DNS code. These are summarized in figure 3. First, a routine evaluating the linearized Navier-Stokes operator is needed. The linearization may be carried out by hand, as done in the examples given in this paper, or numerically "on the fly" from a non-linear routine, as done in [14].

Next, the eigenvalue extraction is performed. Several libraries for both sequential and parallel implementations may be used for this task. The Krylov-Schur solver provided in the SLEPc library [23] is used here to extract the eigenmodes of the SR operator, with 60 Krylov vectors. Better convergence behavior has been observed compared to the Implicitly Restarted Arnoldi Method (IRAM), which is more frequently used for the computation of modes in fluid flow problems[16]. In [22], the authors report good results using the "harmonic extraction" solver of SLEPc for frequency selection. For our cases, this method has not produced the desired outcome.

Finally, only minor changes in order to integrate the filtering procedure into a standard time-stepping routine are necessary. The algorithm for the time stepping of the SR dynamical system is exemplified using an explicit Euler scheme as outlined below. The variables q_1 and q_2, respectively, represent the state and its filtered counterpart, L is the linear flow operator, and δt is a discrete time step.

1: $t \leftarrow 0$
2: **while** $t \leq \Delta t$ **do**
3: $\quad r_1 \leftarrow L(q_1)$
4: $\quad r_1 \leftarrow r_1 - \chi * (q_1 - q_2)$
5: $\quad r_2 \leftarrow \mathrm{i}\omega_0 * q_2 - \chi * (q_2 - q_1)$
6: $\quad q_1 \leftarrow q_1 + \delta t * r_1$
7: $\quad q_2 \leftarrow q_1 + \delta t * r_2$
8: $\quad t \leftarrow t + \delta t$
9: **end while**

The algorithm differs from standard time stepping by the additional lines 4, 5 and 7. These correspond to a small number of operations compared to the application of the operator L, in particular, when high-order schemes are employed; the SR computations are therefore only slightly slower than regular time-stepping, and they can be just as efficiently parallelized.

Memory requirements. The memory requirement of the present method is twice that of a standard propagator technique, as the dimension of the phase space is doubled due to the presence of the filtered variables. If the eigenvalue solver and the time stepper respectively require ncv and nts vectors of size N (the number of degrees of freedom associated with the discretization of the equations) as workspace, most of the memory requirement will originate from the storage of these $2N(ncv + nts)$ values. For the discretization of the compressible Navier-Stokes equations mentioned in the introduction with $ncv = 60$, $nts = 20$ and double precision complex arithmetics, the program would require $2 \times 5 \times 256 \times 512 \times 80 \times 16$ B ≈ 1.6 GB of memory, which is substantially less than the 80 GB required for the sparse LU decomposition alone.

Effect of the propagation time. The effect of the propagation time on the SR operator is the same as for the classical propagator method [10]. The actual value of the propagation time Δt should not influence which subset of modes will be extracted. The propagation time will however affects the convergence of the eigenvalue solver. If Δt is small, only a few time marching steps are required in each iteration; nonetheless, a large number of iterations will be necessary in order to reach a desired accuracy. It will also require a large number of restarts, which ultimately may affect robustness. On the other hand, if Δt is too large, each iteration will be rather costly since it consists of many time steps, and the method will make less use of the orthogonalization step. A balance has to be found between the computational time needed to propagate the solution forward in time, the cost associated with the eigenvalue solver and the robustness of the restarting procedure.

Time stepping accuracy. Numerical time stepping methods such as Euler and Runge-Kutta schemes correspond to an approximation of the exponential matrix propagator by a matching polynomial. Such an approximation preserves the modes: it therefore introduces no error on the computed modes. In practical applications, the time step δt of the time-stepping routine is much smaller than the characteristic time scale of modes one wishes to compute. As a consequence, the spectrum transformation introduced by numerical time stepping will be nearly exponential in the range of eigenfrequencies of interest, such that the rules derived earlier for the choice of parameters remain valid.

Eigenvalue recovery. As explained in § 2.3, recovering the eigenvectors of L is straightforward, as they correspond to the first N components of the eigenvectors of the SR propagator. The eigenfrequency ω associated with an eigenvector $\boldsymbol{q}$ of L may conveniently be obtained by computing the Rayleigh quotient

$$-\mathrm{i}\omega = \frac{\langle \boldsymbol{q}|L\boldsymbol{q}\rangle}{\langle \boldsymbol{q}|\boldsymbol{q}\rangle}. \tag{12}$$

Alternatively, the eigenvalue Ω of the SR operator may be computed from the eigenvalue λ of the SR propagator via

$$\Omega = \frac{\log(\lambda)}{-\mathrm{i}\Delta t}, \tag{13}$$

and (9). Method (12) has three advantages over the latter method. First, as the logarithm is multivalued, the above formula yields the imaginary part only if one knows the Riemann sheet Ω lies on, i.e. for example that $0 \leq \Omega_r \leq 2\pi/\Delta t$. Second, the numerical time stepping makes (13) inexact: as discussed in § 2.4, the transformation introduced by time-stepping is not exactly exponential but rather a polynomial approximation. This problem does not arise for the Rayleigh quotient (12). Finally, (12) minimizes the residual $\|L\boldsymbol{q} + \mathrm{i}\omega\boldsymbol{q}\|/\|\boldsymbol{q}\|$, the norm being that corresponding to the inner product in (12). This inner product may include weights that select specific flow quantities of regions. In all computation presented in § 3 and 4, the l^2 inner product on the state vector components is chosen as it is the one used in the Krylov–Schur algorithm.

3. Application to the local and global stability analysis of a compressible jet

3.1. Governing equations for local and global computations

We consider a compressible jet of radius R, with characteristic velocity U_0, density ρ_0 and temperature T_0 measured on the centerline, discharging into a fluid at rest with density ρ_∞ and temperature T_∞. These same quantities are used to make the problem non-dimensional. In a cylindrical coordinate system (x, r, θ), the nonlinear governing equations are expressed in terms of the conservative flow variables $\boldsymbol{q} = (\rho, \rho u_x, \rho u_r, \rho u_\theta, \rho E)^T$, where ρ is the density, $\boldsymbol{u} = u_x\boldsymbol{e}_x + u_r\boldsymbol{e}_r + u_\theta\boldsymbol{e}_\theta$ is the flow velocity, and E denotes the total energy [25]. The Reynolds, Mach and Prandtl numbers are defined as

$$\mathrm{Re} = \frac{U_0 R \rho_0}{\mu}, \qquad \mathrm{Ma} = \frac{U_0}{c_0}, \qquad \mathrm{Pr} = \frac{\mu C_p}{\kappa} = 1, \tag{14}$$

with c_0 the reference speed of sound on the jet axis, C_p the ambient specific heat at constant pressure, μ the dynamic viscosity and κ the thermal conductivity of the fluid. The fluid properties C_p, μ and κ are assumed to be constant throughout the flow.

For the purpose of a stability analysis, the flow variables $\boldsymbol{q}$ are decomposed into a steady axisymmetric base flow $\boldsymbol{q}^b$ and unsteady perturbations $\boldsymbol{q}'$, such that $\boldsymbol{q}(x, r, \theta, t) = \boldsymbol{q}^b(x, r) + \boldsymbol{q}'(x, r, \theta, t)$. The governing equations are then linearized around $\boldsymbol{q}^b$, and a normal mode ansatz for $\boldsymbol{q}'$ allows to characterize the temporal growth or decay of perturbation eigenmodes of the linear system. Both local (§ 3.2) and global (§ 3.3 and 4) normal modes will be considered in the following. Local theory assumes the flow to be infinite, parallel and uniform in the $x-$ direction. In this case, perturbations are Fourier-transformed in x, leaving only r as an eigendirection. Global theory, by contrast, considers spatially developing base flows, and accounts for boundary conditions at the inlet and outlet. In the global framework, both r and x are thus eigendirections, which leads to a system size that precludes the use of direct eigenvalue solvers.

3.2. Validation: direct computation of local temporal eigenmodes

A validation of the present SR propagator method is conducted by computing the eigenmodes of a *parallel* jet of infinite streamwise extent. This test case represents the local stability problem, as it has been widely

used to describe the stability properties of slowly varying flows [13]. The base flow is prescribed as

$$u_x^b = \frac{1}{2}\left\{1 + \tanh\left[2\left(r - \frac{1}{r}\right)\right]\right\}, \tag{15a}$$

$$u_r^b = u_\theta^b = 0, \tag{15b}$$

$$T^b = S + (1-S)u_x^b + \frac{\gamma-1}{2}\mathrm{Ma}^2 u_x^b(1-u_x^b), \tag{15c}$$

$$\rho^b = {T^b}^{-1}, \tag{15d}$$

from which we obtain the total energy $\rho^b E^b = \gamma^{-1}(\gamma-1)^{-1}Ma^{-2} + \rho^b {u_x^b}^2/2$, with uniform pressure $p^b = (\gamma \mathrm{Ma}^2)^{-1}$. The ratio of specific heats is taken as $\gamma = 1.4$, and $S = T_\infty/T_0$ denotes the ambient-to-jet temperature ratio. A hot jet with $S = 0.5$ is chosen for the present configuration, along with the parameters $\mathrm{Re} = 500$, $\mathrm{Ma} = 0.4$ and $\mathrm{Pr} = 1$.

Azimuthal periodicity and streamwise invariance justify a normal mode ansatz of the form

$$\boldsymbol{q}'(x,r,\theta,t) = \widetilde{\boldsymbol{q}}(r)\exp\left[\mathrm{i}(kx + m\theta - \omega t)\right] + cc, \tag{16}$$

where cc stands for the complex conjugate. Within the framework of a temporal stability analysis, the complex frequency ω is sought as a function of prescribed streamwise and azimuthal wave-numbers $k \in \mathbb{R}^+$ and $m \in \mathbb{Z}$.

One-dimensional reference solution. Upon substitution of the base flow (15) and normal mode perturbations (16) into the linearized equations of motion, only the radial coordinate direction needs to be discretized. We use a compact finite-difference scheme [17] for the spatial discretization and impose homogeneous Dirichlet boundary conditions at $r = 150$, leading to the discrete local temporal eigenvalue problem of the form

$$\mathbf{A}(k,m)\widetilde{\boldsymbol{q}} = \omega \mathbf{B}\widetilde{\boldsymbol{q}}\,. \tag{17}$$

All eigenmodes $(\omega, \widetilde{\boldsymbol{q}})$ are then computed via a QR-algorithm. The most relevant part of the spectrum for values $k = m = 1$ is shown in figure 4*a*. Three families of eigenmodes may be distinguished based on their frequency ω_r, their growth rate ω_i, and their spatial distributions of azimuthal vorticity (figure 4*b*) and dilatation $\boldsymbol{\nabla}\cdot\boldsymbol{u}$ (figure 4*c*).

Vortical perturbations localized in the fluid at rest outside the jet form the classical continuous spectrum of unbounded shear flows [26] with near-zero real frequency. Due to the finite size of the numerical domain, continuous branches results in densely clustered discrete modes in the discretized problem. These are represented by blue symbols that line up close to the $\omega_r = 0$ axis in figure 4*a*. Acoustic waves in the freestream form two continuous branches, both plotted in red in figure 4*a*. These are characterized by very slow temporal decay ($\omega_i \approx 0$) and frequencies in the continuous ranges $\omega_r \leq -k\sqrt{S}/\mathrm{Ma}$ and $\omega_r \geq k\sqrt{S}/\mathrm{Ma}$. These cut-off frequency $\pm k\sqrt{S}/\mathrm{Ma}$ corresponds to cylindrical acoustic waves traveling parallel to the jet axis at the speed of sound c_∞ in the outer flow. Real parts of vorticity and dilatation fields are shown in figures 4*b, c* as a function of r for particular modes (vortical mode with $\omega = 2.24.10^{-6} - 1.49.10^{-3}\mathrm{i}$ in blue and acoustic mode with $\omega = 2.03 - 1.91.10^{-3}\mathrm{i}$ in red). A fourth branch of modes is represented by green symbols in figure 4*a*. This branch consists of discrete modes with a single unstable one marked by a cross. The spatial structure of the unstable eigenmode is plotted in green in figures 4*b, c*. This mode displays strong vorticity perturbations inside the jet shear-layer around $r = 1$, and nearly no dilatation perturbation. As the discrete modes (green symbols in figure 4*a*) have real frequencies below the acoustic cut-off value (i.e. a subsonic phase velocity), no sound is radiated by these modes.

3.3. Local eigenmodes via the SR method on a two-dimensional periodic domain

In order to demonstrate the use of the SR technique, it is applied to reproduce a selected part of the spectrum shown in figure 4*a*. Local modes may be computed as global eigenmodes on a two-dimensional (x,r) domain,

$$\boldsymbol{q}'(x,r,\theta,t) = \widetilde{\boldsymbol{q}}(x,r)\exp\left[\mathrm{i}(m\theta - \omega t)\right]\,, \tag{18}$$

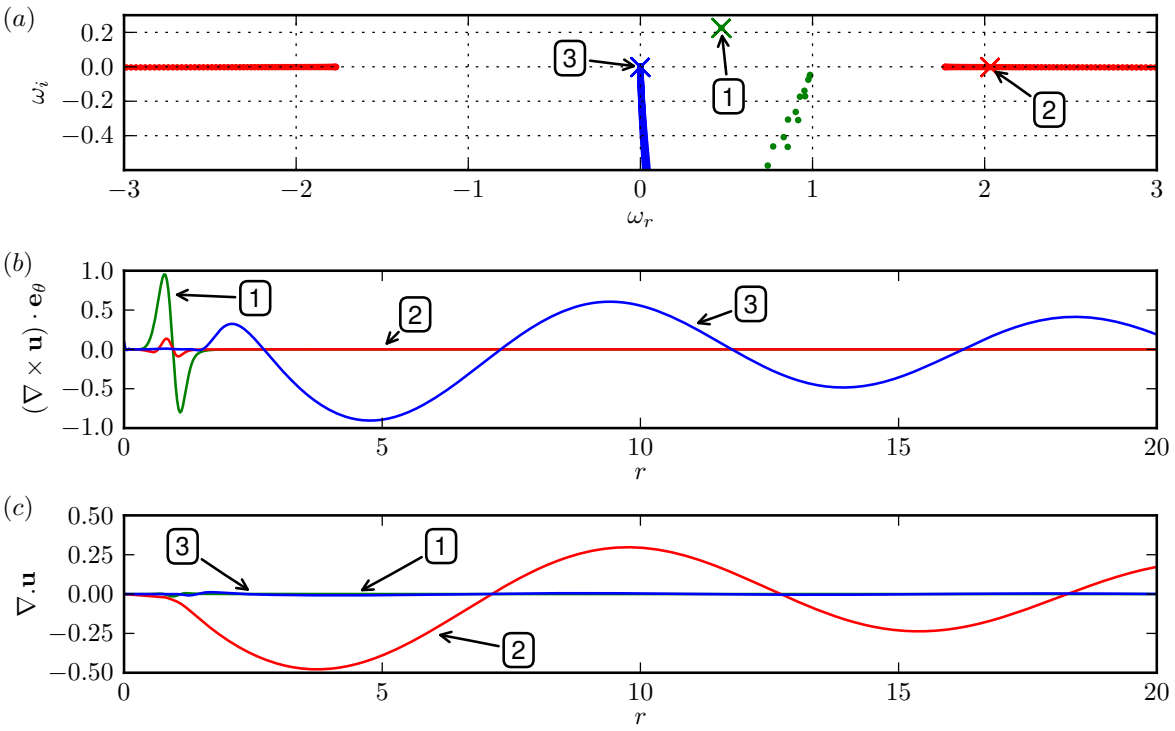

Figure 4: Temporal spectrum directly computed with the QR algorithm for the parallel base flow given by (15) for Re = 500, Ma = 0.4 and Pr = 1, and for waves number $k = 1$ and $m = 1$. (a) The eigenvalue spectrum is displayed in terms of real frequency ω_r' and temporal growth rate ω_i' of the modes. Blue symbols correspond to vortical modes in the outer flow; red symbols to acoustic modes in the outer flow and green ones to shear-layer modes. (b) The real part of vorticity eigenfunction for three selected modes (indicated by large color crosses in (a)) (Green: $\omega = 0.471+0.226$i, label 1 in (a); red: $\omega = 2.03-1.91.10^{-3}$i, label 2 in ($a$); Blue: $\omega = 2.24.10^{-6} - 1.49.10^{-3}$i, label 3 in ($a$)). ($c$) The real part of dilatation eigenfunction is represented for the same modes as in (b).

with periodic boundary conditions in x and with a streamwise extent $0 \leq x \leq 2\pi/k$. Using a two-dimensional discretization allows the use of the same code here (for a parallel base flow) and in § 4 (for non-parallel base flow), except for different boundary conditions. The base flow in the present case is still parallel, given by (15). The objective is to compute a number of least stable discrete eigenmodes of the shear-layer type (green symbols in figure 4a).

If a standard Krylov technique were to be applied to the propagator of the linear equations of motion alone, only the single unstable shear-layer mode could be extracted, all other discrete modes being masked by the less stable acoustic (red in figure 4) or vortical (blue) branches. The SR technique allows to stabilize all modes outside a region of interest of the spectrum, and thereby may give access to otherwise masked parts of the spectrum, in particular here by stabilizing the continuous branches.

The extended linear system (6) is discretized on an orthogonal grid, resolving the domain $0 \leq r \leq 15$, $0 \leq x \leq 2\pi/k$ with 30×256 points. Explicit 5^{th}-order centered finite differences in combination with a spatial filtering scheme [6] are used for the spatial derivatives. The spatial filter merely suppresses numerical instabilities of the finite-difference scheme; it is unrelated to the temporal filtering employed by the SR method. Matrix-free time stepping of the extended linear equations is performed using a 3^{rd}-order Runge–Kutta algorithm. For the purpose of validation against the results of § 3.2, only modes with a streamwise wavenumber $k = 1$ are sought, and higher harmonics of the periodic domain are continuously filtered out during the time stepping, by means of an FFT in x.

Choice of transformation parameters. In order to focus on the green branch represented in figure 4*a*, appropriate parameter values for χ, τ and ω_0 must be chosen. As discussed in § 2.2, a value of $\chi' = 1$ is maintained, such that $\chi = \tau$. The frequency shift ω_0 selects the region of interest in the frequency plane; a choice of $\omega_0 = 1 + 0.2\mathrm{i}$ has been found to be suitable. The parameter τ determines the width of the bandpass filter. It should be chosen sufficiently small to efficiently damp undesired modes (here, the blue and red branches) but large enough such that the modes of interest achieve growth rates $\omega_i \gtrsim \omega_{0,i} - 2\tau$, as discussed in § 2.3. A value of $\tau = 0.5$, yielding $\chi = 0.5$, represents a good compromise for the present case. The propagation time is set to $\Delta t = 0.5$.

Results. Ten eigenvalues obtained with the SR method are shown as black circles in figure 5, alongside the reference solution (identical to figure 4*a*). The agreement is excellent, with relative errors smaller than 10^{-4} on both the eigenvalues and the eigenmodes (in L^∞ norm). The spectral transformation with the present choice of parameters successfully selects the least stable shear-layer modes. Contour lines in figure 5 indicate the transformed growth rate $\Omega_i(\omega)$ that governs the mode selection by the SR method.

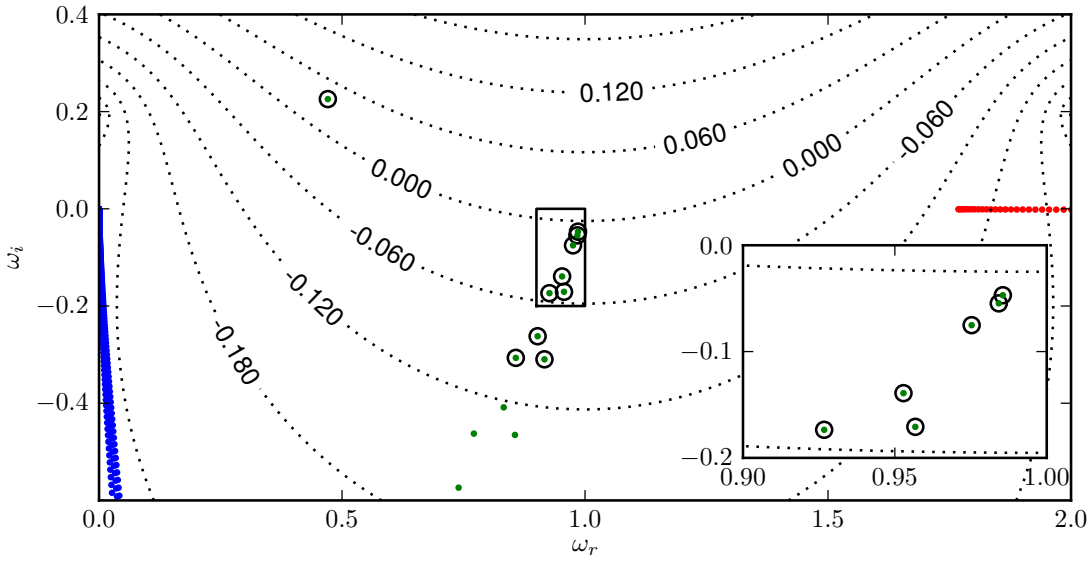

Figure 5: Application of the SR method to the computation of local modes of a compressible jet flow for the same parameter settings as in figure 4. The spectrum from figure 4*a* is reproduced with the same conventions. The ten modes computed with the SR method are denoted by black circles. The dotted lines represent isocontours of the growth rate Ω_i^+ of the filtered propagator, based on parameters $\omega_0 = 1 + 0.2\mathrm{i}$ and $\tau = \chi = 0.5$, confirming that the computed eigenvalues correspond to the largest Ω_i^+. The insert on the bottom right of the figure shows a close-up view on the region marked by a black rectangle

4. Application: global eigenmodes of a compressible jet

4.1. Non-parallel base flow

The SR method is now applied to compute global modes (18) of a non-parallel jet. The geometry of the computational domain is represented in figure 6. The jet exits from an idealized nozzle, modeled as an infinitely thin adiabatic wall at $r = 1$ and $x \leq 0$. Only the upper half-plane $r > 0$ is resolved in the calculations, and appropriate symmetry conditions for axisymmetric flow are imposed on the jet axis $r = 0$. In order to control the jet profile at $x = 0$ (diffusive effects inside the pipe can be particularly important at low Reynolds and high Mach numbers), velocity and temperature profiles are imposed at $x = x_0$, close to the jet nozzle. The Navier–Stokes equations are solved downstream of x_0 (domain II in figure 6*a*), with local

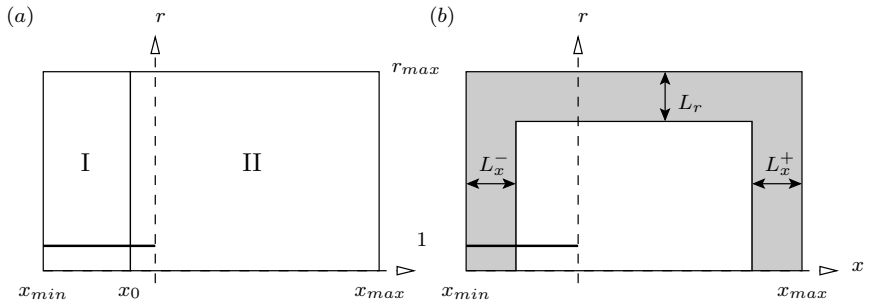

Figure 6: Computational domains for (a) base flow and (b) global mode computations. The parameter values for these computations are: $x_{min} = -200$, $x_{max} = 300$, $r_{max} = 250$, $x_0 = -2$, $L_x^+ = L_x^- = L_r = 150$. The base flow is taken to be parallel in region I, whereas the Navier–Stokes equations are solved in region II.

one-dimensional (LODI) boundary conditions [21] on the numerical boundaries at x_{min}, x_{max} and r_{max}. The same explicit finite-difference scheme as described in § 3.3 is used. A steady solution of the nonlinear Navier–Stokes equations, computed via the SFD method of [1] for Re = 100, Ma = 0.75, Pr = 1 and $S = 1$ is taken as a base flow. A parallel flow region is added upstream of x_0 (domain I in figure 6a) to extend the base flow to the domain used for the linear stability calculations. Axial velocity and angular vorticity distributions of the spatially spreading base flow are shown in figure 7a, b. The momentum thickness

$$\theta(x) = \int_0^{\alpha} \frac{\rho^b(r,x)u^b(r,x)}{\rho^b(0,x)u^b(0,x)} \left(1 - \frac{u^b(r,x)}{u^b(0,x)}\right) r\mathrm{d}r, \quad \alpha = \begin{cases} 1 & x \leq 0 \\ \infty & x > 0 \end{cases}$$

is displayed in figure 7c, and selected axial velocity profiles are shown in figure 7d.

Temporal eigenmodes of the linearized Navier–Stokes equations, commonly referred to as "global modes", are computed on the domain displayed in figure 6b. Non-reflecting boundary conditions given by [7] are employed at the inflow, outflow and upper boundary. Furthermore, perturbation quantities are artificially attenuated in sponge layers [8], indicated by the outer gray regions in figure 6b, in order to further minimize spurious reflections. Only axisymmetric modes ($m = 0$) are computed, and symmetry conditions on the jet axis are imposed accordingly. The numerical domain spanned by $-200 \leq x \leq 300$ and $0 \leq r \leq 250$ is discretized with 1024×512 grid points.

Five eigenvalues were requested for each of nine shift parameters ω_0 with $0.3 \leq \omega_{0,r} \leq 0.75$ and $\omega_{0,i} = 0.05$, represented by black diamonds in figure 8a. Note that SLEPc may return more than the requested number of eigenvalues. Parameters $\tau = \chi = \Delta t = 0.1$ were used in all calculations. The resulting eigenfrequencies are represented in figure 8a in the complex ω- plane and form a discrete branch of solutions. For each value of ω_0, one isocontour of the growth rate Ω_i^+ of the filtered propagator is drawn, corresponding to the growth rate of the most stable mode computed with each particular shift; no eigenfrequency other than those computed should lie above these parabola-shaped curves.

For $\omega_0 = 0.8 + 0.05\mathrm{i}$, five eigenvalues were first requested, as for the other values of the frequency shift. The computation was then continued to yield a total of fifteen modes. This portion of the spectrum is displayed in more detail in figure 8c, together with iso-contours of the growth rate of the filtered propagator. The first five modes that have been found are marked by red circles. Among the additional requested modes, several are found to lie on a separate, slightly more attenuated branch. The spatial structure of the real part of vorticity perturbations associated with three eigenmodes of the upper branch, marked by labels in figure 8, are displayed in figure 9. Perturbations are concentrated in the jet shear layer region, suggesting an inflectional instability mechanism. The time evolution of these modes show that the vortical structures represented in figure 9 propagate downstream at a phase velocity of about half the jet centerline velocity; as a consequence, their typical axial wavelength decreases with increasing real frequency. Modes belonging to the more attenuated branch, which is only detected in figure 8 for the shift $\omega_0 = 0.8 + 0.05\mathrm{i}$, display a very similar structure (not shown).

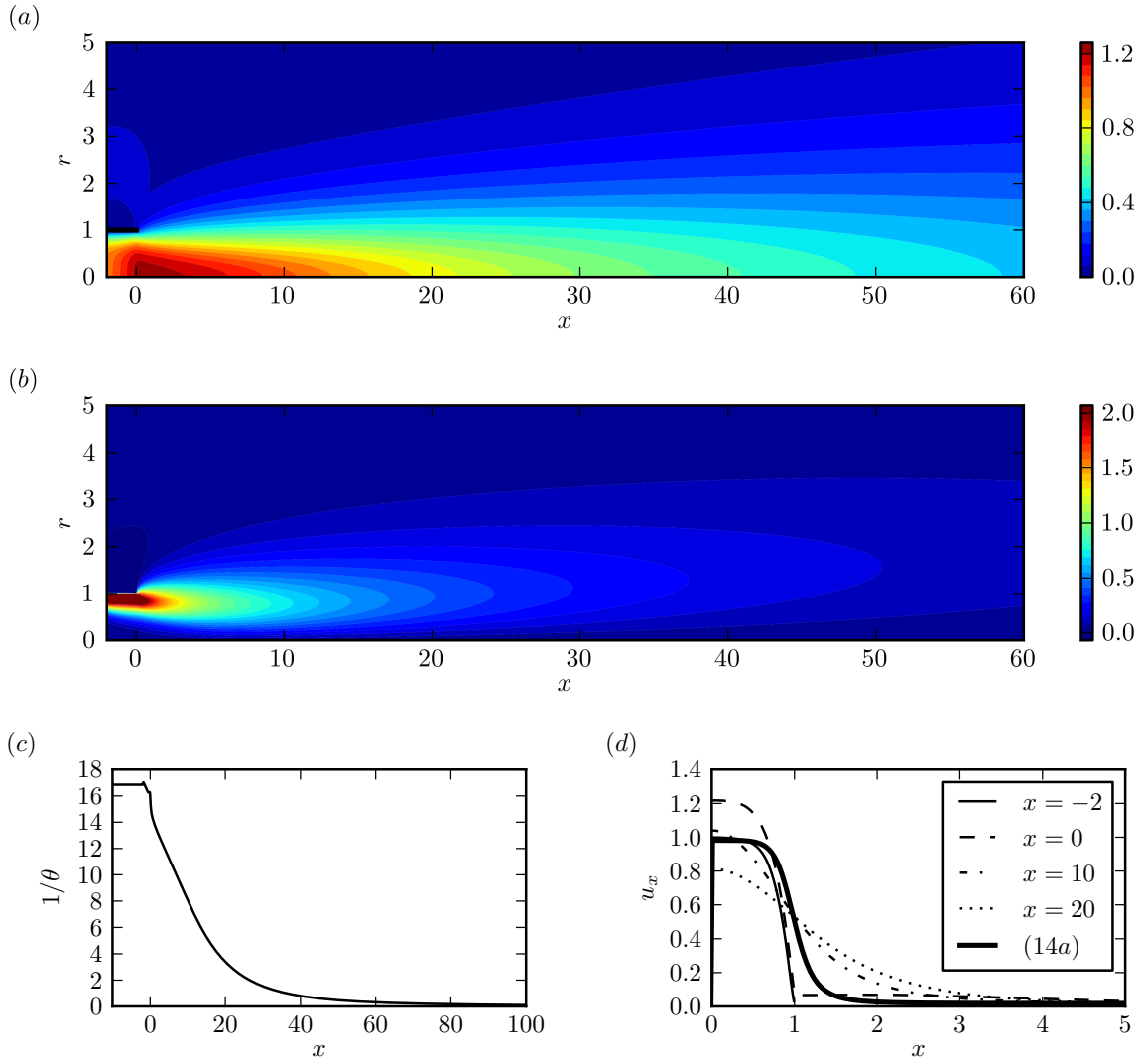

Figure 7: Base flow for the global linear stability study of a spatially developing jet with Re = 100, Ma = 0.75, Pr = 1 and $S = 1$ (unheated). The axial velocity and angular vorticity distributions are respectively displayed in (a) and (b). Only a portion of the computational domain is shown. The evolution of the momentum thickness θ is represented in (c). In (d), axial velocity profiles are at various locations are shown together with the profile used in § 3.2 and 3.3.

Fifteen modes were computed for a large frequency shift $\omega_0 = 5.1$. These are represented in figure 8*b* by red and green symbols. Their dilatation fields, shown in figure 10, characterize these modes as being of acoustic nature. Comparing the real and imaginary parts (not shown) of the dilatation fields in the pipe, it appears that some modes correspond to acoustic waves propagating downstream inside the duct and being scattered at the nozzle exit (green symbols in figure 8*b*). Others correspond to acoustic waves emanating from a location close to the nozzle exit (red symbols in figure 8*b*). These modes propagate upstream in the inlet duct.

One should keep in mind that free-stream vortical modes with near zero decay rates are also present in the spectrum, similar as in the local analysis of § 3.2. Without shifting and relaxing of the propagator, all modes shown in figure 8 would be masked by those least stable modes. In practice, however, the computation of these modes is challenging, as the separation between eigenvalues is very weak (on the order of $1/\left[\mathrm{Re}(x_{max} - x_{min})\right]$). No result could be converged with sufficient accuracy for this family of modes, and they are not shown.

4.2. Convergence

Convergence of the eigenvectors through the iterations of the Krylov-Schur algorithm is usually monitored in terms of a residual associated with the operator the algorithm is applied to, i.e the SR propagator in the present case. Denoting by $\boldsymbol{Q}_{j,p}$ the estimated p^{th} leading eigenvector after the j^{th} restart of the Krylov-Schur algorithm, and by $\lambda_{j,p}$ the corresponding eigenvalue, the residual is estimated

$$e_{j,p} = \frac{\|\exp(\Delta t \mathcal{F})\boldsymbol{Q}_{j,p} - \lambda_{j,p}\boldsymbol{Q}_{j,p}\|}{\|\boldsymbol{Q}_{j,p}\|},$$

and $\boldsymbol{Q}_{j,p}$ is accepted as converged if the estimation is smaller than a user-chosen tolerance ϵ. A typical evolution of the estimation of this residual is displayed in figure 11*a*. Non-monotonous convergence is observed, consistent with the fact that, in the present case for which the operator L is non-Hermitian, the filtered propagator is non-Hermitian as well. For $\omega_0 = 0.45 + 0.05\mathrm{i}$, computations were performed with values $\epsilon = 10^{-3}$ ($\times$ in figure 11*b*), 10^{-4} ($\circ$) and 10^{-5} ($+$). Five modes were requested in each computation. The resulting spectra are shown in figure 11*b*. Significant scattering of the computed eigenvalues is noticed for $\epsilon = 10^{-3}$. The absolute scattering being of the same order of magnitude in the real and imaginary directions, relative errors in the real part of the eigenfrequency are much smaller than in the growth rate. The scattering of eigenvalues becomes less important as requested accuracy increases. With $\epsilon = 10^{-4}$ and $\epsilon = 10^{-5}$ eigenvalues seem to converge to a line trend, and eigenvalues in the overlapping region from the two shift values $\omega_0 = 0.45 + 0.05\mathrm{i}$ and $0.5 + 0.05\mathrm{i}$ are in reasonably good agreement, as shown in figure 11*c*. However, this measure of convergence depends on the spectral transformation used, in particular here on Δt and τ. A more meaningful measure of accuracy may be defined based on the original operator L:

$$e'_{j,p} = \frac{\|L\boldsymbol{q}_{j,p} + \mathrm{i}\omega_{j,p}\boldsymbol{q}_{j,p}\|}{\|\boldsymbol{q}_{j,p}\|} \quad \text{with } \boldsymbol{Q}_{j,p} = (\boldsymbol{q}_{j,p}, \overline{\boldsymbol{q}}_{j,p})^T$$

These residuals are computed after convergence (denoted by $j = \infty$), and are displayed in figure 11*d*. A first observation is that the values differ significantly from the values of the $e_{\infty,p} \approx \epsilon$ discussed earlier, measured with respect to the SR propagator. Furthermore, the values of $e'_{\infty,p}$ decrease only slowly with ϵ; values on the order of 3%, 2% and 1% are found for $\epsilon = 10^{-3}$, 10^{-4} and 10^{-5} respectively. This saturation seems to be due to the spatial filtering which is applied during time-stepping in order to maintain stability. It introduces a slight modification of the propagator which is not taken into account when the Rayleigh quotient (12) is taken.

In order to achieve residuals $e' \leq 2.2\%$, values of ϵ ranging from 10^{-4} to 10^{-7} had to be used for the computations presented in the previous section, depending on the shift ω_0 (larger values of $\omega_{0,r}$ requiring smaller values of ϵ in the present case).

5. Conclusion

A new numerical procedure for the solution of large eigenvalue problems has been presented. A relaxation technique using a first-order temporal bandpass filter is coupled to to the linearized equations of motion, such that the least stable eigenmodes of the filtered system lie in a prescribed frequency band of interest centered around a shift frequency. These modes are then recovered through propagation over a finite time interval, using standard eigenvalue extraction techniques. This "shift-relax" transformation therefore requires no solution of linear systems, which are computationally expensive or even untractable for global stability problems involving two- or three-dimensional flows. Although not as flexible as the classical "shift-invert" transformation or its variants, the present method has the advantage of considerably lower memory requirement, making it suitable for the analysis of complex two- or three-dimensional flow geometries. Another advantage lies in the ease of implementation: only a simple filter equation needs to be added to an existing simulation code in order to perform eigenmode extraction. No matrix needs to be built, and no preconditioning is required. Finally, the algorithm can be parallelized as efficiently as a regular time stepper, as the filter is local in space.

Acknowledgments

This work was supported by DGA grant number 2009.60.034.00.470.75.01. The authors are thankful to Miguel Fosas and Patrick Huerre for their comments.

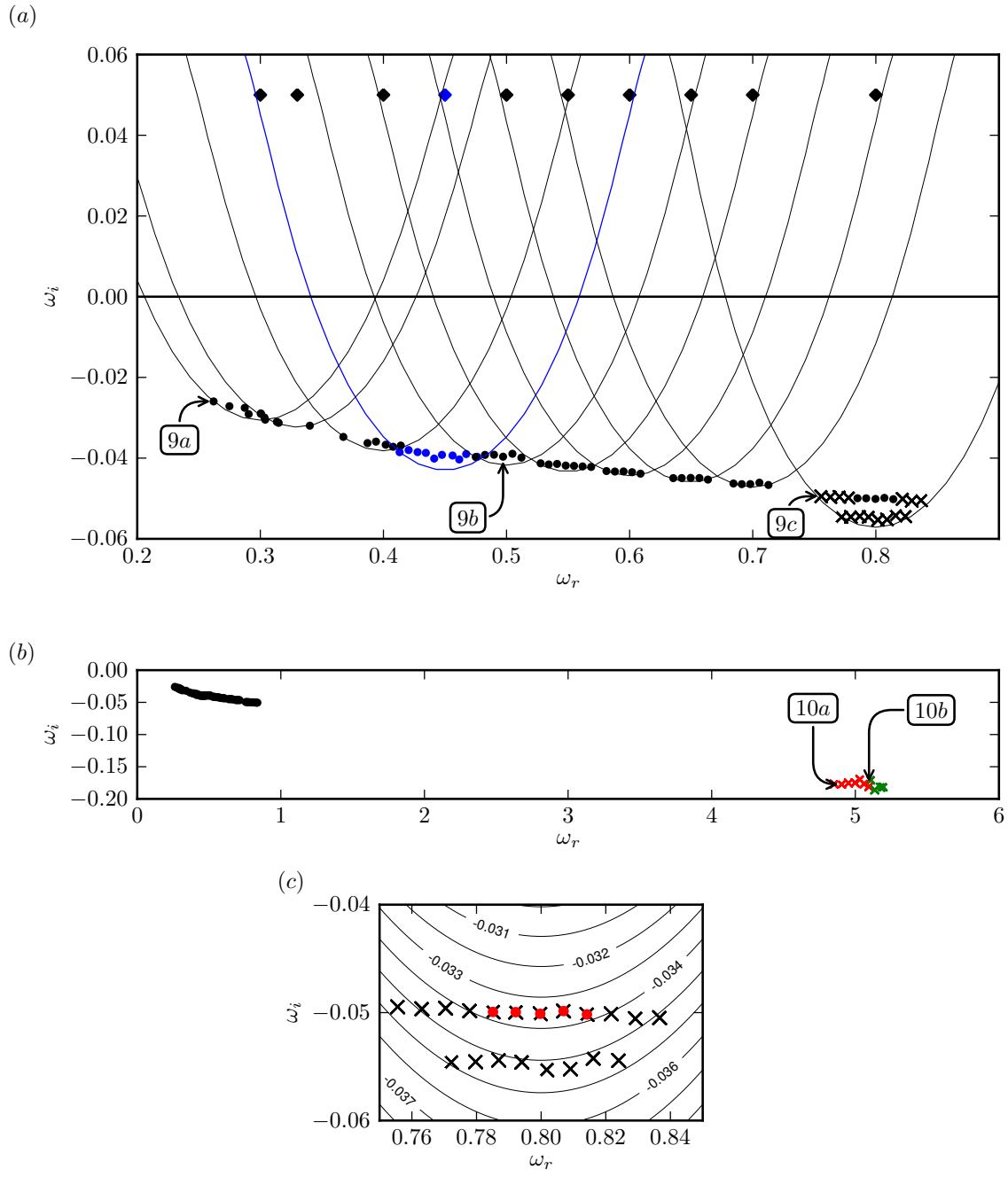

Figure 8: Eigenvalues of axisymmetric modes in an isothermal jet at Re = 100, Ma = 0.75 and Pr = 1 computed using the SR method. Tolerance was set to $\epsilon = 10^{-4}$ for $\omega_{0,r} \leq 0.5$, $\epsilon = 10^{-5}$ for $0.5 < \omega_{0,r} \leq 0.8$ and $\epsilon = 10^{-7}$ for $\omega_{0,r} = 5.1$. (*a*) Low frequency shear layer modes. Shift positions are indicated by diamonds. For each shift, an isocontour of the filtered propagator growth rate is represented; its value corresponds to the least amplified mode computed by the Krylov-Schur solver. For $\omega_0 = 0.45 + 0.05\mathrm{i}$, the shift, the modes and the isocontour are represented in blue. (*b*) Low frequency vortical modes are shown together with higher frequency acoustic modes. (*c*) Close-up on the 15 modes computed for $\omega_0 = 0.8 + 0.05\mathrm{i}$, showing the existence of two branches: dots correspond to the first five modes computed, crosses correspond to the next ten. Labels correspond to the modes for which the vorticity or dilatation field is displayed in figure 9 and 10.

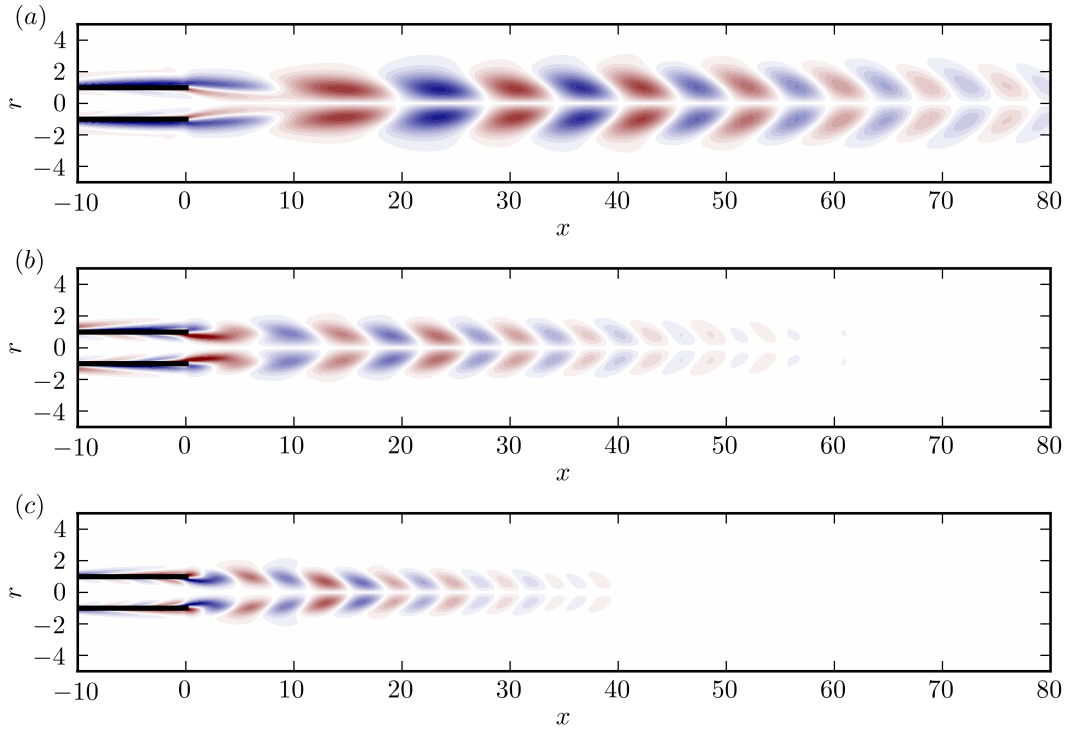

Figure 9: Real part of the vorticity fields of typical eigenmodes, labeled in figure 8*a*, in an isothermal jet at Re = 100, Ma = 0.75 and Pr = 1. (*a*) $\omega = 0.26 - 0.026\mathrm{i}$. (*b*) $\omega = 0.50 - 0.040\mathrm{i}$. (*c*) $\omega = 0.71 - 0.047\mathrm{i}$.

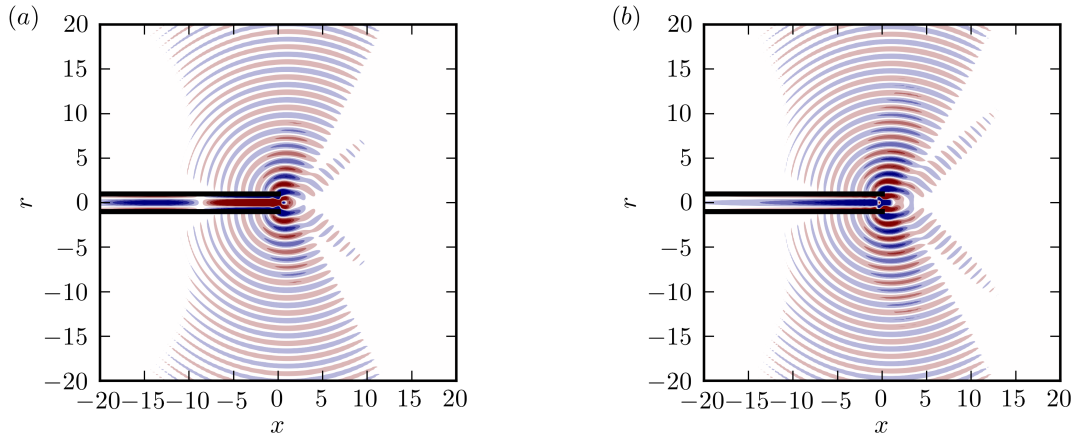

Figure 10: Real part of the dilatation fields of typical eigenmodes, labeled in figure 8*a*, in an isothermal jet at Re = 100, Ma = 0.75 and Pr = 1. (*a*) $\omega = 4.9 - 0.17\mathrm{i}$. (*b*) $\omega = 5.1 - 0.18\mathrm{i}$.

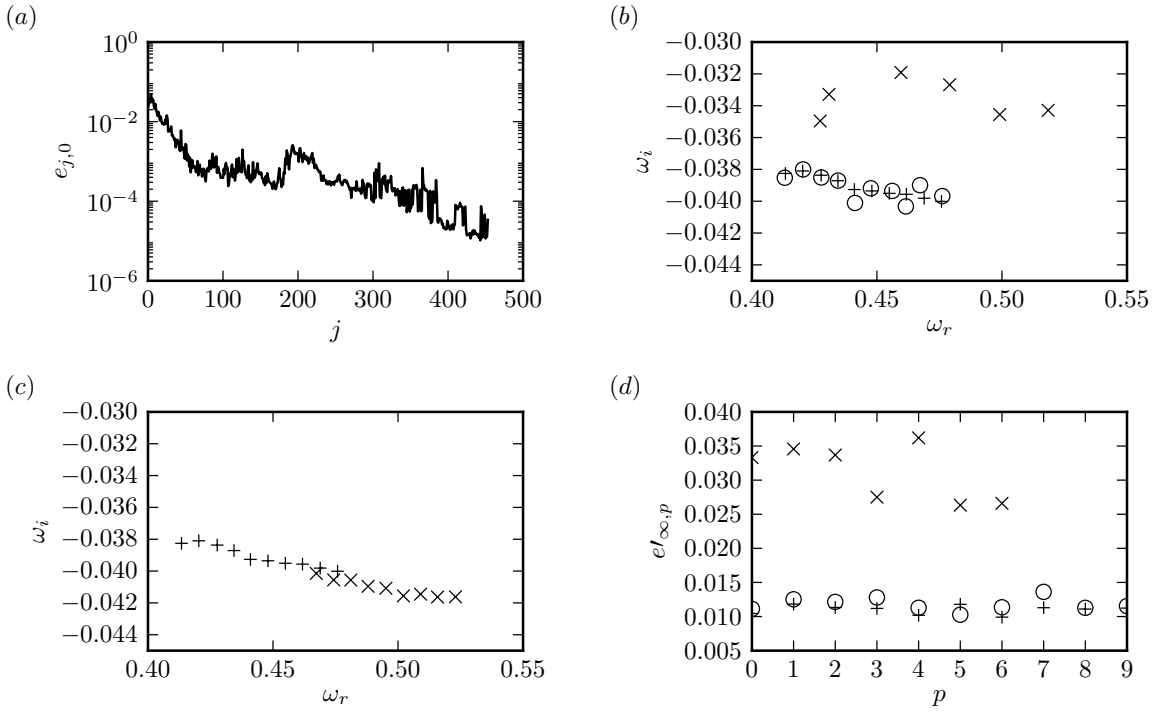

Figure 11: Convergence features. (*a*) A typical evolution of the estimated residual of the leading eigenvalue with the number of restarts. (*b*) Spectra computed with $\omega_0 = 0.45 + 0.05\mathrm{i}$ and $\epsilon = 10^{-3}$, 10^{-4} and 10^{-5} (respectively represented by $\times$, $\circ$ and $+$ symbols). 5 modes were requested. (*c*) Spectra computed for $\epsilon = 10^{-5}$ with $\omega_0 = 0.45 + 0.05\mathrm{i}$ and $0.5 + 0.05\mathrm{i}$ are shown. (*d*) Residual based for the computations of (*b*).

Appendix A. Distinction between the two transformed eigenvalues

The eigenvalue transformation is given in terms of the scaled variables by (10). Let us introduce

$$\widetilde{\Omega} = \frac{\Omega' + \mathrm{i}}{\sqrt{\chi'}}, \qquad \widetilde{\omega} = \frac{\omega' + \mathrm{i}(1-\chi')}{\sqrt{\chi'}}.$$

Equation (10) then reads

$$\widetilde{\Omega}^2 - \widetilde{\omega}\widetilde{\Omega} + 1 = 0. \tag{A.1}$$

The solutions of this second-order polynomial are given by

$$\widetilde{\Omega} = \frac{1}{2}\left(\widetilde{\omega} \pm \sqrt{\widetilde{\omega}^2 - 4}\right).$$

Let $\alpha = \sqrt{\widetilde{\omega}^2 - 4}$. One of these roots has a positive imaginary part and the other one a negative one if $|\widetilde{\omega}_i| \leq |\alpha_i|$. In order to prove that this condition holds, real and imaginary parts are introduced in the definition of α:

$$(\alpha_r^2 - \alpha_i^2) + 2\alpha_r\alpha_i\mathrm{i} = (\widetilde{\omega}_r^2 - \widetilde{\omega}_i^2) - 4 + 2\widetilde{\omega}_r\widetilde{\omega}_i\mathrm{i}$$

so

$$\widetilde{\omega}_r\widetilde{\omega}_i = \alpha_r\alpha_i \qquad \alpha_r^2 - \alpha_i^2 = \widetilde{\omega}_r^2 - \widetilde{\omega}_i^2 - 4.$$

The variable α_i can then be written as

$$\alpha_i^2 = \widetilde{\omega}_i^2 + 4 - (\widetilde{\omega}_r^2 - \alpha_r^2) = \widetilde{\omega}_i^2 + 4 - \left(\frac{\alpha_i^2}{\widetilde{\omega}_i^2} - 1\right)\alpha_r^2$$

which finally gives

$$\alpha_i^2 = \frac{\widetilde{\omega}_i^2 + 4 + \alpha_r^2}{1 + \dfrac{\alpha_r^2}{\widetilde{\omega}_i^2}} = \widetilde{\omega}_i^2\frac{\widetilde{\omega}_i^2 + 4 + \alpha_r^2}{\widetilde{\omega}_i^2 + \alpha_r^2} \geq \widetilde{\omega}_i^2.$$

Let $\widetilde{\Omega}^+$ denote the root of (A.1) with a positive imaginary part and $\widetilde{\Omega}^-$ the one with the negative imaginary part. In terms of the primed variables, this corresponds to

$$\Omega'^-_i \leq -1 \leq \Omega'^+_i.$$

References

[1] E. Akervik, L. Brandt, D.S. Henningson, J. Hoepffner, O. Marxen, and P. Schlatter. Steady solutions of the Navier-Stokes equations by selective frequency damping. *Phys. Fluids*, 18(6):068102, 2006.

[2] E. Akervik, U. Ehrenstein, F. Gallaire, and D.S. Henningson. Global two-dimensional stability measures of the flat plate boundary-layer flow. *Eur. J. Mech. B-Fluid*, 27(5):501–513, 2008.

[3] P.R. Amestoy, I.S. Duff, and J.Y. L'Excellent. Multifrontal parallel distributed symmetric and unsymmetric solvers. *Comput. Method. Appl. M.*, 184(2-4):501–520, 2000.

[4] S. Balay, K. Buschelman, V. Eijkhout, W.D. Gropp, D. Kaushik, M.G. Knepley, L. Curfman McInnes, B.F. Smith, and H. Zhang. PETSc users manual. Technical Report ANL-95/11 - Revision 3.0.0, Argonne National Laboratory, 2008. Available at http://www.mcs.anl.gov/petsc/petsc-as/.

[5] A. Barbagallo, D. Sipp, and P.J. Schmid. Closed-loop control of an open cavity flow using reduced-order models. *J. Fluid Mech.*, 641:1–50, 2009.

[6] J. Berland, C. Bogey, O. Marsden, and C. Bailly. High-order, low dispersive and low dissipative explicit schemes for multiple-scale and boundary problems. *J. Comput. Phys.*, 224(2):637–662, 2007.

[7] C. Bogey and C. Bailly. Three-dimensional non-reflective boundary conditions for acoustic simulations: far field formulation and validation test cases. *Acta Acust.*, 88:463–471, 2002.

[8] T. Colonius. Modeling artificial boundary conditions for compressible flow. *Annu. Rev. Fluid Mech.*, 36(1):315–345, 2004.

[9] T.A. Davis. UMFPACK version 5.5.0 user guide. Technical report, 2009. Available at http://www.cise.ufl.edu/research/sparse/umfpack/.

[10] W.S. Edwards, L.S. Tuckerman, R.A. Friesner, and D.C. Sorensen. Krylov methods for the incompressible Navier-Stokes equations. *J. Comput. Phys.*, 110(1):82–102, 1994.

[11] G.H. Golub and C.F. Van Loan. *Matrix computations, third edition.* The John Hopkins University Press, 1996.

[12] V. Hernandez, J.E. Roman, A. Tomas, and V. Vidal. A survey of software for sparse eigenvalue problems. Technical Report STR-6, Universidad Politcnica de Valencia, 2006. Available at http://www.grycap.upv.es/slepc.

[13] P. Huerre and P.A. Monkewitz. Local and global instabilities in spatially developing flows. *Annu. Rev. Fluid Mech.*, 22:473–537, 1990.

[14] D. A. Knoll and D. E. Keyes. Jacobian-free Newton-Krylov methods: a survey of approaches and applications. *J. Comput. Phys.*, 193(2):357–397, January 2004.

[15] R.B. Lehoucq and A.G. Salinger. Large-Scale eigenvalue calculations for stability analysis of steady flows on massively parallel computers. *Inter. J. Numer. Meth. Fl.*, 36:309–327, 1999.

[16] R.B. Lehoucq, D.C. Sorensen, and C. Yang. *ARPACK Users' Guide: Solution of Large-Scale Eigenvalue Problems with Implicitly Restarted Arnoldi Methods.* SIAM, 1998.

[17] S.K. Lele. Compact finite difference schemes with spectral-like resolution. *J. Comput. Phys.*, 103(1):16–42, 1992.

[18] C.J. Mack and P.J. Schmid. A preconditioned krylov technique for global hydrodynamic stability analysis of large-scale compressible flows. *J. Comput. Phys.*, 229(3):541–560, 2010.

[19] C.J. Mack, P.J. Schmid, and J.L. Sesterhenn. Global stability of swept flow around a parabolic body: connecting attachment-line and crossflow modes. *J. Fluid Mech.*, 611:205–214, 2008.

[20] J.W. Nichols and S.K. Lele. Global modes and transient response of a cold supersonic jet. *J. Fluid Mech.*, 669:225–241, January 2011.

[21] T.J. Poinsot and S.K. Lele. Boundary conditions for direct simulations of compressible viscous flows. *J. Comput. Phys.*, 101(1):104–129, 1992.

[22] J.E. Roman, M. Kammerer, F. Merz, and F. Jenko. Fast eigenvalue calculations in a massively parallel plasma turbulence code. *Parallel Comput.*, 36(5-6):339–358, 2010. Parallel Matrix Algorithms and Applications.

[23] J.E. Roman, E. Romero, and A. Tomas. SLEPc users manual. Technical Report DSIC-II/24/02, Universidad Politecnica de Valencia, 2010. Available at http://www.grycap.upv.es/slepc.

[24] Y. Saad. *Iterative methods for sparse linear systems, second edition.* SIAM, 2003.

[25] R.D. Sandberg. Governing equations for a new compressible Navier-Stokes solver in general cylindrical coordinates. Technical Report AFM-07/07, University of Southampton, 2007. Available at http://eprints.soton.ac.uk/49523/.

[26] P.J. Schmid and D.S. Henningson. *Stability and Transition in Shear Flows*. Springer, 2001.

Chapter 4

Base flows

The aim of this study is to describe the development of coherent structures, such as those shown in figure 4.1, commonly observed over about ten jet radii downstream of the jet pipe. The present chapter presents the different "base states" that have been used. Steady solutions of the Navier-Stokes equations (§ 4.1) describe laminar flows that develop very slowly. Such solutions, although stable, are not observed: incoming perturbations are amplified, resulting in turbulent jets in most situations. Contrary to steady states, turbulent mean flows (§ 4.2) are strongly non-parallel. As no mean flows were available at the time when most of the studies were performed, a model flow developed by Monkewitz and Sohn (1988) was adapted to fit the present flow configuration (§ 4.3).

4.1 Steady jet flows

The Navier–Stokes equations are symbolically written as

$$\mathcal{B}\frac{\partial \boldsymbol{q}}{\partial t} = \mathcal{N}(\boldsymbol{q},\boldsymbol{q}) + \mathcal{L}\boldsymbol{q} = N(\boldsymbol{q}) \tag{4.1}$$

where $\mathcal{N}$ is bilinear and $\mathcal{B}$ and $\mathcal{L}$ are linear[1]. Let $\boldsymbol{q}_0$ be a steady state, such that $N(\boldsymbol{q}_0) = 0$. The dynamics of infinitesimal perturbations $\boldsymbol{q}'$ about this state are therefore governed by

$$\mathcal{B}\frac{\partial \boldsymbol{q}'(t)}{\partial t} = \boldsymbol{\nabla} N_{\boldsymbol{q}_0}\boldsymbol{q}'(t) \equiv L\boldsymbol{q}'(t) \tag{4.2}$$

which provides a convenient framework for the analysis. This approach has been followed in many previous stability analyses, e.g. by Barbagallo et al.

[1] In the compressible case $\mathcal{B} = \mathrm{Id}$. For the incompressible case $\mathcal{B}$ is used to impose mass conservation.

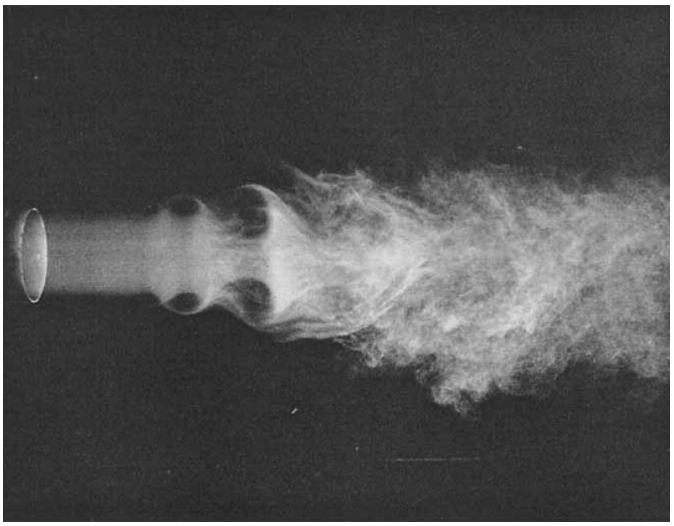

Figure 4.1: Smoke visualization of a jet at $Re = 10^4$. Image taken from Crow and Champagne (1971).

(2009) for the flow over an open cavity, by Meliga et al. (2009) and Meliga et al. (2010) for wakes, by Barkley et al. (2002) for the flow over a backward-facing step and by Akervik et al. (2008) for boundary layer flow.

Instead of computing a steady solution of the Navier–Stokes equations Nichols and Lele (2011b) used a boundary layer approximation of the base flow for their linear analysis of perturbations in free jets. As jet flows are stable, steady solutions of the Navier–Stokes equations can easily be computed by advancing in time an initial guess or, if a linear solver is available, using Newton's method. Compared to a boundary layer approximation, this is computationally more expensive but allows us to take into account both the jet pipe and the free-jet region. A typical steady solution for a jet flow is shown in figure 4.2. As the inflow profile imposed at $x = -5$ is not a Poiseuille flow, a slow viscous spreading is observed inside the jet pipe, and the centerline velocity increases by 10% throughout the pipe. In spite of the sudden change in geometry at $x = 0$, non-parallelism is weak for $x > 0$ since viscous effects are weak. A Reynolds number of ~ 100 would be necessary to have a significant spreading for $0 \leq x \leq 10$. Very similar results have been found for the compressible regime.

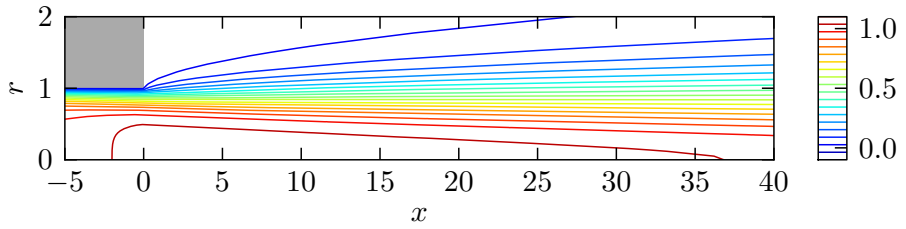

Figure 4.2: Axial velocity distribution of the steady solution of the incompressible Navier–Stokes equations at $Re = 10^3$ with an inflow profile $u_x(0, r) = \tanh(5(1 - r))$.

4.2 Mean turbulent flows

Figure 4.3 displays the axial velocity distribution of a turbulent mean flow obtained by Direct Numerical Simulation by Sandberg et al. (2012) for a jet Mach number of 0.46 and a co-flow Mach number of 0.2. Contrary to the steady flow, the flow development is very rapid downstream of the pipe. In the potential core, which extends over approximately $0 \leq x \leq 8$, the shear layer thickness increases quasi-linearly with x. This type of base flow therefore seems more suitable than steady laminar flows for the description of coherent structures, such as those of figure 4.1. However, a mean flow $\boldsymbol{q}_1$ does not satisfy $N(\boldsymbol{q}_1) = 0$, so the dynamics of perturbations about $\boldsymbol{q}_1$ is no longer given by (4.2). Following Reynolds and Hussain (1972), we decompose the flow field according to $\boldsymbol{q} = \bar{\boldsymbol{q}} + \widetilde{\boldsymbol{q}} + \boldsymbol{q}'$ where $\bar{\boldsymbol{q}}$ corresponds to the mean flow, $\widetilde{\boldsymbol{q}}$ to the coherent structures and $\boldsymbol{q}'$ to the turbulent scales. Let τ_c be the characteristic time associated with coherent structures and τ_t the time associated with turbulent scales. The average over long times $\tau_l \gg \tau_c$ is denoted by $\overline{\cdot}$. Characteristic times are assumed to be such that there is an intermediate time τ_s such that $\tau_c \gg \tau_s \gg \tau_t$, and the average over this time scale is denoted by $\langle\cdot\rangle$. Taking the long-time average of (4.1) yields the equation for the base state:

$$\mathcal{N}(\bar{\boldsymbol{q}}, \bar{\boldsymbol{q}}) + \overline{\mathcal{N}(\widetilde{\boldsymbol{q}}, \widetilde{\boldsymbol{q}})} + \overline{\mathcal{N}(\boldsymbol{q}', \boldsymbol{q}')} + \mathcal{L}\bar{\boldsymbol{q}} = 0. \tag{4.3}$$

The short time average gives

$$\mathcal{B}\frac{\partial \widetilde{\boldsymbol{q}}}{\partial t} - \mathcal{N}(\bar{\boldsymbol{q}}, \widetilde{\boldsymbol{q}}) - \mathcal{N}(\widetilde{\boldsymbol{q}}, \bar{\boldsymbol{q}}) - \mathcal{L}\widetilde{\boldsymbol{q}} = \mathcal{N}(\widetilde{\boldsymbol{q}}, \widetilde{\boldsymbol{q}}) - \overline{\mathcal{N}(\widetilde{\boldsymbol{q}}, \widetilde{\boldsymbol{q}})} + \langle \mathcal{N}(\boldsymbol{q}', \boldsymbol{q}') \rangle - \overline{\mathcal{N}(\boldsymbol{q}', \boldsymbol{q}')}. \tag{4.4}$$

Equation (4.4) gives the dynamics of the coherent structures. Terms on the left-hand side correspond to the LNS equations, similar to the case of pertur-

bations about a steady state. The first two terms on the right-hand side are quadratic in $\widetilde{\boldsymbol{q}}$ and can be omitted in a linear analysis. The last two terms correspond to the influence of turbulent scales on instability waves and can contribute to the linear dynamics. They cannot be explicitly computed and need to be evaluated through a closure model (see Reynolds and Hussain (1972) for possible models). The simplest approach, followed here and referred to as the "quasi-laminar model" in Reynolds and Hussain (1972), is to simply neglect this term. This approximation proved to be sufficient for jet flows in previous linear stability studies (Crighton and Gaster 1976, Plaschko 1979, Michalke 1984). Rodriguez et al. (2011) report that when performing a stability study of a turbulent jet using the Parabolized Stability Equations, modeling turbulent scales through an eddy viscosity did not alter significantly the results. For boundary layer flows, on the contrary, modeling the influence of turbulent scales on coherent structures is required in order to capture the instability features. In a parallel-flow framework, eddy viscosity models have been used, see Kitsios et al. (2010), Pujals et al. (2009). In a non-parallel framework, Crouch et al. (2007) used a uRANS model to study the stability of the flow around an airfoil.

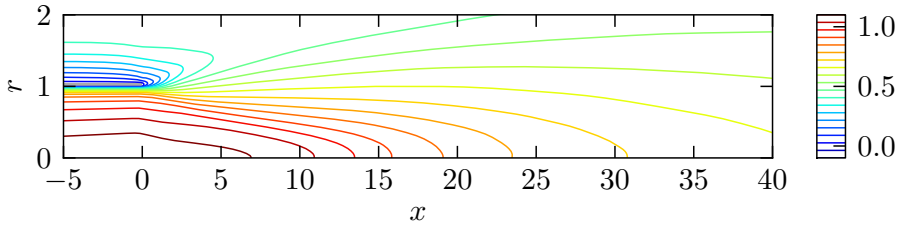

Figure 4.3: Axial velocity distribution of the turbulent mean flow for a $Ma = 0.46$ jet exiting into a $Ma = 0.2$ co-flow at $Re = 7500$. (Data given by Sandberg et al. (2012)).

4.3 Model jet flow

Neither boundary layer approximations nor steady-state solutions of the Navier–Stokes equations can reflect the rapid streamwise development observed in turbulent jets. For the purpose of this study, a parametric model of a turbulent jet is adapted from Sohn (1986) (see also Monkewitz and Sohn (1988)) and schematically presented in figure 4.4. The model is designed to match experimentally measured mean flows in the subsonic regime. As the original manuscript is not widely available, the free-jet model is reviewed in

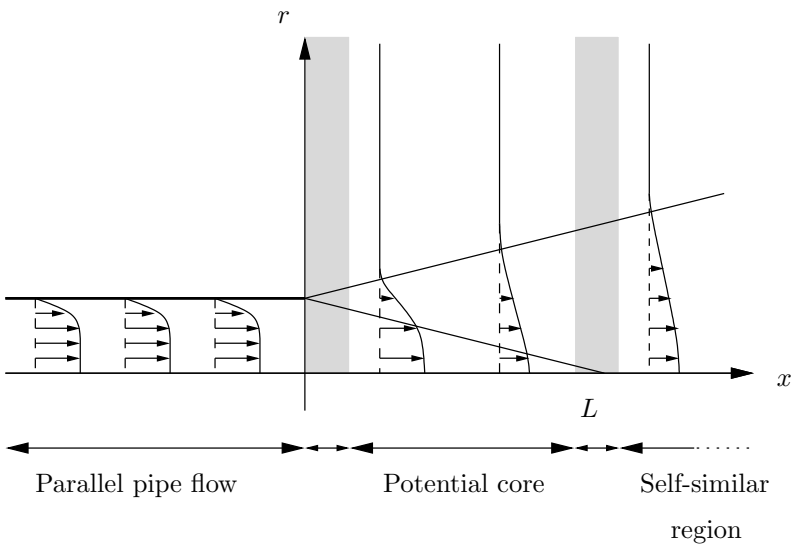

Figure 4.4: Model base flow. The parallel pipe flow region, the potential core and the self similar region are connected by smooth transitions, indicated by shaded areas.

§ 4.3.1. Downstream of the nozzle, experimental studies indicate that the potential core typically extends over eight jet radii, and that in this region the shear layer initially spreads linearly with x while the velocity on the axis remains approximately constant. Further downstream, velocity profiles are approximated as a Gaussian, and continue to spread radially. The flow inside the inlet duct is considered to be parallel (§ 4.3.2). A smooth transition between the pipe flow and the free jet is realized in a small matching region downstream of the nozzle (§ 4.3.3).

4.3.1 Free jet

The parametric model of a turbulent mean jet flow developed by Sohn (1986) is used in this study. A family of profiles is described, characterized by the density ratio at the inlet

$$S_0 = \frac{\rho(0,0)}{\rho_\infty}$$

and the Mach number. A third parameter ϵ_0, characterizing the shear layer thickness at the outlet, is introduced in the present study.

Explicit analytical formulas are given for the length of the potential core and the evolution of the jet axial velocity u_x on the centerline. The shape of the axial velocity profile is also given, up to a radial scale $\delta(x)$ that remains

to be determined. At each axial position, the relationship between density and axial velocity profiles is also given as a function of the density on the jet axis $S(x)$. δ and S are chosen such that momentum and energy flux are conserved throughout the jet.

Potential core The length of the potential core is prescribed as

$$L = 8 + 2.5\log(S_0). \tag{4.5}$$

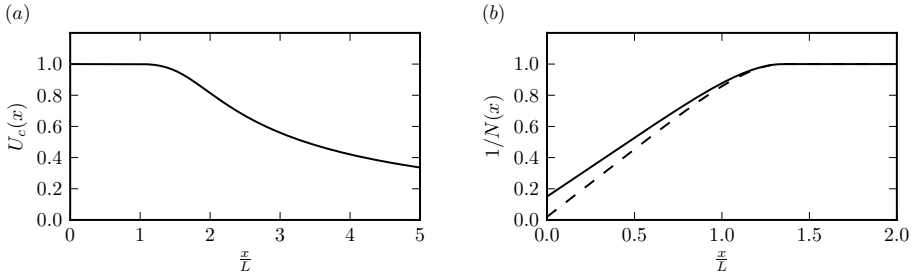

Figure 4.5: (a): Distribution of axial velocity $U_c(x)$ given by (4.7). (b) Distribution of the shear layer thickness parameter $N(x)$ given by (4.8) (dashed line) and by (4.11) with $\epsilon_0 = 0.15$ (solid line).

Axial velocity profile Axial velocity profiles are assumed to be of the form

$$u_x(r,x) = U_c(x)F\left(\frac{r}{\delta(x)}, x\right)$$

with

$$F(\eta,x) = \left\{1 + \left[\exp\left(\eta^2\log(2)\right) - 1\right]^{N(x)}\right\}^{-1}. \tag{4.6}$$

The quantity $U_c(x)$ denotes the velocity on the jet center-line: in order to fit experimental measurements it is assumed to be given by

$$U_c(x) = \begin{cases} 1. & \frac{x}{L} \leq 1. \\ 1.682\left[\left(\frac{x}{L}\right)^7 + 37.1\left(\frac{x}{L}\right)^{-0.189}\right]^{-1/7} & \frac{x}{L} > 1. \end{cases} \tag{4.7}$$

The parameter $N(x)$ governs the smoothness of the profile: $N \to \infty$ corresponds to a cylindrical vortex sheet, while $N = 1$ corresponds to a Gaussian velocity distribution. The streamwise variation of N is given by

$$N(x) = \begin{cases} \left[0.02 + 0.869\left(\frac{x}{L}\right) - 0.031\left(\frac{x}{L}\right)^{6.072}\right]^{-1} & \frac{x}{L} \leq 1.35. \\ 1. & \frac{x}{L} > 1.35. \end{cases} \tag{4.8}$$

and U_c and N are represented as functions of x in figure 4.5.

Pressure field Pressure is assumed to be constant, and given as

$$p = \frac{1}{\gamma Ma^2}.$$

Density / temperature distribution The relation between temperature and velocity is taken from Schlichting (1955):

$$\frac{1/\rho(r,x)-1}{1/S(x)-1} = \left(\frac{u_x(r,x)}{U_c(x)}\right)^{\sigma(x)} = F\left(\frac{r}{\delta(x)},x\right)^{\sigma(x)}, \tag{4.9}$$

where the distribution of σ is given by

$$\sigma(x) = \begin{cases} 1. & \frac{x}{L} \leq 0.64, \\ 0.8 + 0.2\cos\left(2.49\frac{x}{L} - 1.60\right) & 0.64 < \frac{x}{L} \leq 1.90, \\ 0.6 & \frac{x}{L} > 1.90, \end{cases} \tag{4.10}$$

to match experiments.

Momentum and energy conservation The streamwise development of δ and S is not prescribed: these quantities are computed so that momentum and energy fluxes through sections perpendicular to the jet axis are constant:

$$\int_0^\infty \rho u_x^2 r \,\mathrm{d}r = \mathcal{M}$$

and

$$\int_0^\infty \rho u_x \left[\frac{T-1}{(\gamma-1)Ma^2} + \frac{1}{2}u_x^2\right] r \,\mathrm{d}r = \mathcal{E}.$$

These expressions can be rewritten as

$$\mathcal{M} = \delta(x)^2 U_c(x)^2 \int_0^\infty \frac{F(\eta,x)^2}{1+(1/S(x)-1)F(\eta,x)^{\sigma(x)}}\eta \,\mathrm{d}\eta$$

and

$$\mathcal{E} = \delta(x)^2 \int_0^\infty \frac{1}{2}\frac{U_c(x)^3 F(\eta,x)^3}{1+(1/S(x)-1)F(\eta,x)^{\sigma(x)}} + \frac{(1/S(x)-1)}{(\gamma-1)Ma^2}\frac{U_c(x)F(\eta,x)^{1+\sigma(x)}}{1+(1/S(x)-1)F(\eta,x)^{\sigma(x)}}\eta \,\mathrm{d}\eta.$$

The invariants $\mathcal{M}$ and $\mathcal{E}$ are determined by their values at $x = 0$, where $\delta(0) = 1$ and $S(0) = S_0$. The ratio $\mathcal{M}/\mathcal{E}$ is only a function of $S(x)$ and is solved numerically. This value is then used to obtain $\delta(x)$ by invoking momentum and energy conservation.

Thickness of the shear layer The thickness of the shear layer is estimated through the momentum thickness

$$\Theta(x) = \int_0^\infty \frac{\rho(r,x)u_x(r,x)}{\rho(0,x)u_x(0,x)} \left(1 - \frac{u_x(r,x)}{u_x(0,x)}\right) r \, \mathrm{d}r.$$

which is related to the distribution of $N(x)$. The variations of N in the potential core are such that:

- the shear layer thickness is of the order of 0.02 at the nozzle,
- the shear layer spreading is approximately linear in the potential core,
- the shear layer matches a Gaussian distribution at $x = 1.35L$: N and its first derivative are continuous.

From a numerical point of view, the treatment of such a shear layer would be expensive. The only modification to the free jet model of Sohn reviewed above is to prescribe N in the form

$$N(x) = \left[\epsilon_0 + ax + bx^6\right]^{-1}, \quad x \leq 1.35L. \tag{4.11}$$

The parameter ϵ_0 is chosen as $\epsilon_0 = 0.15$, which gives $\Theta = 0.054$ at $x = 0$ (this value is modified by the presence of the pipe flow as explained in § 4.3.2). The coefficients a and b are determined in order to ensure continuity of N and N' at $x = 1.35L$. The new distribution of N is illustrated in figure 4.5 together with the one given by (4.8); they have similar behavior except for the value at $x = 0$.

4.3.2 Pipe flow

Parallel pipe flow The axial velocity profile in the pipe is assumed to be of the form

$$u_x(r,x) = \begin{cases} 2\left(1 + \left[\exp\left(r^2 \log(2)\right) - 1\right]^{N_1}\right)^{-1} - 1 & r \leq 1. \\ 0 & r > 1. \end{cases} \tag{4.12}$$

The parameter N_1 characterizes the maximum slope of the velocity profile. It should be of the order of ϵ_0^{-1} such that it continuously matches (4.12) with the jet flow velocity distribution given by (4.6). An adiabatic pipe is considered, and thus uniform temperature, density and pressure distributions are assumed inside and outside the pipe. The density is respectively equal to S_0 for $r \leq 1$ and 1 for $r > 1$. This pipe flow profile defines the momentum and energy fluxes $\mathcal{M}$ and $\mathcal{E}$ to be conserved throughout the jet. The resulting distributions of δ and S are shown in figure 4.6.

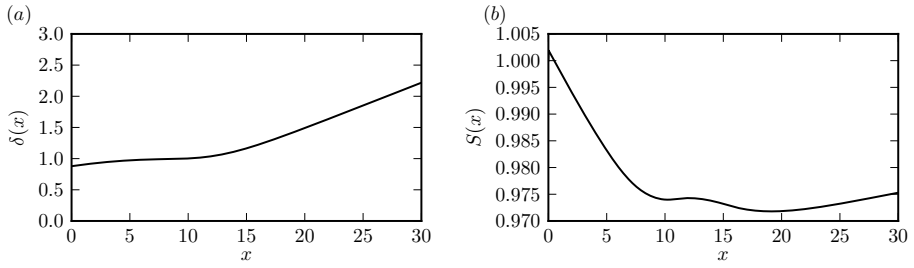

Figure 4.6: Application of momentum and energy conservation for $\epsilon_0 = 0.15$, Ma $= 0.75$ and $S_0 = 1$. A value $N_1 = 0.6/\epsilon_0$ has been chosen to ensure smoothness of the momentum thickness. (a): jet radial scale. (b): local density ratio.

4.3.3 Matching

Matching of pipe and jet flow Let ϕ denote any of the flow field variables, ρ, u_x or T. If $\phi^j(r,x)$ denotes the quamtity in the jet (given in §4.3.1) and $\phi^p(r)$ the same field in the pipe (given in §4.3.2), a continuous matching between each field is achieved as follows. Given a transition length x_t, ϕ_b is uniformly defined in the entire domain as

$$\phi_b(r,x) = \begin{cases} \phi^p(r) & x \leq 0, \\ \left[(1-\psi\left(\frac{x}{x_t}\right)\right]\phi^p(r) + \psi\left(\frac{x}{x_t}\right)\phi^j(r,x) & 0 < x \leq x_t, \\ \phi^j(r,x) & x_t < x, \end{cases} \tag{4.13}$$

where ψ is a smooth function with $\psi(0) = 0$ and $\psi(1) = 1$. The values of x_t and N_1 are chosen such that the evolution of the momentum thickness is continuous. The resulting axial velocity field is presented in figure 4.7.

Radial velocity: mass conservation Only momentum and energy fluxes across sections perpendicular to the jet axis are conserved. Mass conservation is imposed locally, in order to obtain a radial velocity field $u_{0,r}$ from the previously computed axial velocity and density fields using local mass conservation:

$$\frac{\partial \rho_b u_{0,x}}{\partial x} + \frac{\partial \rho_b u_{0,r}}{\partial r} + \frac{\rho_b u_{b,r}}{r} = 0.$$

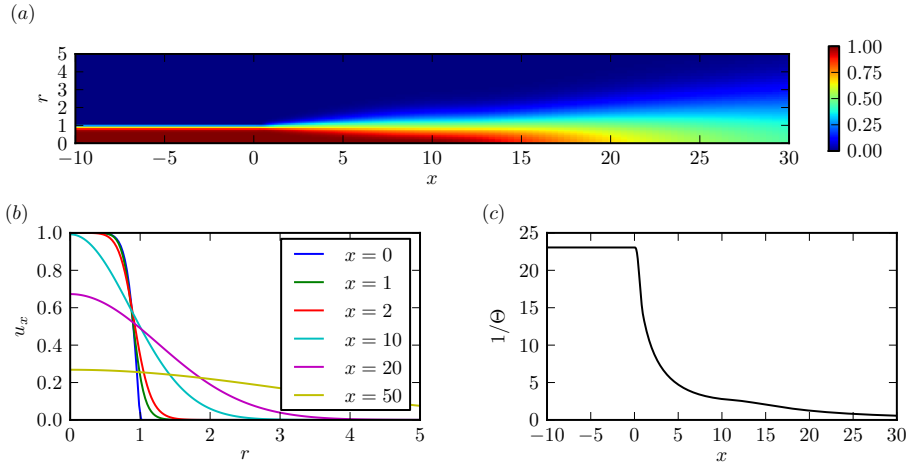

Figure 4.7: Base flow for $\epsilon_0 = 0.15$, Ma $= 0.75$ and $S_0 = 1$ and $x_t = 1.$. A value $N_1 = 0.6/\epsilon_0$ has been chosen to ensure smoothness of the momentum thickness. (a): isocontours of axial velocity. (b): axial velocity profiles at various x locations. (c): momentum thickness.

Chapter 5

Modal analysis of the jet dynamics

5.1 Introduction

5.1.1 Spatial and temporal instability

Classically, flow stability has been studied under the assumption of parallel base flows $\boldsymbol{q}_0$ (Schmid 2007). For non parallel base flows, slices at different locations x_0 are considered, and the stability of the base flow profile $\widetilde{\boldsymbol{q}_0}(x,r) = \boldsymbol{q}(x_0,r)$ is considered. This type of analysis is valid when the typical scale of variation of the base flow L is much larger than the wave length of the perturbations λ. In these approaches as the domain is infinite pertubations are assumed to be of the form

$$\boldsymbol{q}(x,r;t) = \widetilde{\boldsymbol{q}}(r)\exp\left[\mathrm{i}(kx-\omega t)\right] \tag{5.1}$$

Using this decomposition, the LNS equations read

$$-\mathrm{i}\omega M_\omega \boldsymbol{q} + \mathrm{i}kM_k\boldsymbol{q} - k^2 M_{k^2}\boldsymbol{q} + L\boldsymbol{q} = 0 \tag{5.2}$$

where M_ω, M_k, M_{k^2} and L are linear operators. Two types of modal stability analysis can be carried out in this framework:

- in the temporal approach, the wave length λ of the perturbation is given, so the wave number $k = 2\pi/\lambda \in \mathbb{R}$ is imposed. In this case the complex frequencies ω can be computed as eigenvalues of (5.2) using e.g. a QZ algorithm. Depending on the sign of the imaginary part of ω, the perturbation will either grow or decay exponentially in time .

- in the spatial approach, the circular frequency of perturbations $\omega \in \mathbb{R}$ is imposed, so the wavenumber $k \in \mathbb{C}$ appears in (5.2) as the solution of a quadratic eigenvalue problem, which can be converted to a regular eigenvalue problem and solved similarly to the temporal case.

Figure 5.1 presents the spatial growth rate as a function of the frequency for an inviscid incompressible plane shear layer with a tanh profile (data taken from Ho and Huerre (1984)). In this case, the only length scale is the shear layer thickness, so the relevant scaling for frequencies is to consider a Strouhal number based on the momentum thickness

$$St_\theta = \frac{f^*\theta^*}{U_0^*} = \frac{\theta}{R}\frac{\omega}{2\pi}$$

It appears that only a limited range of frequencies is spatially amplified, characterized by $0 \leq St_\theta \leq 0.08$. The optimal spatial growth is achieved for $St_{opt} = 0.032$, and for this frequency the corresponding spatial growth rate is

$$k_{i,\theta} = k_i^*\theta^* = \frac{\theta}{R}k = 0.12$$

In the case of a spatially evolving shear layer, the momentum thickness varies with the steamwise position x, and consequently, so does the range of amplified frequencies and the associated growth rates. Long wavelengths are weakly amplified at any position, but large spatial growth only occurs in a limited region of strong shear.

In the case of a viscous jet flow profile, the stability features are similar to the case presented above but additional length scales are introduced by the jet radius and viscous effects. Figures 5.2 and 5.3 display temporal and spatial stability features at various axial locations for the model mean flow described in chapter 4. From such an analysis, one could expect that the least stable structures would come from the shear layer right downstream of the nozzle, and have sizes of the order of the inlet shear layer thickness and frequencies scaling with St_θ. This is not what has been observed in experiments: Crow and Champagne (1971) showed that, fairly independently of the inflow conditions, the structures observed in the shear layer have frequencies that scale with St which suggests that the dynamics of instabilities comes from a "global" mechanism. Indeed for a typical jet mean flow, the shear layer thickness increases through the potential core, such that quite independently of the inlet conditions it is of order 1 at the end of the potential core, $x \approx 8$. Figures 5.2 and 5.3 show that for $x \geq 8$ the flow is both spatially and temporally stable to axisymmetric perturbations. Non-parallel effects are therefore expected to play an important role in the "global" behavior of

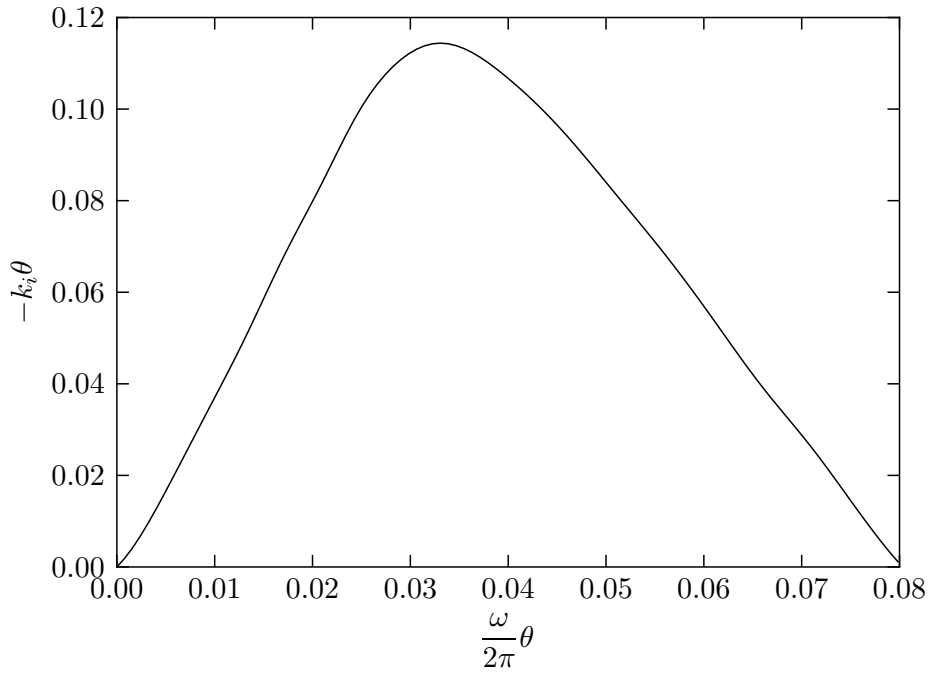

Figure 5.1: Spatial instability features of an inviscid incompressible shear layer (data taken from Ho and Huerre (1984)).

perturbations. In order to capture them, Crighton and Gaster (1976) performed a WKB analysis of jet flows in a spatial framework. Such a study provides insight into the spatial behavior of forced structures, but can not explain the intrinsic behavior, in particular the decay rates of the eigenmodes as a function of their frequencies.

In the following paper, the "global" behavior is investigated through eigenmodes of the LNS equations in a 2D domain, with no assumption on the spatial structure or on the temporal evolution of the perturbations. This analysis aims at (i) accurately taking into account the non-parallelism and (ii) providing both the spatial and temporal evolution of eigenmodes.

5.1.2 Local shear-layer and jet-column modes

Figure 5.4 shows a portion of the spatial spectrum for one given frequency at different streamwise locations. In addition to the shear-layer modes discussed above, that may be stable or unstable, the local stability analysis also shows

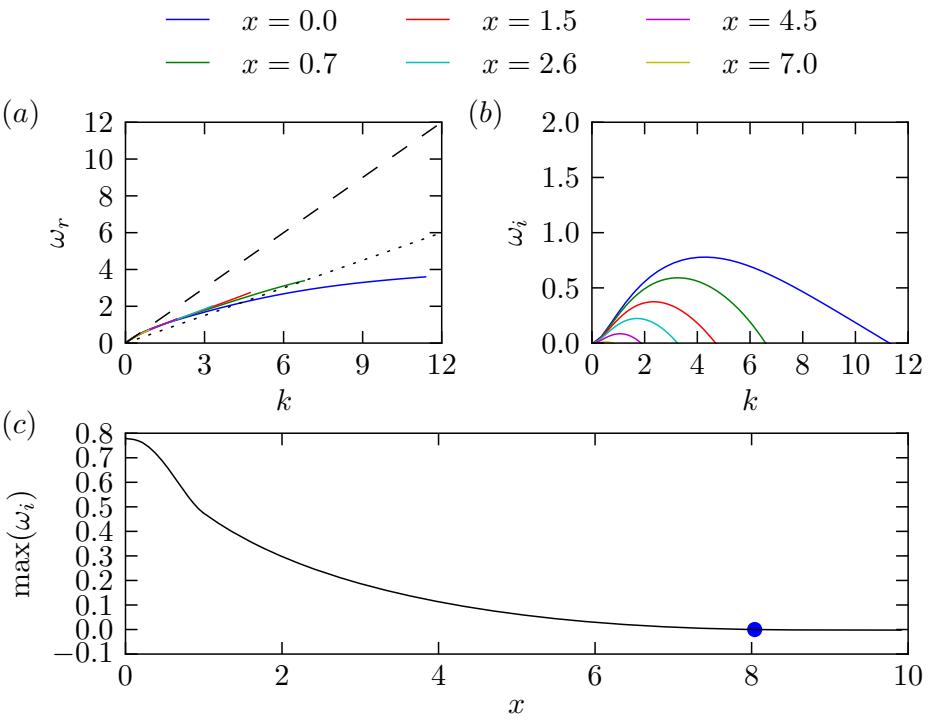

Figure 5.2: Temporal stability properties of the model incompressible jet for $m = 0$. (a, b): real and imaginary parts of the unstable eigenfrequency are displayed as a function of the wavenumber k for different streamwise locations. (c): maximum temporal growth rate as a function of the streamwise location. The location where the flow becomes temporally stable for $m = 0$ is displayed by the blue dot.

the presence of a family of stable eigenmodes (shaded area in figure 5.4). These modes are referred to as jet-column modes. The analysis of their radial distribution reveals that these modes are concentrated close to the jet axis. The least stable jet-column modes are very weakly damped, and their phase velocity is approximately equal to the jet centerline velocity.

5.1.3 Convective instability

The modal analyses presented above are concerned with either the temporal dynamics of perturbations of a given wavelength or with the spatial evolution of perturbations with a given frequency. In a purely parallel flow, temporal instability of a flow only means that the amplitude of some Fourier compo-

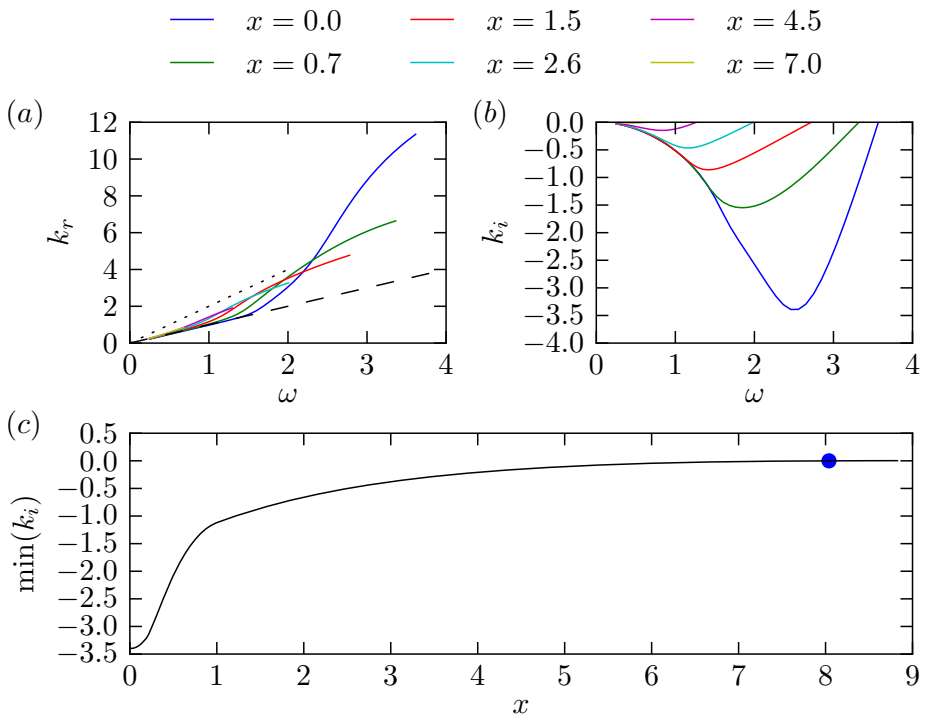

Figure 5.3: Spatial stability properties of the model incompressible jet for $m = 0$. (a, b): real and imaginary parts of the unstable eigenfrequency are displayed as a function of the circular frequency ω for different streamwise locations. (c): maximum spatial growth rate as a function of the streamwise location. The location where the flow becomes spatially stable for $m = 0$ is displayed by the blue dot.

nents will grow exponentially in time. In an infinite domain, a localized initial condition (a Dirac delta function) will therefore generate a disturbance with a L^2 norm which will grow exponentially in time. Two situations may occur: the disturbance may grow in time at any location for long times, in which case the flow is referred to as absolutely unstable, or the disturbance may grow as it travels downstream, in which case the flow is said to be convectively unstable. Quantitative analysis of the absolute/convective behavior of a flow can be carried out based on the saddle points of the dispersion relation associated with (5.2). It has been shown (Monkewitz and Sohn 1988) that isothermal jets are convectively unstable so the norm of any initial perturbation measured on a finite domain will eventually decay to zero for long times. The short time dynamics of perturbations is therefore of interest. These are

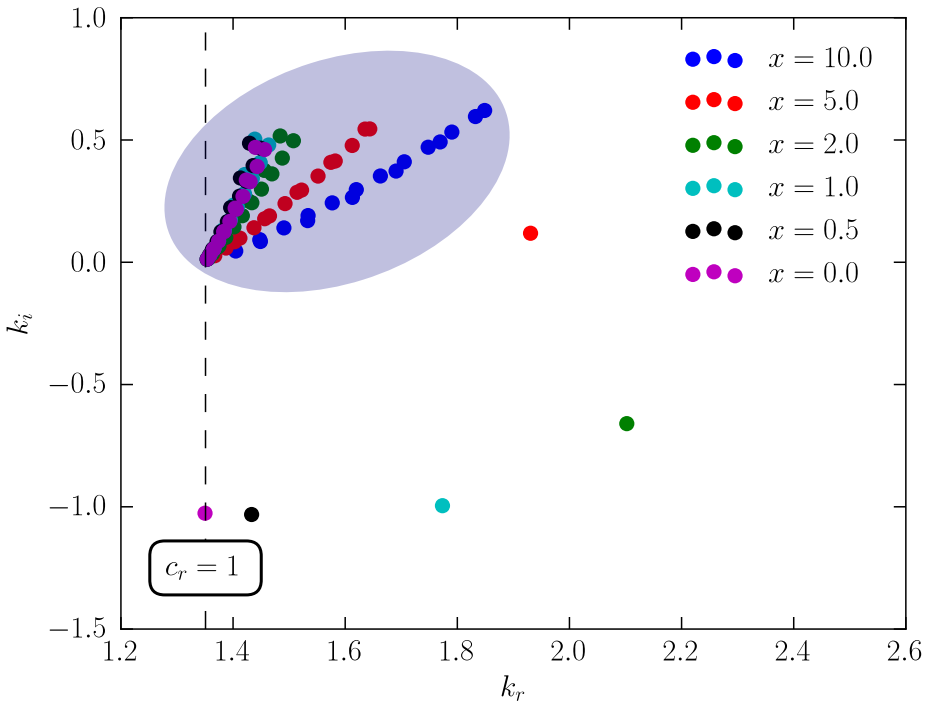

Figure 5.4: Portion of the spatial spectrum at different locations for the model incompressible jet for $m = 0$ and $\omega = 1.35$. The shaded area corresponds to jet-column modes.

studied in terms of "optimal perturbations" (Reddy and Henningson 1993) for both compressible and incompressible flows.

5.1.4 Helical perturbations

Right downstream of the nozzle, where shear is strong, the instability features of axisymmetric and helical perturbations are similar, but significant differences occur further downstream. Michalke (1984) showed that bell-shaped velocity profiles, that are stable for an azimuthal wave number $m = 0$ are unstable for $m = 1$. Figure 5.5 shows the maximum temporal growth rate of the velocity profiles at different streamwise locations for the model mean flow: while the flow is stable for $x \geq 8$ for $m = 0$ is remains unstable through the domain for $m = 1$.

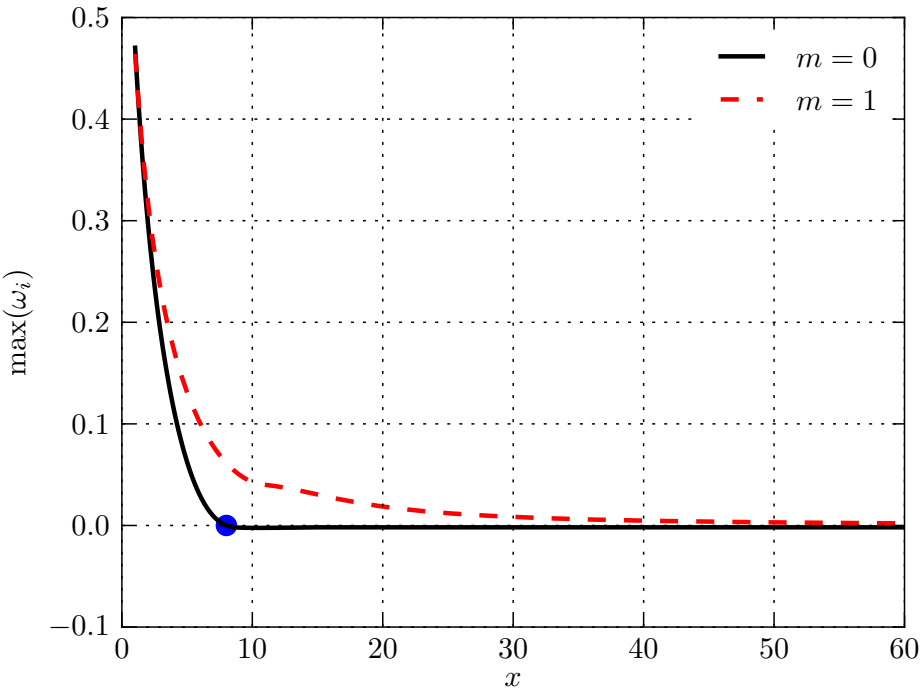

Figure 5.5: Maximum temporal amplification as a function of the streamwise position x for $m = 0$ and $m = 1$. The location where the flow becomes spatially stable for $m = 0$ is displayed by the blue dot.

5.2 Paper: *Modal and transient dynamics of jet flows*

The following paper describes the dynamics of perturbations in incompressible and compressible isothermal jets at both short and long times, through the computation of the optimal perturbations and the 2D "global" eigenmodes of the Linearized Navier–Stokes equations.

Modal and transient dynamics of jet flows

X. Garnaud,[1, a)] L. Lesshafft,[1] P.J. Schmid,[1] and P. Huerre[1]
LadHyX, Ecole Polytechnique – CNRS, 91128 Palaiseau, France.

The linear stability dynamics of incompressible and compressible isothermal jets are characterized by means of their optimal initial perturbations and of their temporal eigenmodes. The transient growth analysis of optimal perturbations is robust and allows physical interpretation of the salient instability mechanisms. In contrast, the modal representation appears to be inadequate as neither the computed eigenmode spectra nor the eigenmodes themselves allow a characterization of the flow dynamics in these settings. More surprisingly, numerical issues also prevent the reconstruction of the dynamics from a basis of computed eigenmodes. An investigation of simple models reveals inherent problems of this approach in the context of a stable convection-dominated configuration, and provides an understanding of several counter-intuitive results: the exponential spatial growth of a stable eigenmode does not necessarily imply a convective instability of the flow.

I. INTRODUCTION

Jets are known to sustain large-scale perturbation structures, both in the laminar and turbulent flow regime. These structures are commonly interpreted as wavepackets developing within a laminar steady base state, or a turbulent mean flow, due to inflectional instability mechanisms. The spatial shape of the wavepacket envelope then depends on the downstream development of the base or mean flow. In order to fully account for the effects of non-parallelism, the present study seeks to identify wavepacket structures in the form of temporal eigenmodes of the linearized equations of motion in a two-dimensional domain. Linear "global modes" of this kind have been investigated for a large variety of flow configurations in recent years; examples include vortex shedding in the cylinder wake[1] or in a three-dimensional jet in crossflow[2], and the flapping of a separated boundary layer[3]. Weakly nonlinear flow dynamics may in some cases be described by a combination of several dominant global modes[4,5]; furthermore, passive[6] as well as active[7] control strategies for the suppression of flow oscillations have been devised based on the knowledge of the global mode spectrum. However, Barbagallo *et al.*[8] showed that a model reduction based on eigenmodes successfully captures the unstable structures but fails to represent the stable dynamics.

All of the above examples represent oscillator-type flows, where intrinsic flow oscillations observed in the nonlinear regime are found to be linked to the presence of at least one unstable linear global mode. In open shear flows, global instability is typically associated with the presence of a locally absolutely unstable flow region[9], although feedback mechanisms may also be responsible for the flow destabilization. In contrast, amplifier-type flows are characterized by a stable global eigenspectrum. Consistent with the notion of local convective instability, non-normal interaction of stable global modes may give rise to transient perturbation growth[10], but ultimately all perturbations decay in time. Jets, unless sufficiently hot[11,12], are prominent examples of amplifier-type flows. Crow & Champagne[13] measured the flow response in low-Mach number turbulent jets as a function of the forcing frequency, and found maximum amplification to occur at a Strouhal number of 0.3. This approximate value for the *preferred mode* has been confirmed in numerous later studies to be remarkably universal over a large range of operating conditions, even in the supersonic regime[14]. Huerre & Monkewitz[9] hypothesized that the preferred mode was the manifestation of a "slightly damped oscillator" character of the flow, i.e. that the strong flow response may be interpreted as a resonance of the least stable global mode in the presence of external

a)Electronic mail: garnaud@ladhyx.polytechnique.fr

forcing. Such an eigenmode has been identified by Cooper & Crighton[15] by extending the dispersion relation of the local shear-layer mode into the complex X-plane. The authors report a Strouhal number based on the diameter of 0.44 for this mode, in agreement with experimental observations[16]. This earlier analysis is based on the hypothesis of the contribution of one single local mode to the global response and of a slow streamwise development of the flow.

Motivated by these results, the first objective of the present study is to compute the global spectrum of subsonic jets. A laminar steady state as well as a turbulent mean flow are considered in the incompressible limit, and the turbulent mean flow is further investigated in the compressible setting at a Mach number of 0.75.

Stable global spectra have been successfully computed for supersonic jets by Nichols & Lele[17,18]. In weakly non-parallel laminar settings, these calculations required extremely large numerical domains, extending over up to 800 jet radii in the downstream direction, in order to capture the wavepacket maximum and reach convergence. In turbulent mean flows obtained from RANS calculations, the dominant modes were sufficiently localized near the nozzle to be accurately resolved on much shorter domains. However, difficulties with the computation of stable global modes have been reported for a variety of flow configurations. Barkley *et al.*[19] obtained easily converged modes that are localized within the recirculation bubbles behind a backward-facing step, but no convergence was achieved for a family of stable modes exhibiting spatial growth far downstream of the step; these modes therefore were not further explored. Similar problems were encountered in planar wakes with surface tension[20,21]. In a flat plate boundary layer[22], all modes are stable and spatially growing. Convergence with respect to the domain length was achieved in this case through the use of carefully designed boundary conditions, based on the local dispersion relation. Amplitudes at the in- and outflow differed by two orders of magnitude. Much larger variations occurred in the analysis of a Batchelor vortex by Heaton *et al.*[23]; amplitude differences on the order of 10^6 were found to prevent convergence. The second and principal objective of the present paper is to expose the root cause for such computational problems of stable global modes, and to delineate circumstances under which convergence may be impossible to achieve.

Earlier studies[24,25] has been shown that individual eigenmodes may carry a limited physical meaning in the context of amplifier flows and that non-modal stability analyses are more suitable to represent instability features in this case. An eigenmode representation of the dynamics can however be used to carry out these analyses, and previous investigations have shown that this provides a robust means of analyzing non-normal effects[22,26] as well as of performing control[7] for weakly unstable flows. Optimal perturbations will therefore be computed in order to characterize transient growth phenomena in jets. Results obtained using both an adjoint method[27] and a modal representation of the propagator[28] will be discussed.

The significance and challenges of a modal representation of the dynamics for advection dominated flows is first investigated by means of model systems in § II. The flow configuration of a round jet with a solid nozzle is then presented in § III, together with the numerical procedure and the different base flows that are investigated. The results of optimal perturbation (§ IV) and eigenmode (§ V) computations are then presented. Although most of the discussion is established in the context of incompressible flows, compressibility effects are also examined. Conclusions are drawn in § VII.

II. MODEL PROBLEMS: EIGENMODES OF ADVECTIVE SYSTEMS

Reddy & Trefethen[29] investigated the features of the spectrum and pseudo-spectrum of a 1D convection-diffusion problem with homogeneous Dirichlet conditions at the inflow and outflow, a well posed Sturm-Liouville type of problem. The eigenmodes exhibit an exponential spatial growth, and a boundary layer forms at the outflow. In contrast, in the model considered in Cossu & Chomaz[30] eigenmodes have a Gaussian envelope. The two models presented below aim at reproducing some of the features of a flow where instability mechanisms act in an upstream region, creating structures that are convected downstream

by a neutrally stable flow. These models show features similar to the problem considered by Reddy & Trefethen and provide an understanding of the relationship between the decay rate of a mode, its spatial structure and local instability features.

A. Advection equation with upstream boundary forcing

The simplest possible model for the evolution of perturbations in an advection-dominated flow is given by a pure advection equation with one spatial direction x and a constant advection velocity $U_0 > 0$. The system is forced by an unsteady upstream boundary condition with its own dynamics,

$$\frac{\partial \psi}{\partial t}(x,t) + U_0 \frac{\partial \psi}{\partial x}(x,t) = 0 \qquad x > 0, \tag{1a}$$

$$\psi(0,t) = \psi_0(t), \tag{1b}$$

$$\dot{\psi}_0(t) = -a\psi_0(t) \qquad a \in \mathbb{C}. \tag{1c}$$

The dynamics of this system are imposed by the linear ODE (1c). The system (1) only has one single mode of the form $\psi(x,t) = \widetilde{\psi}(x)\,\exp(-\mathrm{i}\omega t)$, with eigenvector $\widetilde{\psi}(x)$ and eigenvalue ω given by

$$\widetilde{\psi}(x) = \exp\left(\frac{a}{U_0}x\right), \qquad \omega = -\mathrm{i}a. \tag{2}$$

If the system is stable, $a_r \geq 0$ (subscripts $_r$ and $_i$ denote, respectively, the real and imaginary parts of complex scalars and vectors), the amplitude of the mode grows exponentially in x and diverges as $x \to \infty$. A lower advection velocity U_0 leads to stronger spatial growth of $\widetilde{\psi}(x)$.

It is quite clear from this simple example how a temporally decaying source of perturbations under pure advection gives rise to a spatially growing structure, since all perturbations generated at a later time must be exponentially smaller than those generated earlier. Furthermore, this model also serves to exemplify the occurrence of spurious numerical modes. If (1) is discretized using a first-order upwind scheme on a uniform mesh, the mode (2) is recovered independently of the size of the numerical domain, but a second eigenvalue is found as $-1/h$, where h is the grid spacing. The corresponding spatial structure is localized at the outflow discretization point. If a general non-uniform mesh with n points is used, then n distinct modes exist, localized anywhere on the grid. In this particular example, $n-1$ of them have no physical meaning because they do not correspond to modes of the continuous problem. In a more general case where no *a priori* knowledge about the modal structure is available, care must be taken with numerically computed modes. Although the discretization method is suitable for transient problems, it is possible that even the least stable modes computed numerically may have no physical meaning.

B. Unforced Ginzburg–Landau equation

It may be argued that the above model is indeed too simple for a comparison with jet dynamics, since information can only propagate downstream. This property, however, is not the cause for the exponential spatial growth. A similar reasoning can be applied to the linear Ginzburg–Landau equation, given as

$$\frac{\partial \psi}{\partial t} + U_0 \frac{\partial \psi}{\partial x} = -a(x)\psi + \frac{\partial^2 \psi}{\partial x^2} \qquad x > 0, \tag{3a}$$

$$\psi(0,t) = 0. \tag{3b}$$

At each individual location x, the system is known[31] to be locally stable if $a(x) < 0$, convectively unstable if $0 < a(x) < U_0^2/4$ and absolutely unstable if $a(x) > U_0^2/4$.

Cossu & Chomaz[30] considered solutions of a problem of the form (3a) that are bounded in $\mathbb{R}$, and assumed the instability parameter $a(x)$ to be of a parabolic shape $a(x) = \alpha x^2 + \beta$, with $\alpha > 0$, such that the spatial and temporal growth rates tend to $-\infty$ as $x \to \pm\infty$. Eigenmode shapes are recovered analytically, and they are found to decay as $\exp(-x^2)$ for large x.

On the contrary, if a reaches a *finite* value a_∞ as $x \to \infty$, perturbations do not experience arbitrarily strong spatial or temporal decay. For a demonstration of the spatial behavior, this limiting value a_∞ can be taken as 0 without loss of generality, as it only affects the temporal eigenvalue but not the corresponding eigenfunction. In order to model a situation where instability mechanisms are active around a given position, while passive convection and diffusion of perturbations is dominant throughout the rest of the domain, let the instability parameter $a(x)$ be of the form

$$a(x) = a_0(\mathrm{i} - 1)\mathrm{e}^{-(x-2)^2}, \quad a_0 > 0. \tag{4}$$

In order to numerically solve (3)–(4) on the interval $[0, x_\infty]$, a boundary condition has to be imposed at the outflow $x = x_\infty$. While a homogeneous Dirichlet boundary condition can be imposed for $a(x) = \alpha x^2 + \beta$ with $\alpha > 0$, this would result in the formation of a boundary layer at the outflow in our present case[32]. In order to take into account convective effects at the outflow, $\psi''(x_\infty) = 0$ is imposed. This "convective outflow"-type boundary condition neglects viscous effects at $x = x_\infty$. Results are qualitatively similar when imposing a homogeneous Neumann boundary condition, but the truncation effect is stronger.

Figure 1 shows the effect of the different parameters on the spectrum as well as on the leading eigenmode $\psi^{(0)}$. Figure 1(a) shows that, for $a_0 = 1$, the system changes from globally unstable to stable as U_0 is increased. At low values of U_0, the leading eigenmode reaches a maximum around $x = 2$ and decays exponentially downstream (figure 1(b)). As U_0 increases, the temporal decay of the mode becomes stronger, and the spatial maximum eventually disappears: exponential growth is observed essentially throughout the entire domain. As observed previously[22], the spatial growth rate of the global mode corresponds to the local spatial growth rate at the global frequency.

For $U_0 = 4$ and $U_0 = 5$, the largest values of U_0 considered in figure 1(a, b), the overall shape of the spectrum completely changes. Figure 1(b) shows that in these cases, exponential growth occurs throughout the domain, and the amplitude of the mode varies by a factor of 10^{16} between $x = 0$ and the outlet at $x = 25$: the modes, and in particular the region $1 < x < 3$ where instability mechanisms act, cannot be resolved numerically. This phenomenon can also be seen as the length of the domain is increased for fixed U_0 and a_0. The same behavior is observed for $a(x) \in \mathbb{R}$, in which case the spectrum should lie on the imaginary axis, indicating that none of these computed modes actually correspond to modes of the continuous problem. Figure 1(c) shows that the eigenvalues returned by the eigensolver for $U_0 = 5$ approximately lie on the 10^{-14} contour of the pseudospectrum of the discrete operator which, in this case, does not provide a good approximation to the spectrum. In situations where the amplitude of the mode cannot be represented throughout the domain, even the QZ algorithm fails to compute an accurate approximation to the discrete spectrum.

The relative effect of the instability parameter and of the advection velocity is summarized in figure 1(d), where the spatial growth rate of the leading eigenmode is represented as a function of the two parameters U_0 and a_0. From this growth rate, it is possible to evaluate the maximum domain length for which the computation is possible using double precision arithmetics. The dashed lines displayed in figure 1(d) correspond to values of (a_0, U_0) for which the numerical truncation errors prevented the computation.

C. Conclusions from model problems

The above examples have shown that the spatial behavior to be seen in § V A for the eigenmodes of the Navier–Stokes equations is not inconsistent, and that it does not correspond to a spatial instability within a local framework. In the case where the flow dynamics are dominated by convection and diffusion effects, the downstream evolution of the modes

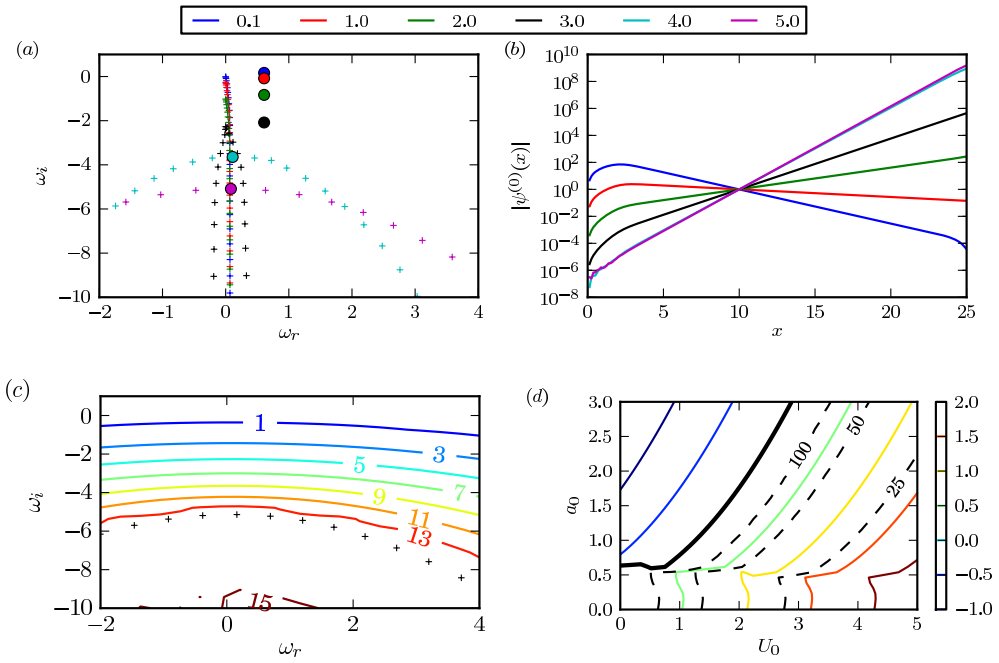

FIG. 1. (a, b): effect of U_0 on the leading eigenmodes for the Ginzburg–Landau model (for $x_\infty = 25$ and $a_0 = 1$). The least stable part of the eigenvalue spectrum is shown in (a), and the leading eigenmode for each value of U_0 (represented in (a) by circles) are displayed in (b). (c): spectrum (+ symbols) and iso-contours of the pseudo-spectrum for $x_\infty = 25$, $U_0 = 5$ and $a_0 = 1$ (logarithmic scale). (d): Spatial growth rate of the leading global mode (measured as $\psi^{(0)\prime}(10)/\psi^{(0)}(10)$) as a function of parameters a_0 and U_0. The solid contour represents the limit between growing and decaying modes, the dashed lines gives the maximum value of the advection parameter for which computation is possible in a domain of a given length (indicated on the curve).

results from two opposing mechanisms: the local stability of the flow tends to decrease the amplitude of the mode in the streamwise direction, but the advection of the globally stable structures has the opposite effect. In the case of a parabolic profile for a, the local stability eventually dominates for large x and the global modes decay to 0. On the contrary for $a \to a_0$ as $x \to \infty$ the local stability is not necessarily strong enough to prevent exponential spatial growth. The second model pointed out that, when convective effects dominate as $x \to \infty$, the size of the computational domain should be small enough that the amplitude of the mode can be resolved throughout the domain, otherwise numerical accuracy becomes problematic as the 10^{-15}-pseudospectrum can extend far from the spectrum[29]. The following section will present details on how this affects the computation and the convergence of modes for the Navier–Stokes system.

III. SETUP OF THE JET PROBLEM

A. Flow configuration

a. Incompressible setting

A cylindrical jet of a Newtonian fluid with viscosity ν^*, of radius R^* and exit velocity U_0^* is considered. The two latter quantities are used to make lengths and velocities non-

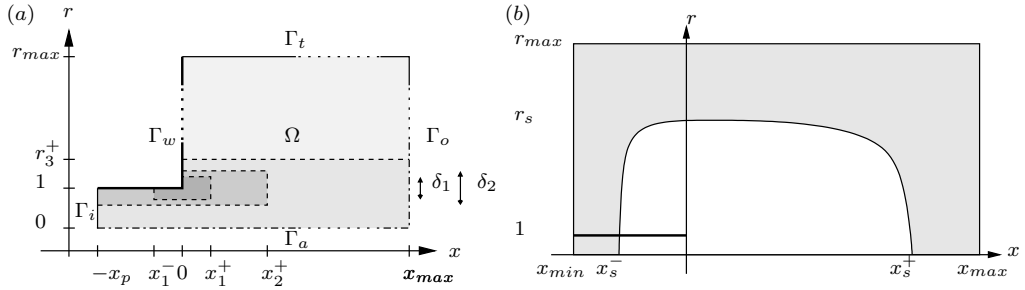

FIG. 2. Flow configuration for (a) incompressible and (b) compressible computations . The incompressible Navier–Stokes equations are solved on the 2D domain Ω using a Finite Element formulation, with an inflow BC on Γ_i (thin solid line), a no slip BC on Γ_w (thick solid line), a stress-free BC on Γ_o (dashed line) and compatibility conditions on the axis Γ_a (dash-dot line). No sponge layers are used in this case. The compressible Navier–Stokes equations are discretized using high order Finite Differences (FD) on the rectangular domain represented in (b). The shaded regions correspond to sponge layers, and the presence of an infinitely thin adiabatic wall for $r = 1$ and $x \leq 0$ is taken into account by means of appropriate FD schemes.

dimensional. The outer fluid is at rest. The Reynolds number is taken as

$$\mathrm{Re} = \frac{U_0^* R^*}{\nu^*} = 10^3.$$

Frequencies f^* will be reported in terms of the non-dimensional circular frequency ω, related to the Strouhal number St as

$$\mathrm{St} = \frac{2 f^* R^*}{U_0^*} = \frac{\omega}{\pi}.$$

The axisymmetric flow domain, described in terms of cylindrical coordinates r, θ and x, is represented in figure 2(a). The steady solution of the non-linear Navier–Stokes equations (see § III B) is assumed to be axisymmetric. This assumption is no longer made for the perturbations, but in a linear context all perturbation quantities can be decomposed into independent Fourier-modes in θ, by introducing the azimuthal wavenumber $m \in \mathbb{N}$. Consequently, only the two-dimensional (r, x) plane needs to be discretized for both non-linear and linear calculations.

The boundary of the computational domain Ω consists of Γ_i, Γ_w,Γ_t,Γ_o and Γ_a, corresponding to the inlet, a solid wall, the outer radial boundary, the outflow and the jet axis. The inflow velocity is imposed on Γ_i, a no-slip condition on Γ_w, and stress-free boundary conditions are applied on Γ_t[33]. Compatibility conditions on Γ_a ensure a smooth solution on the axis[34]. Unless stated otherwise, stress-free boundary conditions are imposed at the outflow Γ_o.

The length of the pipe included in the numerical domain is set to $x_p = 5$, and it has been verified that setting the domain height to $r_{max} = 10$ does not affect the results of all incompressible calculations.

b. Compressible setting

In addition to the flow parameters introduced above, the compressible setting is characterized by density and temperature scales ρ_∞^* and T_∞^*, defined as the respective values in the outer fluid at rest. Natural choices for the Mach and Prandtl numbers are

$$\mathrm{Ma} = \frac{U_0^*}{c_\infty^*}, \qquad \mathrm{Pr} = \frac{\mu^* C_P^*}{\kappa^*},$$

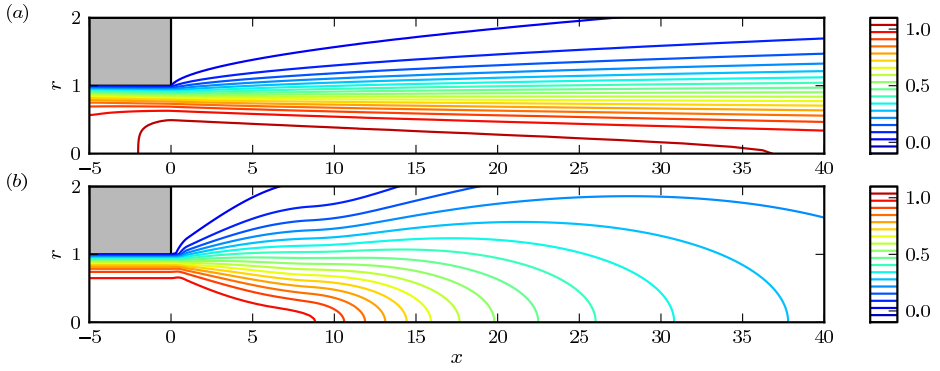

FIG. 3. Axial velocity field of the two base flows. (a) : laminar base flow, computed as a steady solution of the Navier–Stokes equations. (b) : turbulent mean flow, adapted from an analytical model[36].

where $c^*_\infty = \sqrt{\gamma r^* T^*_\infty}$ denotes the ambient speed of sound and C_p the specific heat at constant pressure.

In order to capture the acoustic radiation, the typical extent of the numerical domain has to be of the same order in the axial and radial direction. High resolution Finite Differences (FD) on a rectilinear grid are used to treat such a large problem. Consequently, the geometry (schematically displayed in figure 2(b)) is slightly different than in the incompressible case. In compressible studies, the jet pipe is modeled as an infinitely thin adiabatic wall located at $r = 1$ and $x \leq 0$. Its presence is taken care of by using appropriate FD schemes. The treatment of the far field boundary conditions depends on the type of study performed. As will be shown later, the eigenmodes of the linearized Navier–Stokes equations are not spatially localized, so an accurate treatment of the outer boundaries is needed. To limit as much as possible the reflection of vortical or acoustic waves, the non-reflecting boundary conditions described by Bogey and Bailly[35] are used together with sponge layers. This is not required for the computation of the optimal perturbations which have a limited spatial extent. In the latter case, the sponge layers alone suffice to ensure that the solution decays to zero at the outer boundaries without affecting the flow in the physical region.

B. Base flows

Two types of base flows are investigated in this study: a laminar steady-state solution of the Navier–Stokes equations, and a parametric model of a turbulent mean flow. The incompressible analysis is performed on both these base flows, whereas only the turbulent case is considered in the compressible study.

a. Laminar steady state

A steady flow state is computed as an exact solution of the Navier–Stokes equations (see §III C). The inflow velocity is prescribed on Γ_i as

$$u_x(-x_p, r) = \tanh\left(5(1-r)\right) \qquad u_r(-x_p, r) = 0 \qquad u_\theta(-x_p, r) = 0.$$

This profile has a momentum thickness

$$\delta = \int_0^1 r u_x (1 - u_x)\, \mathrm{d}r \approx \frac{1}{20}.$$

Stress-free boundary conditions are employed at the outflow Γ_o. The resulting base flow is weakly non-parallel, as seen in figure 3(a). A slight growth of the boundary layer in the pipe leads to an increase in the centerline velocity between $x = -x_p$ and 0, so that the exit centerline velocity is 1.06 at $x = 0$.

b. Turbulent mean flow

Based on experimental measurements, Monkewitz & Sohn[36] proposed a model for the turbulent mean flow of compressible jets. The flow field comprises two regions: a potential core extending over a distance of eight jet radii downstream of the nozzle, and an adjoining self-similar region with Gaussian profile shapes. This model is extended in our study by a parallel flow region inside the pipe, which smoothly connects to the free jet over the interval $0 \leq x \leq 1$. The full model is described in detail in Garnaud *et al.*[37]. The resulting streamwise velocity field is displayed in figure 3(b) for the zero-Mach-number case. The formulation does take into account compressibility effects, and finite-Mach-number configurations are used for the compressible analysis. The inflow momentum thickness is prescribed as $\delta^{-1} \approx 23$, similar to the laminar case.

Following Hussein & Reynolds[38], the stability of turbulent flows can be analyzed using a triple decomposition of the flow field into a mean flow, coherent perturbations and fine-scale turbulence. Using this decomposition, turbulent scales affect the motion of instability waves through Reynolds stresses, for which a closure model needs to be provided[39,40]. For turbulent jet flows, successful stability analyses[41,42] have been performed while neglecting the effect of Reynolds stresses, and this approach is also followed here as a first approximation.

C. Numerical methods

a. Incompressible setting

The incompressible Navier–Stokes equations are discretized using Finite Elements (P2-P1), and the zero-divergence condition for the flow velocity is enforced by a penalty method[43]. The incompressible laminar steady flow is computed using Newton's method and the FreeFEM++ software[43]. A direct solver[44] is used for linear systems. Given this steady state or a model turbulent mean flow (see § III B b), the linearized Navier–Stokes equations that govern the evolution of perturbations may be written as

$$B\frac{\partial \boldsymbol{q}}{\partial t} = L\boldsymbol{q} \tag{5}$$

where $\boldsymbol{q}$ is the state vector, containing the values of all degrees of freedom of the velocity and pressure fields. Equation (5) is discretized using FreeFEM++ and the resulting sparse matrices are exported for the linear analysis. The solution of all the problems in § IV and § V A relies on the software libraries PETSc[45], SLEPc[46] and MUMPS[44]. Eigenvalue problems arising in § V A are non-Hermitian, so the Kylov-Schur method is used. In order to compute the least stable eigenmodes the "shift-invert"[47] spectral transformation is applied using a direct linear solver.

In the study of optimal perturbations the amplitude of a perturbation needs to be measured. The square root of the perturbation kinetic energy integrated over the entire domain Ω is used for incompressible flows. This results in a pseudo-norm, as pressure is not taken into account. For the problem to be well posed, the amplitude of the initial condition needs to be measured in terms of a norm. The initial disturbance is therefore assumed to consist only of a velocity perturbation. Let $\boldsymbol{q}_u$ be a vector containing only velocity-related degrees of freedom, and P be a matrix that associates $\boldsymbol{q}_u$ to a state vector where pressure-related degrees of freedom are zero. Conversely, the operator $P^\dagger$ removes these degrees of freedom from a full state vector $\boldsymbol{q}$. The pseudo-norm is then obtained as

$$\|\boldsymbol{q}\|^2 = \boldsymbol{q}_u^\dagger Q_u \boldsymbol{q}_u = \boldsymbol{q}^\dagger P Q_u P^\dagger \boldsymbol{q} = \boldsymbol{q}^\dagger Q \boldsymbol{q} \tag{6}$$

where Q_u is a Hermitian definite matrix.

The computation of optimal perturbations described in § IV requires (i) a direct time stepper, (ii) an adjoint time stepper and (iii) an eigenvalue solver. The linear equations of motion are marched forward in time using the Crank-Nicolson method (steps (i) and (ii)). A discrete adjoint is used for step (ii), based on the Hermitian transpose of the discretization matrices. Finally, as the eigenvalue problem to be solved is Hermitian, the Lanczos method is used.

b. Compressible setting

The linearized compressible Navier–Stokes equations are spatially discretized using a finite-difference scheme designed for aero-acoustic studies[48]. The resulting discretization matrix is sparse, but with an important number of nonzero elements, in particular due to the stencil of the cross derivative terms which involves here 121 discretization points. Another consequence of the large FD stencils is that the bandwidth of the sparse discretization matrices becomes relevant, leading to excessive memory requirements for direct solvers. Iterative solvers could be used instead[49], but these methods are very sensitive to the design of an efficient preconditioner and robustness may be an issue. In order to circumvent these problems, all of the analysis is performed using an algorithm based on time stepping of linear equations (an explicit third order Runge-Kutta method is used here). In such a framework, the structure of the discretization matrices is not needed, therefore a matrix-free approach is used. Compressible eigenmodes are computed by use of a relaxation method[50], which is based on the application of a bandpass frequency filter to the equations of motion. This method allows to solve very large eigenvalue problems with low memory requirements. However, our experience shows that the relaxation method in general does not reach the machine-precision accuracy that is possible with the shift-invert method.

The adjoint Navier–Stokes operator is needed for the computation of optimal perturbations (§ IV). A discrete adjoint formulation is chosen, following the memory-efficient approach of Fosas *et al.*[51]. The norm used is that of Hanifi *et al.*[52]. Care is taken with the selective spatial filter so that the discrete propagator of the adjoint equations is the adjoint of the discrete direct propagator up to machine precision.

IV. TRANSIENT GROWTH OF PERTURBATIONS

The initial condition $\boldsymbol{q}(0)$ that is most amplified over a finite time interval T is referred to as the *optimal perturbation* for T. Reddy & Henningson[32] established the notion of optimal perturbations in order to characterize the transient (short-term) linear dynamics of flow systems. Let the amplification factor be defined as

$$G_m(T) = \max_{\boldsymbol{q}(0)} \frac{\|\boldsymbol{q}(T)\|}{\|\boldsymbol{q}(0)\|} \,. \tag{7}$$

Furthermore, let $\mathcal{P}_T$ be the propagator, i.e. the linear operator that advances an initial condition over the time interval T according to equation (5). The optimal gain $G_m(T)$ is found as the leading eigenvalue of the operator $Q_u^{-1} P \mathcal{P}_T^\dagger Q \mathcal{P}_T P^\dagger$, and the associated eigenvector represents the optimal perturbation. The eigenvalue problem is solved using the Lanczos method, as implemented in the SLEPc library. The operators $\mathcal{P}_T$ and $\mathcal{P}_T^\dagger$ are applied using the time steppers described in § III C, and Q_u^{-1} is determined using a Cholesky decomposition (in the case of a finite-difference discretization, this decomposition is easily performed by hand).

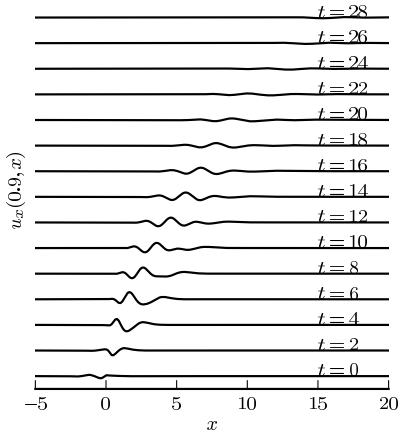

FIG. 4. Spatio-temporal evolution of the optimal initial condition for $m = 0$ and $T = 10$ for the turbulent jet mean profile in the incompressible case. The value of the axial velocity along the line $r = 0.9$ is represented at various time steps, as indicated next to the curve.

A. Incompressible flow

In the incompressible setting, the length of the computational domain is chosen as $x_\infty = 40$, and stress-free boundary conditions are employed at the outflow. The convergence of the results with respect to the spatial and temporal discretizations has been verified by using (i) a halved time-step and (ii) a finer mesh where the cell size in the near-nozzle region is divided by more than 3. For both the laminar and the turbulent base flows, and for all azimuthal wave numbers and time horizons, the optimal perturbation is found in the form of structures localized in the boundary layer upstream of the nozzle, and the perturbations are amplified as they travel downstream. A typical example is shown in figure 4, which displays the evolution of the optimal perturbation of the turbulent jet for $m = 0$ and $T = 10$, along the line $r = 0.9$.

The optimal gain as a function of time horizon T is displayed in figure 5 for both base flows. In the case of the laminar base flow, this amplification factor grows monotonically with T as long as the perturbation is contained inside the numerical domain. Very large amplitudes are reached, comparable to similar computations in the supersonic regime by Nichols & Lele[17]. In the case of the turbulent base flow (figure 5(b)), the gain reaches a maximum for a finite time horizon $T_{opt,m}$. This maximum is particularly pronounced for axisymmetric perturbations ($m = 0$), with $T_{opt,0} \approx 10$. This interval roughly corresponds to the advection time of the initial perturbation across the potential core. Downstream of the potential core, axisymmetric perturbations decay as they travel on. Non-axisymmetric perturbations may still experience further growth beyond the potential core, and the decay of $G_m(T)$ with T is slower as a consequence. This observation is consistent with the fact that bell-shaped profiles in the self-similar regime may be unstable for $m \neq 0$ but not for axisymmetric perturbations[53]. Both the laminar and the turbulent settings display the largest gains for helical perturbations $m = 1$. It may be conjectured that a *lift-up* mechanism[54] is responsible for the strong growth of helical perturbations, since such a mechanism can only exist at azimuthal wavenumbers $m \neq 0$. However, no firm evidence of lift-up effects can be reported at present.

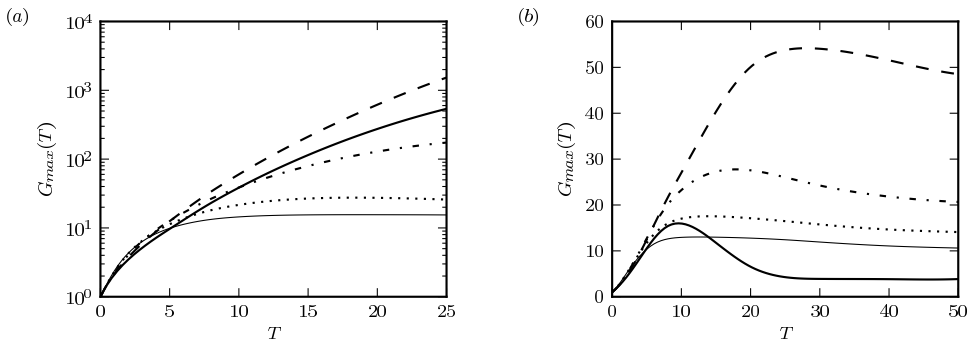

FIG. 5. Gains associated with the optimal perturbations for (a) the laminar and (b) the model base flows.Thick solid line : $m = 0$, dashed line : $m = 1$, dash-dotted line : $m = 2$, dotted line : $m = 3$ and thin solid line $m = 4$.

B. Effects of compressibility

Corresponding results of optimal perturbations of the turbulent mean flow at $Ma = 0.75$ are displayed in figure 6. The qualitative behavior of $G_{max}(T)$ (shown in figure 6(a)) is similar to that obtained for incompressible flows (figure 5(b)), and the amplification levels are comparable, although perturbations are not measured in the same norm. The spatial shape of optimal perturbations for short time horizons also resembles those found in the incompressible setting. Figures 6(b, c) show the optimal perturbation for $T = 12$: vortical structures in the pipe boundary layer are amplified as they travel through the jet shear layer. However, compressibility allows a different scenario at longer time horizons $T \gtrsim 25$, as shown in figures 6(d, e): the optimal initial condition takes the form of a spherical acoustic pulse that *contracts* and hits the nozzle at a finite time. A vortical wavepacket is thus created at the nozzle, which is amplified while it propagates through the potential core. This result illustrates that acoustic waves can be very efficiently converted into vortical perturbations at the nozzle tip[55–57].

V. MODAL ANALYSIS

A. Incompressible global modes

a. Spectrum of the laminar base state

Eigenmodes of the linear equations (5) are sought in the form $\boldsymbol{q}(t) = \widetilde{\boldsymbol{q}} \exp(-\mathrm{i}\omega t)$, such that $\widetilde{\boldsymbol{q}}$ and ω satisfy the generalized eigenvalue problem

$$-\mathrm{i}\omega B\widetilde{\boldsymbol{q}} = L\widetilde{\boldsymbol{q}}. \tag{8}$$

Stress-free boundary conditions are used at the outflow Γ_o, and eigenmodes are computed for $x_\infty = 60$ with various shift parameters. The resulting spectra for the laminar base flow are shown in figure 7(a).

All eigenvalues have a negative growth rate $\omega_i \leq 0$ and therefore are stable. This finding is consistent with local instability results from the literature, which have shown isothermal jets to be convectively unstable[36], except in rare circumstances[58].

Several families of modes can be identified from figure 7(a). A first branch of modes, starting at the origin, is represented as blue circles. The least stable of these modes correspond to vortical structures in the free-stream, as displayed in figure 7(b). The wavelength of these nearly stationary modes scales with the size of the numerical domain. As the growth

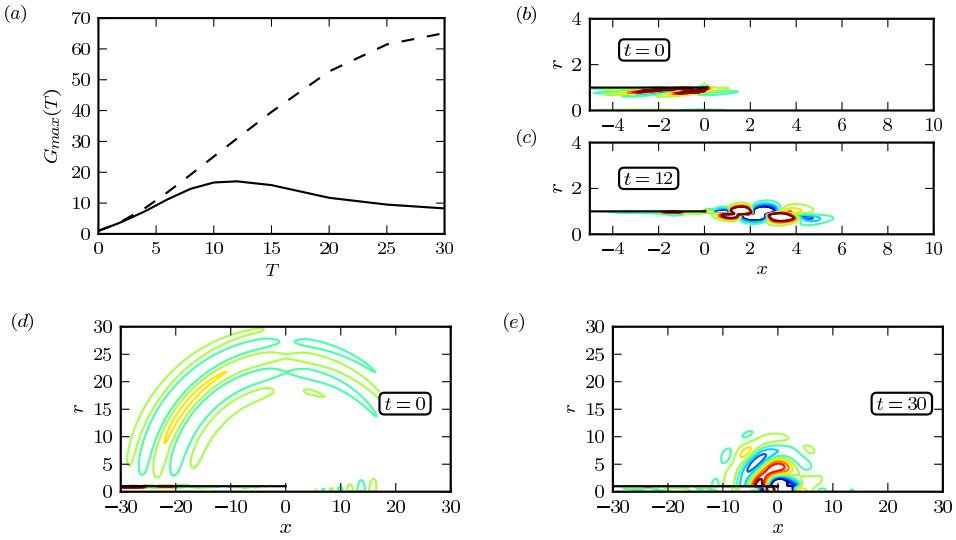

FIG. 6. (a) Optimal perturbations for the model subsonic jet at Ma = 0.75 for $m = 0$ (solid line) and $m = 1$ (dashed line). (b, c) : Azimuthal vorticity field for the optimal initial condition for $m = 0$ and $T = 12$, and the corresponding perturbation at $t = 12$. (d, e) : Dilatation field for the optimal initial condition for $m = 0$ and $T = 30$, and the corresponding perturbation at $t = 30$.

rate decreases along this branch, the branch is distorted and the mode structure tends to be localized more towards the jet shear-layer. This is an effect of the finite extent of the numerical domain that has been observed in other studies[26,59]. A second branch is represented by black $\times$ symbols. These eigenmodes are localized inside the shear layer. At the lowest frequencies, an exponential spatial growth in the streamwise direction is observed throughout the computational domain, as shown in figure 7(c). This behavior is similar to what was observed in the model problems of § II, and by this analogy we attribute the exponential spatial growth to the temporal decay of these modes. At higher frequencies (figure 7(d)), spatial growth is still found downstream of the nozzle, but the mode reaches a maximum amplitude within the computational domain. The maximum growth rate along this branch occurs around the frequency ($\omega_r \approx 1$) for which the location of maximum amplitude of the mode enters the computational domain, suggesting that the maximum in ω_i is an artifact of the finite domain size. Domain truncation effects are investigated in the following section. The phase velocity of all modes along this branch corresponds approximately to half the jet velocity on the centerline; modes at higher frequency therefore display shorter wavelengths, as can be seen in figure 8.

A third family of modes is found, represented by red symbols in figure 7(a). None of these eigenvalues are recovered identically with different shift parameters, indicating a lack of convergence. However, these modes have been computed by the eigenvalue solver with the specified convergence criterion, namely $\|L\boldsymbol{q} + \mathrm{i}\omega\boldsymbol{q}\| < 10^{-10}\|\boldsymbol{q}\|$. We attribute this class of modes to spurious effects arising from finite machine precision. The spatial structure of one such spurious mode is represented in figure 7(e).

All modes represented in figure 7 display very large amplitude variations throughout the free-jet region. If these variations are of the order of machine precision, the low-amplitude dynamics near the nozzle cannot be accurately resolved. The perturbation amplitudes shown in figures 7($b - d$) do not span more than ten orders of magnitude in the free-jet region, and appear to be well-converged. The spurious mode in figure 7(e), in contrast, varies over 14 orders of magnitude, and seems to be affected by the double-precision round-off error as a consequence. In fact, it may be surmised that its very existence is due to the round-off error; this conjecture will be further investigated in the next section. A similar observation

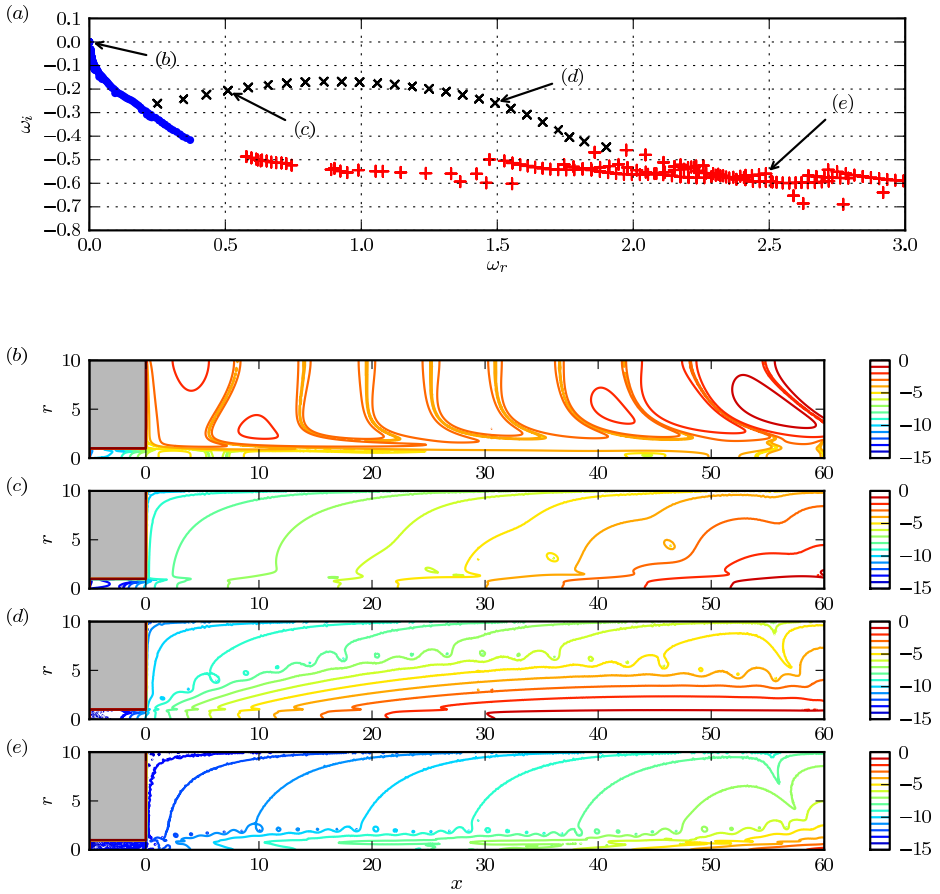

FIG. 7. Global modes computed for $m = 0$ on the laminar base flow. (a): eigenfrequency spectrum. (b, c, d, e): axial velocity magnitude of four selected modes, in logarithmic scale, as indicated in (a).

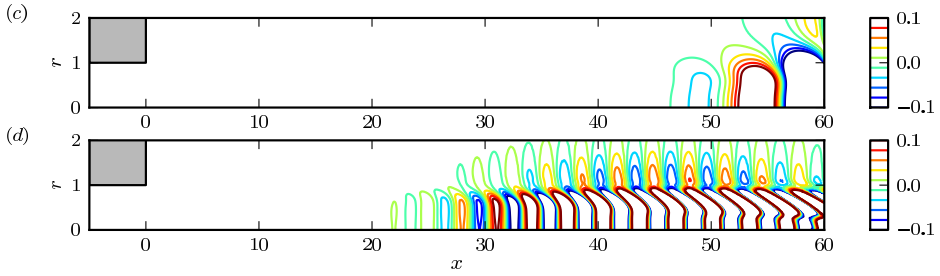

FIG. 8. Axial velocity for global modes (c) and (d) of figure 7, in linear scale.

has been made by Heaton *et al.*[23] in their modal stability analysis of the Batchelor vortex. Those authors report that modes with amplitude variations above a factor of 10^6, between the inlet and outlet of the computational domain, cannot be accurately resolved with their numerical method. With the present algorithm, this limiting factor is approximately 10^{14}.

b. Influence of domain truncation

All eigenmodes displayed in figure 7 reach their maximum amplitude at or near the downstream boundary of the numerical domain. It may therefore be expected that the position of this boundary, as well as the numerical treatment of the outflow condition, should affect the results. In order to evaluate this influence, different domain lengths between 40 and 100 radii have been tested. The results are compared in figure 9(a), which shows that the branches of eigenmodes computed are domain-dependent. A similar behavior has been obtained in the analysis of the Blasius boundary layer[22], and is attributed to the fact that the wavepackets travel throughout the domain. Most importantly, the maximum growth rate of the shear-layer branch shifts to lower frequencies as x_{max} is increased. An inspection of the associated spatial amplitude distributions reveals that this maximum growth rate occurs roughly at the frequency at which the mode maximum amplitude is first captured inside the numerical domain. At low real frequencies, the true amplitude maximum lies on the outflow boundary of the numerical domain, and the eigenvalues are strongly affected by truncation. With increasing real frequency, this amplitude maximum moves further upstream, and the influence of the domain truncation lessens. The mode shapes shown in figure 7 are consistent with this observation. If the trend with increasing domain size is extrapolated, one may expect that the growth rate of the shear-layer branch decreases monotonically with increasing frequency in an infinitely long domain.

While the spectra in figure 9(a) have been computed with stress-free outflow conditions, figure 9(b) displays corresponding results obtained with a "convective outflow" formulation[60]. Both boundary conditions are found to give very similar results. It is inferred from this comparison that the outflow boundary conditions do not have a significant impact on the eigenmode computations in this study.

It appears that the spurious branches become less and less stable as the domain length increases. This branch is interpreted as a consequence of finite precision arithmetics. Under the assumption of a quasi-parallel flow, let C_g be the group velocity of a spurious spatial instability wave forced by numerical noise in the vicinity of the jet pipe,

$$\psi_{sp} = \widehat{\psi}(r)\exp(\mathrm{i}(k_r + \mathrm{i}k_i)x)\exp(-\mathrm{i}\omega t) \tag{9}$$

where ω is the complex forcing frequency. This forced wave will be considered an eigenmode by the solver if the forcing amplitude is of the order of the numerical precision ϵ_m, i.e. if the amplitudes of this forced wave at the inlet and at the outlet are such that

$$\psi(x=0) \sim \epsilon_m \psi(x = x_\infty).$$

In this case, (9) gives $k_i = -\log(\epsilon_m)/x_\infty$. Let $\omega_i^t(k_r)$ be the local temporal growth rate associated with the axial wavenumber k_r. In the limit of long wavelengths, jet flow profiles are approximately marginally stable. Following an approach similar to that of the Gaster transformation[61], the global temporal decay rate ω_i can be related to the global spatial growth rate k_i by

$$\omega_i \approx C_g k_i + \omega_i^t(k_r) \approx C_g \frac{\log(\epsilon_m)}{x_\infty}. \tag{10}$$

As the group velocity C_g is of the order of the base flow velocity U_0, the decay rate associated with such pseudomodes can be estimated as

$$\sigma \equiv U_0 \frac{\log(\epsilon_m)}{x_\infty}. \tag{11}$$

Figure 9 shows that the above expression provides a reasonable estimate for the decay rate of the spurious modes. Since σ varies as $1/x_\infty$, this spurious branch will eventually become less stable than the other two branches as x_∞ increases, preventing their computation. It is thus impossible to obtain converged results for the spectra, at least using standard double precision arithmetic ($\epsilon_m = 10^{-15}$).

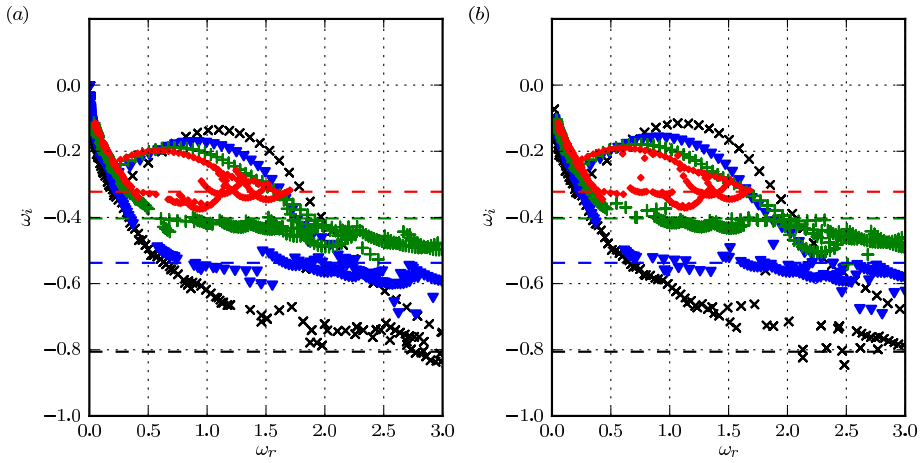

FIG. 9. Spectra computed for various domain lengths using stress-free (a) and convective outflow (b) boundary conditions at the outlet. Black $\times$: $x_\infty = 40$. Blue triangles : $x_\infty = 60$. Green $+$: $x_\infty = 80$. Red circles : $x_\infty = 100$. The dashed line corresponds to the estimated decay rate (11).

It appears that machine precision imposes severe constraints on global mode computations for convective flows such as jets. The streamwise extent of the numerical domain must be sufficiently large to capture the amplitude maximum of the mode, but the amplitude variations must also be within the range of machine precision. At the same time, spurious modes contaminate an increasingly large portion of the spectrum as the numerical domain length is increased.

c. Spectrum of the turbulent mean flow

One would expect that for the turbulent mean flow profile the local spatial stability will dominate over the effect of the advection as shear is less important downstream of the potential core. However, as the advection velocity is also lower it tends to increase the spatial growth rate due to the advection of stable structures. This spatial growth is not compensated by the local spatial stability of the bell-shaped profiles. The estimate for the decay rate of spurious structures given by (11) can be modified to account for the significant variation of the base velocity on the jet axis, giving

$$\sigma' \equiv \log(\epsilon_m) \left(\int_0^{x_\infty} \frac{1}{u_x^0(0,x)} \, \mathrm{d}x \right)^{-1} . \tag{12}$$

The spectra displayed in figure 10 show that this estimate is also reasonably accurate. This implies an even more stringent constraint on the size of the computational domain than in the case of a nearly parallel flow.

Figure 11 displays selected global modes computed for $x_\infty = 60$: as for all the modes presented in figure 10, the exponential growth continues throughout the computational domain. Indeed, in light of the discussion of the model problems, there is no guarantee that a maximum will ever be reached: the maximum amplitude may well continue towards infinity. Consequently, even though the model base flow is more suitable for describing the transient dynamics of perturbations than the laminar flow, it neither allows computing global modes.

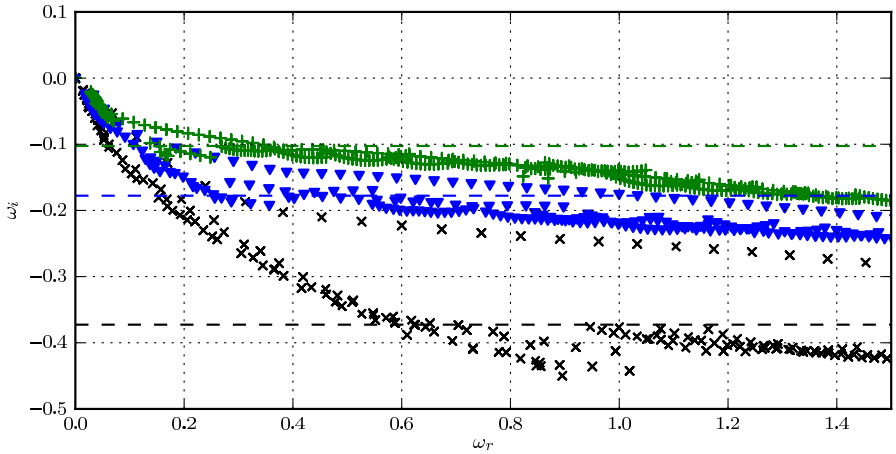

FIG. 10. Global spectra computed for $m = 0$ for the model base flow. Black $\times$: $x_\infty = 40$. Blue triangles : $x_\infty = 60$. Green $+$: $x_\infty = 80$. The dashed line corresponds to the estimated decay rate of the spurious branch given by (11).

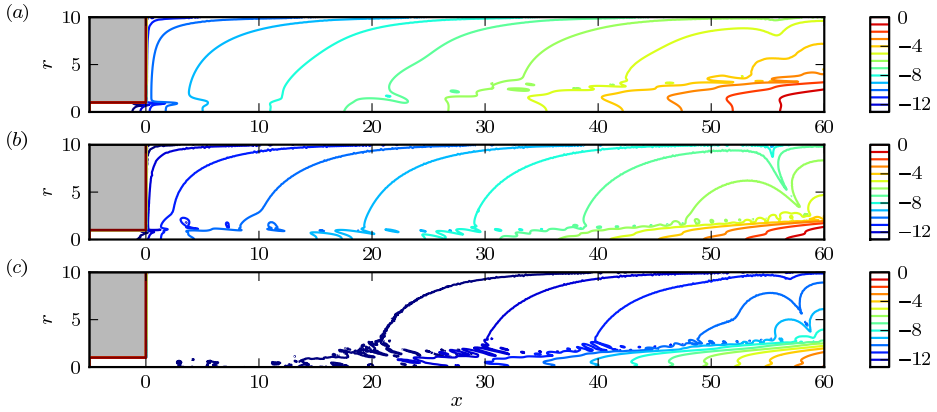

FIG. 11. Axial velocity fields of selected global modes computed for $m = 0$ for the model base flow with $x_\infty = 60$ and stress-free outflow boundary conditions (logarithmic scale). (a) : $\omega = 0.22-0.11\mathrm{i}$, (b) : $\omega = 1.0 - 0.17\mathrm{i}$, (c) : $\omega = 0.98 - 0.23\mathrm{i}$.

B. Compressible eigenmodes

Eigenmodes have been computed for the model mean flow at Ma = 0.75. The computed spectrum is displayed in figure 12(a). Similar to the incompressible case, it is worth pointing out that the spectrum does not show any preferred frequency. The decay rates of the modes are however significantly less stable than in the incompressible case, by more than a factor of five. Although the solver used for this computation is less accurate than the one used for incompressible computations, the results displayed in figure 12 are converged with respect to the iterative eigenvalue solver. As a consequence of the very low decay rate, the spatial growth of eigenmodes is weaker than in the incompressible case, and at high frequencies the global modes decay right after the end of the jet pipe (see figure 12(b, c, d))

Several reasons may explain such a slow temporal decay. As it was seen in § IV, acoustic

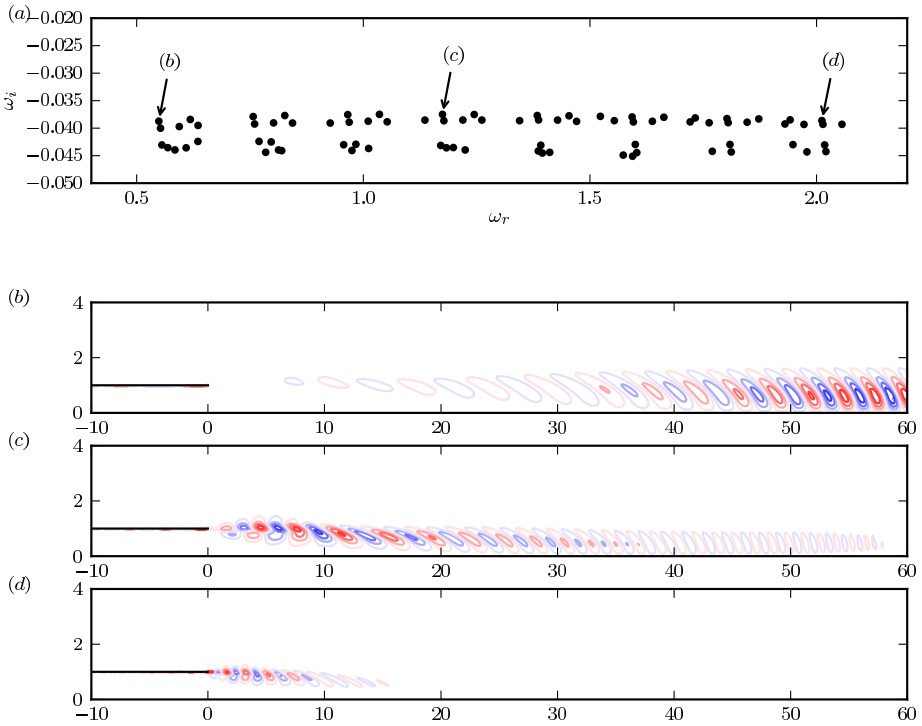

FIG. 12. Global modes computed for $m = 0$ on the model subsonic jet at Ma $= 0.75$. (a): eigenvalue spectrum. (b, c, d): azimuthal vorticity of three selected modes, as indicated in (a).

disturbances efficiently excite vortical structures, and, as the Mach number increases, the acoustic wavelength gets closer to the wavelength of vortical wavetrains, so that excitation can be efficient and lead to a feedback loop. The feedback could also be spurious: indeed, although the optimal perturbation results of § IV are quite insensitive to the treatment of the outer boundaries, this significantly affects the eigenmodes. In spite of the use of non-reflecting boundary conditions and very weak sponge regions, it is expected that an effect is still present here. Similarly, as the vorticity field grows in space due to the temporal stability, the acoustic field also grows exponentially with the distance to the acoustic sources. As a consequence, even for weakly damped modes, reflection can be significant in large numerical domains. Finally, the low decay rate may be related to the fact that the numerical dissipation is lower with the present FD formulation than with the FEM discretization used for incompressible flows. Indeed, in situations where structures are convected outside of the numerical domain, dissipative effects can be important at large times.

VI. PROJECTION OF THE TRANSIENT DYNAMICS ONTO THE SPACE SPANNED BY EIGENMODES.

Optimal perturbations have been computed in § IV using a direct-adjoint technique. An alternative method is to approximate the propagator using a reduced-order basis consisting of the computed eigenmodes. This technique has, for example, been successfully used by Akervik *et al*[7] for the global analysis of an amplifier flow. Regardless of the relevance of the eigenmodes to describe the dynamics, such an analysis is expected to yield accurate results provided the eigenmodes are computed accurately. Figure 13 displays the optimal gains computed for the laminar incompressible jet with $m = 0$: the N least stable eigenmodes

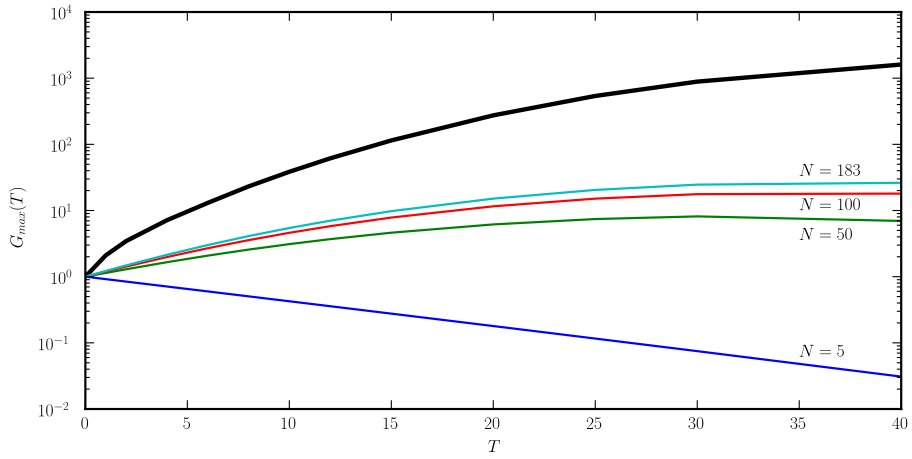

FIG. 13. Optimal transient amplification of axisymmetric perturbations for the laminar incompressible jet. Thick line: computation using the adjoint equations, as computed in § IV. Thin lines: optimal gains computed by projecting the dynamics onto the space spanned by the N least stable eigenmodes.

have been used for the computation, with N varying from 5 to 183[62]. It appears that even when all the computed eigenmodes are taken into account, the optimal gains are under-estimated by up to two orders of magnitude. Eigenmodes are therefore not relevant individually, which is already well known for amplifier flows, but also as a superposition to represent transient dynamics. A similar study on a stable lid-driven cavity flow (not shown here) yielded substantially better convergence towards transient energy gains when the number of included eigenmodes was increased. This further emphasized the role of advection in the representation of transient phenomena by global modes. The above finding is contrary to that of Akervik *et al*[7] and it is related to the much stronger streamwise growth of eigenmodes in the present configuration. Indeed the optimal initial conditions consist of structures in the jet pipe. In this region, all eigenmodes have very small amplitudes and numerical inaccuracies (due to both the eigenmode computation and the projection) become significant.

VII. CONCLUSIONS

The linear dynamics of perturbations in jet flows is the result of two mechanisms, advection by the base flows and shear layer instability. In order to investigate the effect of these two features on the modal and non-modal stability properties of the flow, two types of base flows have been considered. The first one is a laminar steady solution of the Navier–Stokes equation, for which both advection and instability remain approximately constant in the streamwise direction. A turbulent mean flow has also been used: in this case, instability is limited to a region of about eight radii downstream of the jet pipe, referred to as the potential core, where advection remains approximately constant. Further downstream the base flow velocity decreases significantly and the jet profiles become stable to axisymmetric perturbations.

An optimal perturbation analysis has been performed on these two base flows, revealing that vortical structures are amplified throughout the laminar jet, but only in the potential core for turbulent mean flows. In both cases the flow is globally stable.

Based on model problems reproducing the advection and instability properties of jet flows, it has been shown that problems arise when studying such flows within a modal

framework. Indeed, when eigenmodes represent the advection of stable, temporally decaying structures, they grow exponentially in the streamwise direction. When computing such modes, difficulties therefore arise due to the domain truncation, the modeling of outflow boundary conditions and the finite precision of computer arithmetic.

Eigenmodes have been computed for jets in laminar and turbulent, compressible and incompressible settings, and results display the same properties as those obtained from the model problems. It has been shown that convergence of the spectrum of incompressible jets is inhibited by the presence of spurious pseudomodes which impose strict constraints on the size of the numerical domain.

As was shown with simple models, the exponential spatial growth of the stable modes is not an indication of a local spatial instability, it is merely a reflection of the fact that the eigenfrequency ω has a negative imaginary part. This has been further exemplified through the computation of eigenmodes for turbulent mean flows that grow even faster than those computed for a laminar base flow while the flow is stable downstream of the potential core for $m = 0$. The temporally stable structures observed in the modes, generated by a shear layer instability downstream of the nozzle, are convected downstream in a quasi-neutral flow resulting in an apparent spatial growth. For both mean flows the global decay rates of shear layer modes are of the same order of magnitude since the inflow shear layer thickness is similar. As the advection velocity is much smaller for the turbulent mean flow, the spatial growth is therefore larger.

For compressible flows, the computed eigenmodes are less stable than in the incompressible case. As a consequence, the local stability of shear layer structures dominates over the growth due to stable advection such that the exponential growth is not observed. However, this growth not only affects vortical structures but also acoustic waves. For acoustic perturbations the exponential growth due to the advection of stable structures eventually dominates over the algebraic decay: the acoustic waves radiated from a mode reach their maximum amplitude at the boundaries of the computational domain, which represents considerable challenges to avoid spurious reflections.

The present results found for jet flows are consistent with the literature on the stability of the Blasius boundary layer. The qualitative features of the eigenmodes are similar for both configurations, but the physical settings are quite different and eigenmodes are much less temporally stable for the boundary layer problem. Consequently, the spatial growth of the modes is weaker and numerical issues are less important in the latter case.

All the numerical challenges faced in the modal analysis of jet flows cannot be attributed to a poor discretization and other numerical influence, since the numerical tools used in this study provided robust results for the transient flow analysis. As the numerical schemes employed for this study are linear, the transient simulations can be viewed as a superposition of all eigenmodes of the discrete problem. The issues are not related to the convective nature of the flow, since the transient analysis successfully and robustly reproduced the flow behavior; they rather lie with the description of stable convective dynamics by global modes, and their interpretation as coherent invariant structures.

ACKNOWLEDGMENTS

This work was supported by DGA grant number 2009.60.034.00.470.75.01 and by a fellowship from the EADS Foundation. Calculations were performed using HPC resources from GENCI (Grant 2012-026451). The authors thank F. Gallaire for his help.

[1]D. Barkley, "Linear analysis of the cylinder wake mean flow," Europhysics Letters **75**, 750–756 (2006).
[2]S. Bagheri, P. Schlatter, P. Schmid, and D. Henningson, "Global stability of a jet in crossflow," Journal of Fluid Mechanics **624**, 33 (2009).
[3]U. Ehrenstein and F. Gallaire, "Two-dimensional global low-frequency oscillations in a separating boundary-layer flow," Journal of Fluid Mechanics **614**, 315 (2008).
[4]P. Meliga, J. Chomaz, and D. Sipp, "Global mode interaction and pattern selection in the wake of a disk: a weakly nonlinear expansion," Journal of Fluid Mechanics **633**, 159 (2009).
[5]M. Navarro, L. Witkowski, L. Tuckerman, and P. L. Qur, "Building a reduced model for nonlinear dynamics in Rayleigh-Bnard convection with counter-rotating disks," Physical Review E **81** (2010).

[6]O. Marquet, D. Sipp, and L. Jacquin, "Sensitivity analysis and passive control of cylinder flow," Journal of Fluid Mechanics **615**, 221–252 (2008).
[7]E. Akervik, J. Hpffner, U. Ehrenstein, and D. Henningson, "Optimal growth, model reduction and control in a separated boundary-layer flow using global eigenmodes," Journal of Fluid Mechanics **579**, 305 (2007).
[8]A. Barbagallo, D. Sipp, and P. Schmid, "Inputoutput measures for model reduction and closed-loop control: application to global modes," Journal of Fluid Mechanics **685**, 23–53 (2011).
[9]P. Huerre and P. Monkewitz, "Local and global instabilities in spatially developing flows," Annual Review of Fluid Mechanics **22**, 473–537 (1990).
[10]J. Chomaz, "Global instabilities in spatially developing flows: Non-Normality and nonlinearity," Annual Review of Fluid Mechanics **37**, 357–392 (2005).
[11]L. Lesshafft, P. Huerre, P. Sagaut, and M. Terracol, "Nonlinear global modes in hot jets," Journal of Fluid Mechanics **554**, 393–409 (2006).
[12]L. Lesshafft, *Global modes and aerodynamic sound radiation in self-excited hot jets*, PhD thesis, Ecole Polytechnique (2007).
[13]S. Crow and F. Champagne, "Orderly structure in jet turbulence," Journal of Fluid Mechanics **48**, 547 (1971).
[14]D. Bodony and S. Lele, "On using large-eddy simulation for the prediction of noise from cold and heated turbulent jets," Physics of Fluids **17**, 085103 (2005).
[15]A. Cooper and D. Crighton, "Global modes and superdirective acoustic radiation in low-speed axisymmetric jets," European Journal of Mechanics - B/Fluids **19**, 559–574 (2000).
[16]C. Moore, "The role of shear-layer instability waves in jet exhaust noise," Journal of Fluid Mechanics **80**, 321 (1977).
[17]J. Nichols and S. Lele, "Non-normal global modes of high-speed jets," International Journal of Spray and Combustion Dynamics **3**, 285–302 (2011).
[18]J. Nichols and S. Lele, "Global mode analysis of turbulent high-speed jets," Annual Research Briefs 2010 (Center for Turbulence Research, 2010).
[19]D. Barkley, M. Gomes, and R. Henderson, "Three-dimensional instability in flow over a backward-facing step," Journal of Fluid Mechanics **473** (2002).
[20]O. Tammisola, *Linear stability of plane wakes and liquid jets: global and local approach*, PhD thesis, KTH (2009).
[21]O. Tammisola, F. Lundell, and L. Soderberg, "Effect of surface tension on global modes of confined wake flows," Physics of Fluids **23**, 014108 (2011).
[22]U. Ehrenstein and F. Gallaire, "On two-dimensional temporal modes in spatially evolving open flows: the flat-plate boundary layer," Journal of Fluid Mechanics **536**, 209–218 (2005).
[23]C. Heaton, J. Nichols, and P. Schmid, "Global linear stability of the non-parallel batchelor vortex," Journal of Fluid Mechanics **629**, 139 (2009).
[24]L. Trefethen, A. Trefethen, S. Reddy, and T. Driscoll, "Hydrodynamic stability without eigenvalues," Science **261**, 578–584 (1993).
[25]P. Schmid, "Nonmodal stability theory," Annual Review of Fluid Mechanics **39**, 129–162 (2007).
[26]E. Akervik, U. Ehrenstein, F. Gallaire, and D. Henningson, "Global two-dimensional stability measures of the flat plate boundary-layer flow," European Journal of Mechanics - B/Fluids **27**, 501–513 (2008).
[27]B. Farrell and A. Moore, "An adjoint method for obtaining the most rapidly growing perturbation to oceanic flows," Journal of Physical Oceanography **22**, 338–349 (1992).
[28]K. Butler and B. Farrell, "Three-dimensional optimal perturbations in viscous shear flow," Physics of Fluids A: Fluid Dynamics **4**, 1637 (1992).
[29]S. Reddy and L. Trefethen, "Pseudospectra of the Convection-Diffusion operator," SIAM Journal on Applied Mathematics **54**, 1634 (1994).
[30]C. Cossu and J. Chomaz, "Global measures of local convective instabilities," Physical Review Letters **78**, 4387–4390 (1997).
[31]P. Huerre and P. Monkewitz, "Absolute and convective instabilities in free shear layers," Journal of Fluid Mechanics **159**, 151–168 (1985).
[32]S. Reddy and D. Henningson, "Energy growth in viscous channel flows," Journal of Fluid Mechanics **252**, 209–238 (1993).
[33]E. Dick, "Introduction to finite element methods in computational fluid dynamics," in *Computational fluid dynamics: an introduction* (Springer, 2009) 3rd ed.
[34]T. Matsushima and P. Marcus, "A spectral method for polar coordinates," Journal of Computational Physics **120**, 365–374 (1995).
[35]C. Bogey and C. Bailly, "Three-dimensional non-reflective boundary conditions for acoustic simulations: far field formulation and validation test cases," Acta Acustica **88**, 463–471 (2002).
[36]P. Monkewitz and K. Sohn, "Absolute instability in hot jets," AIAA Journal **26**, 911–916 (1988).
[37]X. Garnaud, L. Lesshafft, and P. Huerre, "Global linear stability of a model subsonic jet," AIAA paper 2011-3608 (2011).
[38]W. Reynolds and A. Hussain, "The mechanics of an organized wave in turbulent shear flow. part 3. theoretical models and comparisons with experiments," Journal of Fluid Mechanics **54**, 263 (1972).
[39]V. Kitsios, L. Cordier, J. Bonnet, A. Ooi, and J. Soria, "Development of a nonlinear eddy-viscosity closure for the triple-decomposition stability analysis of a turbulent channel," Journal of Fluid Mechanics **664**, 74–107 (2010).

[40]J. Crouch, A. Garbaruk, and D. Magidov, "Predicting the onset of flow unsteadiness based on global instability," Journal of Computational Physics **224**, 924–940 (2007).
[41]D. Crighton and M. Gaster, "Stability of slowly diverging jet flow," Journal of Fluid Mechanics **77**, 397 (1976).
[42]K. Gudmundsson and T. Colonius, "Instability wave models for the near-field fluctuations of turbulent jets," Journal of Fluid Mechanics **689**, 97–128 (2011).
[43]F. Hecht, "Freefem++ manual, third edition, version 3.16-1," Tech. Rep. (2011) available at http://www.freefem.org/ff++.
[44]P. Amestoy, I. Duff, and J. L'Excellent, "Multifrontal parallel distributed symmetric and unsymmetric solvers," Computational Methods in Applied Mathematics **184**, 501–520 (2000).
[45]S. Balay, K. Buschelman, V. Eijkhout, W. Gropp, D. Kaushik, M. Knepley, L. C. McInnes, B. Smith, and H. Zhang, "PETSc users manual," Tech. Rep. ANL-95/11 - Revision 3.0.0 (Argonne National Laboratory, 2008) available at http://www.mcs.anl.gov/petsc/petsc-as/.
[46]V. Hernandez, J. Roman, and V. Vidal, "SLEPc: a scalable and flexible toolkit for the solution of eigenvalue problems," ACM Transactions on Mathematical Software **31**, 351362 (2005).
[47]R. Lehoucq, D. Sorensen, and C. Yang, *ARPACK Users' Guide: Solution of Large-Scale Eigenvalue Problems with Implicitly Restarted Arnoldi Methods* (SIAM, 1998).
[48]C. Bogey and C. Bailly, "A family of low dispersive and low dissipative explicit schemes for flow and noise computations," Journal of Computational Physics **194**, 194–214 (2004).
[49]C. Mack and P. Schmid, "A preconditioned krylov technique for global hydrodynamic stability analysis of large-scale compressible flows," Journal of Computational Physics **229**, 541–560 (2010).
[50]X. Garnaud, *Modes, transient dynamics and forced response of circular jets*, PhD thesis, Ecole Polytechnique (2012).
[51]M. F. de Pando, D. Sipp, and P. Schmid, "Efficient evaluation of the direct and adjoint linearized dynamics from compressible flow solvers." submitted to Journal of Computational Physics (2012).
[52]A. Hanifi, P. Schmid, and D. Henningson, "Transient growth in compressible boundary layer flow," Physics of Fluids **8**, 826–837 (1996).
[53]A. Michalke, "Survey on jet instability theory," Progress in Aerospace Science **21**, 159–199 (1984).
[54]M. Landahl, "A note on an algebraic instability of inviscid parallel shear flows," Journal of Fluid Mechanics **98**, 243 (1980).
[55]D. Jones and J. Morgan, "The instability of a vortex sheet on a subsonic stream under acoustic radiation," Mathematical Proceedings of the Cambridge Philosophical Society **72**, 465 (1972).
[56]D. Crighton and F. Leppington, "Radiation properties of the semi-infinite vortex sheet: the initial-value problem," Journal of Fluid Mechanics **64**, 393 (1974).
[57]M. Barone and S. Lele, "Receptivity of the compressible mixing layer," Journal of Fluid Mechanics **540**, 301–335 (2005).
[58]L. Lesshafft, P. Huerre, and P. Sagaut, "Aerodynamic sound generation by global modes in hot jets," Journal of Fluid Mechanics **647**, 473–489 (2010).
[59]P. Schmid and D. Henningson, *Stability and Transition in Shear Flows* (Springer, 2001).
[60]I. Orlanski, "A simple boundary condition for unbounded hyperbolic flows," Journal of Computational Physics **21**, 251–269 (1976).
[61]W. Criminale, T. Jackson, and R. Joslin, *Theory and computation of hydrodynamic stability* (Cambridge University Press, 2003).
[62]For $m = 0$ the linearized Navier–Stokes operator is real, so only eigenvalues with $\omega_r \geq 0$ need to be considered.

Chapter 6

Optimal forcing of incompressible jets

6.1 Introduction

The previous chapter showed that a modal approach fails to describe the dynamics of perturbations observed in isothermal jets due to the amplifier nature of the flow, and due to the fact that downstream of the instability region structures are advected in a flow which is close to neutrally stable[1]. Studying the optimal perturbation, i.e. the structures that are most amplified over a time horizon T, provided some insight into the instability mechanisms at play in a strongly non-parallel jet. In most situations, optimal initial conditions consist of upstream tilted structures in the boundary layer at the end of the jet pipe: perturbations are first amplified through the Orr mechanism in the boundary layer, and continue being amplified throughout the potential core via a shear layer instability. Further downstream perturbations with azimuthal wave-numbers $m \neq 0$ can continue to slowly grow.

In order to relate the optimal disturbances obtained from such an analysis to the structures actually seen in flows two questions should be answered: can these structures be present in the flow in the first place, and is the amplification very sensitive to the exact shape of the initial disturbance. The second question can be answered through the distribution of the singular values of the propagation operator: the larger the ratio between the first two singular values is the most likely the optimal response will be observed with a random initial condition. This ratio is generally large. Ehrenstein and Gallaire (2005) showed that for the flat plate boundary layer the initial

[1] in a local approach, velocity profiles are weakly stable or unstable depending on the azimuthal wave number m.

amplification due to the Orr mechanism is sensitive (it is in particular poorly represented on a truncated eigenmode basis), but the later growth is not. In order to answer the first question, one should know where disturbances come from.

Optimal perturbations can be viewed as a forcing distributed in space but a Dirac in time. In this chapter the forcing is no longer assumed to be a Dirac in time but an exponential, i.e. Fourier components of a general forcing are considered. The results of this type of analysis can be viewed in the context of flows disturbed by a low level random incoming noise, or in the context of flows excited by a controlled forcing. Crow and Champagne (1971) excited turbulent jets with a loud speaker of adjustable frequency, and measured the velocity fluctuations on the jet axis. The amplification of the forcing is displayed in figure 6.1 for different frequencies: the authors report that the relevant scaling of the frequency of large scale structures is the Strouhal number based on the jet diameter, and that this is fairly independent of the inflow conditions. The structures observed for a Strouhal number of 0.3 (displayed in figure 4.1) are referred to as the jet *preferred mode*. The purpose of this chapter is to describe such structures. Different procedures to characterize the response of a flow to external forcing are briefly mentioned below.

Signaling problem The response of a parallel flow to a harmonic forcing localized in the streamwise direction is described for example by Huerre and Monkewitz (1985), Gordillo and Perez-Saborid (2002). For convectively unstable flows and within the range of unstable frequencies a periodic forcing generates spatially growing waves. Their structure is given by the solution of the spatial instability problem. For slices of the mean turbulent flow, the spatial instability features were represented in figure 5.3. They depend strongly on the axial position x. For $x \leq 8$ frequencies in the range $0 \leq \omega \leq \omega_{max}(x)$ are amplified, and both $\omega_{max}(x)$ and the maximum spatial growth rate decrease approximately linearly with x. For $x \geq 8$ the mean flow is locally stable.

The most amplified frequency scales with the Strouhal number based on the momentum thickness at the end of the jet pipe, and therefore does not correspond to the frequency of the preferred mode, suggesting that non-parallel effects play a dominant role in the frequency selection.

WKB analysis of weakly non-parallel flows The parallel flow approach can be extended to weakly non-parallel flow through a WKB approximation. In this framework it is assumed that information propagates only down-

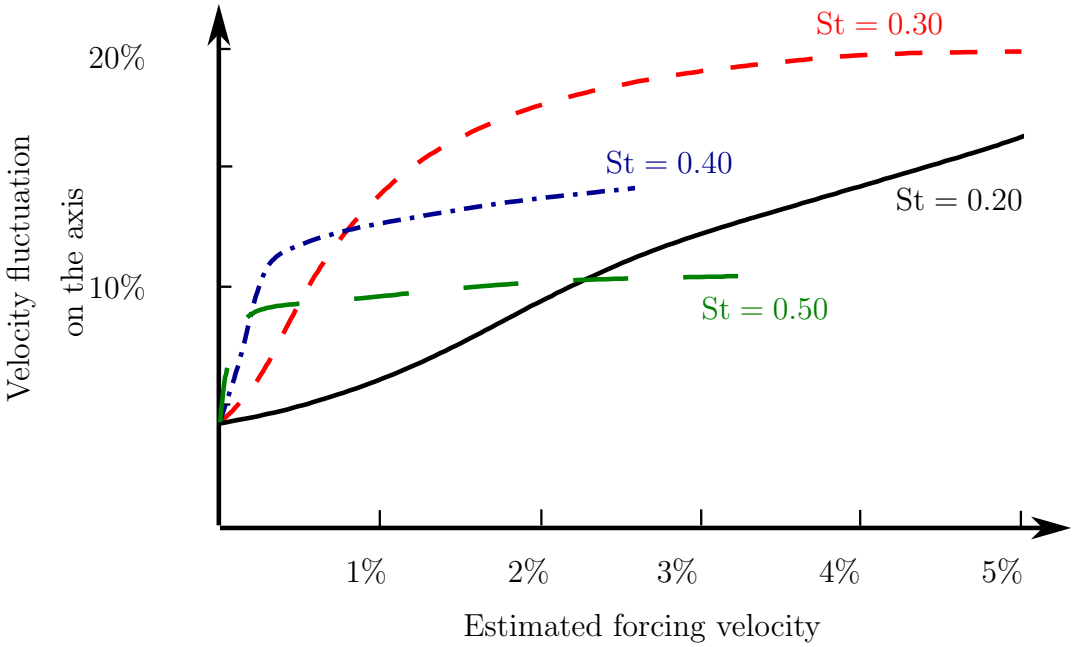

Figure 6.1: Velocity fluctuations on the jet axis in a turbulent jet triggered by a speaker. The Strouhal number of the perturbations based on the jet diameter is indicated next to the curves. Data taken from Crow and Champagne (1971). A visualization of the structures corresponding to the *preferred mode* is given in figure 4.1.

stream, and that at each location x the perturbation velocity and pressure profiles are those of the k^+ spatial branch. Such an analysis has been performed by Crighton and Gaster (1976). As shown in figure 6.2 their results are in reasonable agreement with the experimental data of Crow and Champagne (1971) in the near nozzle region.

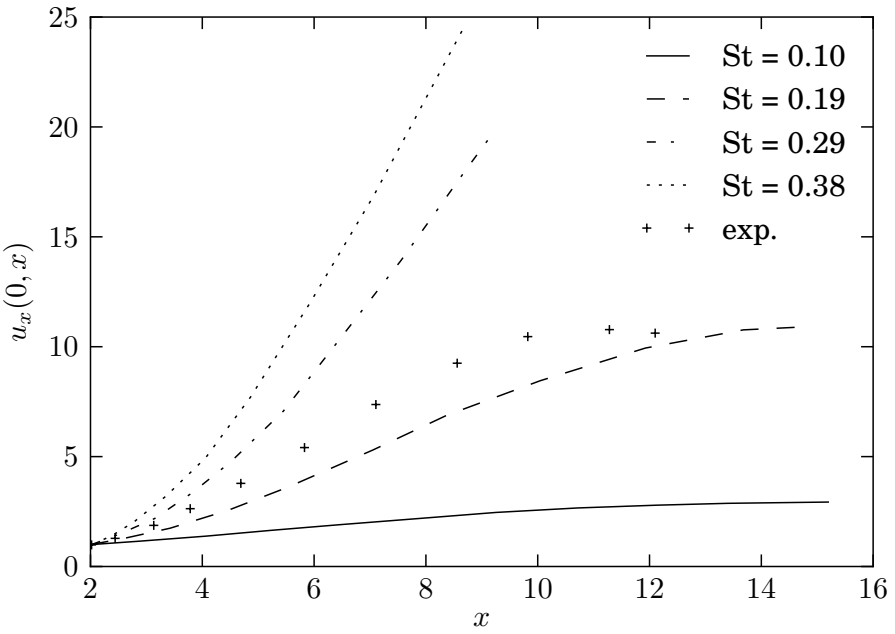

Figure 6.2: Gain in centre-line axial velocity fluctuation: comparison between WKB results and experimental measurements by Crow and Champagne (1971) for a jet forced at $St = 0.3$ (Data taken from Crighton and Gaster (1976)).

PSE analysis of weakly non-parallel flows The WKB approximation can be generalized so that the perturbation distribution in the radial direction is no longer given by the spatial instability modes. In the Parabolized Stability Equation framework, the perturbation distribution along r has to be prescribed at the inflow, and is then solved for increasing x. This approach has been applied to jet flows in particular by Gudmundsson and Colonius (2009), Rodriguez et al. (2011) to describe the development of shear layer structures and their acoustic radiation. Figure 6.3 displays a comparison

of PSE results with experimental data obtained from an natural (unforced) turbulent jet: the increase of the centerline velocity fluctuations within the potential core is accurately predicted using this approach for Strouhal numbers $St \geq 0.3$.

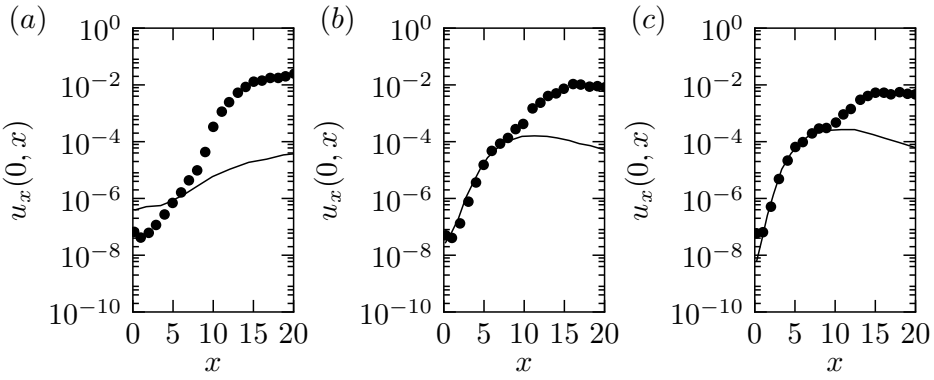

Figure 6.3: Gain in centre-line axial velocity fluctuation: comparison between PSE results and experimental measurements by Crow and Champagne (1971) for a natural jet (Data taken from Rodriguez et al. (2011)). (a): $St = 0.1$, (b): $St = 0.3$, (c): $St = 0.5$

Receptivity study: optimal forcing In both the WKB and PSE approaches, the shape of the disturbance at the inflow is imposed together with the frequency, and the downstream development of the instability structures is solved for.

The receptivity of a flow to external disturbances can be studied in terms of the resolvent $R(\omega) = (L - \mathrm{i}\omega\mathrm{Id})^{-1}$ for $\omega \in \mathbb{R}$ [2]. The norm of the resolvent $\mathcal{R}(\omega) = \|R(\omega)\|$ gives the maximum amplification of a time harmonic forcing at the frequency ω (Trefethen et al. 1993). The corresponding optimal forcing corresponds to the leading singular vector of $R(\omega)$.

For one dimensional discretization, an SVD of the resolvent operator can be performed to compute the optimal forcing (see e.g. Cossu and Chomaz (1997), Reddy and Trefethen (1994) for 1D PDEs and Trefethen et al. (1993), Schmid (2007), Hwang and Cossu (2010) for local flow problems). A local analysis however cannot be used to explain the pseudo-resonance of jet flows

[2] This formalism is very close to that of the pseudo-spectrum mentioned in the previous chapter to explain the impossibility to compute eigenmodes in some flow configurations (Trefethen and Embree 2005). In this case, complex values of ω are considered.

since non-parallel effects are dominant, but this analysis applies in the way to two dimensional problems (the only problem being the computational cost)

Optimal forcing in a "global" framework Considering the resolvent operator for a two dimensional discretization, one can find the forcing at a given frequency that generates the largest time harmonic response. This has been done by Marquet and Sipp (2010) for the flow over a backward facing step and by Monokrousos et al. (2010) for the flat plate boundary layer.[3]

Stochastic forcing Time harmonic forcing is appropriate to describe forced experiments such as those of Crow and Champagne (1971), but less so to study the case of a natural jet as in Rodriguez et al. (2011). In such cases, one can consider the forcing to be a stochastic Gaussian white noise. This situation has been studied by Farrell and Ioannou (1993) for parallel Couette and Poiseuille flows. In this approach, the solution procedure to characterize the variance of the flow fluctuations involves the solution of a Lyapounov equation. For one dimensional discretizations, this can be solved by using dense linear algebra but this procedure would be untractable for 2D or 3D problems. Methods are being developed for such problems, but this remains a very complicated task (Nong and Sorensen 2009).

6.2 Paper: *The preferred mode of incompressible jets*

The following paper presents the application of the receptivity formalism to the incompressible jet.

[3]This has also been examined by Nichols and Lele (2010) who present results for the pseudo-spectrum of laminar supersonic flows. These authors compute the resolvent norm using a projection of the linearized Navier–Stokes equations on the space spanned by some of the least stable eigenmodes.

Under consideration for publication in J. Fluid Mech. 1

The preferred mode of incompressible jets: linear frequency response analysis

X. GARNAUD, L. LESSHAFFT, P.J. SCHMID AND P. HUERRE

Laboratoire d'Hydrodynamique (LadHyX), Ecole Polytechnique – CNRS, 91128 Palaiseau, France

(Received 27 September 2012)

The linear amplification of axisymmetric external forcing in incompressible jet flows is investigated within a fully non-parallel framework. Experimental and numerical studies have shown that isothermal jets preferably amplify external perturbations for Strouhal numbers in the range $0.25 \leq St_D \leq 0.5$, depending on the operating conditions. In the present study, the optimal forcing of an incompressible jet is computed as a function of the excitation frequency. This analysis characterizes the preferred amplification as a pseudo-resonance with a dominant Strouhal number of around 0.45. The flow response at this frequency takes the form of a vortical wave-packet that peaks inside the potential core. Its global structure is characterized by the cooperation of local shear-layer and jet-column modes.

1. Introduction

Large-scale coherent structures develop in the shear layers of isothermal jet flows, for both laminar and turbulent regimes. These structures are not self-sustained, but are the consequence of strong amplification of incoming disturbances. Crow & Champagne (1971) performed experiments where the flow was forced with a controlled frequency; they showed that optimal excitation is achieved for a Strouhal number based on the jet diameter of about 0.3. The corresponding flow perturbations, referred to as the jet *preferred mode*, grow in amplitude starting at the nozzle until they undergo non-linear saturation.

A local analysis of jets (Michalke 1984) identifies shear layer perturbations immediately downstream of the nozzle as the fastest growing instability modes, which would indicate that the preferred frequency scales with the initial shear layer thickness. This also suggests that the mechanisms underlying the selection of the preferred frequency depend on the downstream flow development. Under the assumption of a slowly diverging base flow, Crighton & Gaster (1976) used a WKBJ approximation to describe the spatial development of the instability wave. Their results are in reasonable agreement with the experimental results of Crow & Champagne (1971) for the initial growth of the structures. This approach has subsequently been generalized through the use of the Parabolized Stability Equations (Ray *et al.* 2009; Gudmundsson & Colonius 2011; Rodriguez *et al.* 2011). While this approach also relies on the assumption of a slow variation of the base flow in the streamwise direction, these results were found to yield good agreement with experiments of natural turbulent jets.

The optimal disturbance of flows subjected to time-harmonic linear perturbations has been described by Trefethen *et al.* (1993). This method has first been applied to general non-parallel configurations using a projection of the flow dynamics onto a reduced space spanned by a set of eigenmodes (Alizard *et al.* 2009; Nichols & Lele 2010). In other studies

(Monokrousos *et al.* 2010; Marquet & Sipp 2010; Nichols & Lele 2011*b*; Sipp & Marquet 2012) the resolvent norm has been computed directly from the linearized Navier–Stokes operator, such that the entire non-normal flow behavior captured by the discretization is taken into account in the results. This approach is followed here to provide a better understanding of the preferred frequency selection and the associated spatial structures; in particular, the non-parallel nature of the flow, as well as the effects of a solid circular jet-pipe, are taken into account. The present analysis is mainly restricted to axisymmetric forcing and perturbations. Results for helical forcing are only briefly discussed.

After a description of the flow under consideration in § 2, two different models of the external forcing are described in § 4, together with the numerical method used. The results, presented in § 5, are then discussed and compared to classical local stability analysis.

2. Flow configuration

2.1. *Geometry*

A cylindrical jet of an incompressible Newtonian fluid of viscosity ν^*, with radius R^* and exit centerline velocity U_0^* is considered. The latter two quantities are used to make lengths and velocities non-dimensional. Frequencies f^* can be non-dimensionalized to yield either a circular frequency ω or a Strouhal number St based on the jet diameter. These parameters are related via $St = \omega/\pi$. Throughout the study, the Reynolds number is taken as

$$Re = \frac{U_0^* R^*}{\nu^*} = 10^3.$$

The flow geometry, described in terms of the cylindrical coordinates r, θ and x, is represented in figure 1. The boundary of the computational domain Ω is decomposed into Γ_i, Γ_w,Γ_o and Γ_a, respectively corresponding to the inlet, a solid wall, the outlet and the jet axis. No-slip boundary conditions are imposed on Γ_w, and stress-free boundary conditions are used on Γ_o (Dick 2009). Compatibility conditions, ensuring the smoothness of the computed fields are imposed on the axis $r = 0$ (Matsushima & Marcus 1995). At the inflow, homogeneous or inhomogeneous Dirichlet boundary conditions are imposed on the velocity as requested by the problem under consideration.

Two unstructured meshes with identical dimensions but different resolution are used for the finite-element computations. The density of vertices in the domain is controlled by the distance between discretization points on the boundary of the computational domain as well as on interior boundaries (dashed lines in figure 1). This distance is denoted h_4 for boundaries in the far field ($r > r_3^+$). It is smaller than h_3 for $r \leq r_3^+$, and respectively smaller than h_2 and h_1 in the inner regions defined by $x \leq x_2^+$ and $1-\delta_2/2 \leq r \leq 1+\delta_2/2$ and by $x_1^- \leq x \leq x_1^+$ and $1 - \delta_1/2 \leq r \leq 1 + \delta_1/2$. These sub-domains are indicated by gray shaded areas in figure 1. The values of the h_i's for both meshes are given in figure 1.

2.2. *Base state*

Linear stability analysis formally applies to base states that are steady solutions of the governing equations. However, several studies have found that linearization around a time-averaged mean flow yields better predictions of the nonlinear flow behaviour, in particular with regard to the frequency selection of intrinsic oscillations (Pier 2002; Barkley 2006). The present study employs the mean-flow model proposed by Monkewitz & Sohn (1988) for a turbulent free jet, displayed in figure 2. This model consists of a potential core, starting from a momentum thickness $\theta = 0.043$, and extending over eight radii

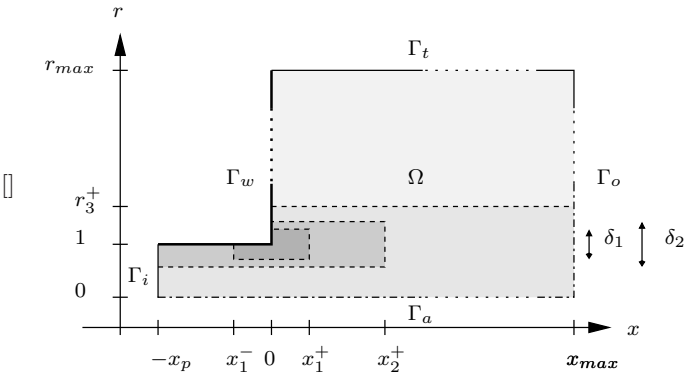

Mesh	#1	#2
h_1	0.035	0.01
h_2	0.035	0.035
h_3	0.07	0.05
h_4	0.2	0.2

FIGURE 1. Schematic representation of the numerical domain. The pipe length is set to $x_p = 5$, and it has been verified that setting $r_{max} = 10$ does not influence the results. Gray shaded areas correspond to subregions in which different grid resolutions are selected. Values of $x_1^- = -2$, $x_1^+ = 1$, $\delta_1 = 0.15$, $x_2^+ = 10$, $\delta_2 = 0.5$ and $r_3^+ = 2$ are used.

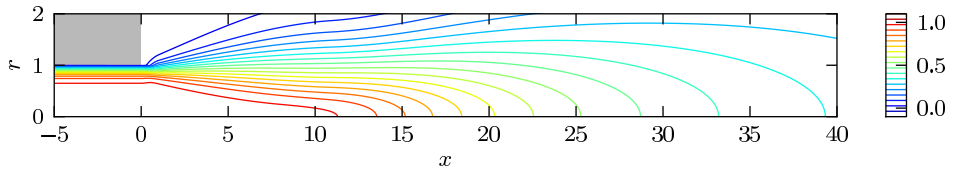

FIGURE 2. Axial velocity field for the model turbulent mean flow of Monkewitz & Sohn (1988).

downstream of the end of the jet pipe, followed by a self-similar region, where the velocity profiles have an approximately Gaussian shape. A parallel pipe flow region has been added upstream, and a smooth transition is made for $0 \leq x \leq 1$, as described in Garnaud *et al.* (2011).

In the following, infinitesimal perturbations around the steady mean flow are considered, such that the flow field can be written as $(\boldsymbol{u}, p) = (\boldsymbol{U} + \epsilon \boldsymbol{u}', P + \epsilon p')$, where $(\boldsymbol{U}, P)$ denotes the base state displayed in figure 2.

3. Modal analyis

Monkewitz (1989) and Huerre & Monkewitz (1990) conjectured that the preferred mode observed in experiments corresponds to the resonance of the least stable eigenmode of the jet with incoming disturbances. This issue has been investigated by Cooper & Crighton (2000) by means of a WKB approximation. Upon making the assumptions that (i) the global mode has the shape of a local shear-layer mode at each location and that (ii) the base flow development is slow, the authors found a weakly stable global mode at a Strouhal number of 0.44 which agrees well with experimental observations. In order to avoid such strong assumptions, eigenmodes can now be computed using the axisymmetric Navier–Stokes equations discretized on a two-dimensional domain. Such a modal analysis has for example been performed by Nichols & Lele (2011*a*) in the context of supersonic jets. This approach is followed in this section. Figure 3 displays the spectrum obtained

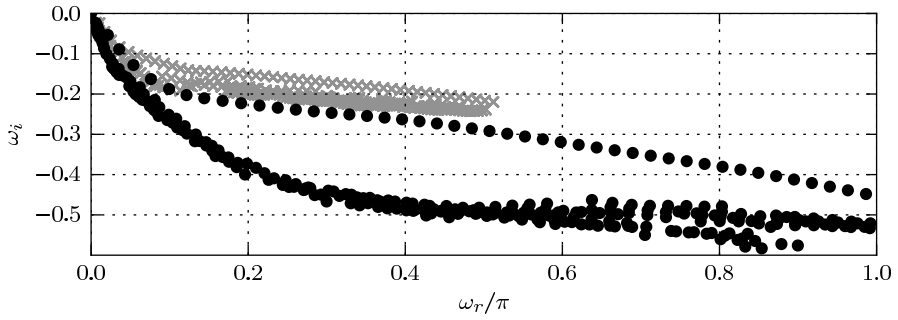

FIGURE 3. Eigenvalue spectra of the linearized Navier–Stokes equations ($L\boldsymbol{q} = \mathrm{i}\omega B\boldsymbol{q}$) computed for a domain of length $x_{max} = 40$ (black dots) and $x_{max} = 60$ (gray crosses).

for the global eigenvalue problem

$$\begin{aligned} \boldsymbol{\nabla}\cdot\boldsymbol{u}' &= 0, \\ -\mathrm{i}\omega\boldsymbol{u}' + (\boldsymbol{U}\cdot\boldsymbol{\nabla})\boldsymbol{u}' + (\boldsymbol{u}'\cdot\boldsymbol{\nabla})\boldsymbol{U} &= -\boldsymbol{\nabla}p' + \frac{1}{Re}\boldsymbol{\nabla}^2\boldsymbol{u}' + \psi(\boldsymbol{x})\boldsymbol{f}', \end{aligned} \tag{3.1}$$

with homogeneous Dirichlet boundary conditions on $\Gamma_i \cup \Gamma_w$. All eigenmodes are stable, and three families of modes can be identified. First, low-frequency free-stream modes (eigenvalues close to the origin) correspond to standing vortical structures. These decay very slowly due to viscous effects. Second, a branch of shear-layer / jet-column modes is observed (upper branch in figure 3). Along this branch the decay rate $-\omega_i$ increases with frequency ω_r, and the spatial structure of the eigenmodes is characterized by an exponential growth throughout the computational domain. This growth can be understood as a consequence of the stable advection of nearly neutral shear layer structures. Finally, the lower branch of eigenmodes in figure 3 corresponds in fact to pseudomodes that lie on the 10^{-10} contour of the pseudospectrum. Note that the actual spectrum is quite dependent on the size of the numerical domain, but that qualitative features are not. For more details, see Garnaud (2012).

The spectrum of the linearized Navier–Stokes equations therefore exhibits no isolated or least stable eigenmode that could explain the preferred mode through a resonance mechanism. In the next section, a pseudo-resonance analysis is carried out to investigate the origin of the preferred mode.

4. Response to harmonic forcing

4.1. *External forcing as a body force*

Following Monokrousos *et al.* (2010), Marquet & Sipp (2010) and Sipp & Marquet (2012), the external forcing can be modeled as a body force $\boldsymbol{f}(\boldsymbol{x}, t)$ acting on the momentum equation,

$$\frac{\partial\boldsymbol{u}}{\partial t} + (\boldsymbol{u}\cdot\boldsymbol{\nabla})\boldsymbol{u} = -\boldsymbol{\nabla}p + \frac{1}{Re}\boldsymbol{\nabla}^2\boldsymbol{u} + \psi(\boldsymbol{x})\boldsymbol{f},$$

while $\boldsymbol{\nabla}\cdot\boldsymbol{u} = 0$ is maintained throughout the flow. The weight function ψ is used to restrict the flow region where forcing is applied, and the forcing amplitude is assumed to be small: $\boldsymbol{f} = \epsilon\boldsymbol{f}'$. ~~Infinitesimal perturbations around the steady mean flow are considered, such that the flow field can be written as $(\boldsymbol{u}, p) = (\boldsymbol{U} + \epsilon\boldsymbol{u}', P + \epsilon p')$ and $\boldsymbol{f} = \epsilon\boldsymbol{f}'$, where $(\boldsymbol{U}, P)$ denotes the base state described in §~~. To leading order, the dynamics of

perturbations are governed by the linear system

$$\begin{aligned} \boldsymbol{\nabla}\cdot\boldsymbol{u}' &= 0, \\ \frac{\partial \boldsymbol{u}'}{\partial t} + (\boldsymbol{U}\cdot\boldsymbol{\nabla})\boldsymbol{u}' + (\boldsymbol{u}'\cdot\boldsymbol{\nabla})\boldsymbol{U} &= -\boldsymbol{\nabla}p' + \frac{1}{Re}\boldsymbol{\nabla}^2\boldsymbol{u}' + \psi(\boldsymbol{x})\boldsymbol{f}', \\ \boldsymbol{u}' &= 0, \qquad && \Gamma_i \cup \Gamma_w \\ \frac{1}{Re}\frac{\partial \boldsymbol{u}'}{\partial n} - p'\boldsymbol{n} &= 0. && \Gamma_t \cup \Gamma_o \end{aligned} \tag{4.1}$$

In a linear framework, all signals are decomposed in time into independent Fourier components. The forcing is therefore considered to be time-harmonic, $\boldsymbol{f}' = \widetilde{\boldsymbol{f}}\exp(-\mathrm{i}\omega t)$, prompting an asymptotic flow response $(\boldsymbol{u}', p') = (\widetilde{\boldsymbol{u}}, \widetilde{p})\exp(-\mathrm{i}\omega t)$ at the same frequency. The amplification of the externally applied forcing at a given frequency ω is measured in terms of the gain

$$G^{bf}_{opt}(\omega) = \max_{\widetilde{\boldsymbol{f}}} \left(\int_\Omega |\widetilde{\boldsymbol{u}}|^2 r \,\mathrm{d}r\,\mathrm{d}x\right) \Big/ \left(\int_\Omega |\widetilde{\boldsymbol{f}}|^2 r \,\mathrm{d}r\,\mathrm{d}x\right). \tag{4.2}$$

The optimal forcing $\widetilde{\boldsymbol{f}}_{opt}(\omega)$ realizes this maximum. For the results presented in §5.1, the forcing is assumed to be localized inside the pipe only, i.e. the weight function is defined as $\psi(\boldsymbol{x}) = 1$ for $x < 0$ and $\psi(\boldsymbol{x}) = 0$ for $x \geq 0$.

4.2. *External forcing as an inflow condition*

Rather than forcing the jet through a distributed body force in the pipe interior as in the previous section, one may model incoming perturbations in the form of an unsteady upstream boundary condition of the linearized Navier–Stokes equations:

$$\begin{aligned} \boldsymbol{\nabla}\cdot\boldsymbol{u}' &= 0, \\ \frac{\partial \boldsymbol{u}'}{\partial t} + (\boldsymbol{U}\cdot\boldsymbol{\nabla})\boldsymbol{u}' + (\boldsymbol{u}'\cdot\boldsymbol{\nabla})\boldsymbol{U} &= -\boldsymbol{\nabla}p' + \frac{1}{Re}\boldsymbol{\nabla}^2\boldsymbol{u}', \\ \boldsymbol{u}' &= 0, && \Gamma_w \\ \frac{1}{Re}\frac{\partial \boldsymbol{u}'}{\partial n} - p'\boldsymbol{n} &= 0, && \Gamma_t \cup \Gamma_o \\ \boldsymbol{u}' &= \boldsymbol{f}'. && \Gamma_i \end{aligned} \tag{4.3}$$

Such a model corresponds more closely to the assumptions of local spatial stability, WKBJ and PSE approximations. In this case, the gain between a harmonic inflow forcing and the corresponding response is measured as

$$G^{bc}_{opt}(\omega) = \max_{\widetilde{\boldsymbol{f}}} \left(\int_\Omega |\widetilde{\boldsymbol{u}}|^2 r \,\mathrm{d}r\,\mathrm{d}x\right) \Big/ \left(\int_{\Gamma_i} |\widetilde{\boldsymbol{f}}|^2 r \,\mathrm{d}r\right). \tag{4.4}$$

4.3. *Numerical solution of the optimization problem*

The linear systems (4.1) and (4.3) are discretized by $P2$-$P1$ finite elements using the software FreeFEM++ (Hecht 2011). Let $\boldsymbol{q}$ be the discrete state vector containing all degrees of freedom related to velocity and pressure fields. Both (4.1) and (4.3) can then be written in their semi-discretized form as

$$B\dot{\boldsymbol{q}} = L\boldsymbol{q} + B_f\boldsymbol{f}, \tag{4.5}$$

where $\boldsymbol{f}$ is the discrete forcing vector and L, B and B_f are sparse matrices resulting from the finite elements discretization of the linearized Navier–Stokes equations. Let

$\boldsymbol{f} = \widetilde{\boldsymbol{f}}\exp(-\mathrm{i}\omega t)$ and $\boldsymbol{q} = \widetilde{\boldsymbol{q}}\exp(-\mathrm{i}\omega t)$ be time harmonic such that

$$-(L + \mathrm{i}\omega B)\widetilde{\boldsymbol{q}} = B_f\widetilde{\boldsymbol{f}}. \tag{4.6}$$

Perturbation amplitudes are measured in a pseudo-norm $\|\boldsymbol{q}\|^2 = \boldsymbol{q}^\dagger Q\boldsymbol{q}$ that represents the discretization of the perturbation kinetic energy:

$$\|(\boldsymbol{u}', p')\|^2 = \int_\Omega |\boldsymbol{u}'|^2 r\,\mathrm{d}r\,\mathrm{d}x. \tag{4.7}$$

The norm of the forcing vector $\boldsymbol{f}$, which appears in the denominator of (4.2) and (4.4), is expressed accordingly in discrete form as $\|\boldsymbol{f}\|_f^2 = \boldsymbol{f}^\dagger Q_f\boldsymbol{f}$. Note that $\boldsymbol{f}$ does not contain pressure components, and that Q_f therefore is symmetric positive-definite, in contrast to Q, which is positive semi-definite. The discrete optimal forcing problem can be written as

$$G_{opt}^2(\omega) = \max\frac{\|\widetilde{\boldsymbol{q}}\|^2}{\|\widetilde{\boldsymbol{f}}\|_f^2}. \tag{4.8}$$

Monokrousos *et al.* (2010) formalized a similar optimal forcing problem by use of a constrained optimization approach involving Lagrange multipliers. For linear time-harmonic problems, a more concise formalism is possible. The formulation used here, similar to that of Sipp & Marquet (2012), is briefly outlined below. Substituting (4.6) into (4.8) gives

$$\begin{aligned} G_{opt}(\omega)^2 &= \max_{\widetilde{\boldsymbol{f}}}\frac{\|(L + \mathrm{i}\omega B)^{-1}B_f\widetilde{\boldsymbol{f}}\|^2}{\|\widetilde{\boldsymbol{f}}\|_f^2}, \\ &= \max_{\widetilde{\boldsymbol{f}}}\frac{\widetilde{\boldsymbol{f}}^\dagger B_f^\dagger{(L + \mathrm{i}\omega B)^{-1}}^\dagger Q^\dagger(L + \mathrm{i}\omega B)^{-1}B_f\widetilde{\boldsymbol{f}}}{\widetilde{\boldsymbol{f}}^\dagger Q_f\widetilde{\boldsymbol{f}}}. \end{aligned}$$

Let $M_f^\dagger M_f$ be the Cholesky decomposition of Q_f, and let $\widetilde{\boldsymbol{g}} = M_f\widetilde{\boldsymbol{f}}$, i.e. $\widetilde{\boldsymbol{f}} = M_f^{-1}\widetilde{\boldsymbol{g}}$. The optimal gain can then be rewritten as

$$G_{opt}(\omega)^2 = \max_{\widetilde{\boldsymbol{g}}}\frac{\widetilde{\boldsymbol{g}}{M_f^{-1}}^\dagger B_f^\dagger{(L + \mathrm{i}\omega B)^{-1}}^\dagger Q^\dagger(L + \mathrm{i}\omega B)^{-1}B_f M_f^{-1}\widetilde{\boldsymbol{g}}}{\widetilde{\boldsymbol{g}}^\dagger\widetilde{\boldsymbol{g}}}.$$

The right-hand side of the above expression is a Rayleigh quotient, and $G_{opt}(\omega)$ is therefore the leading eigenvalue of the associated Hermitian eigenvalue problem

$${M_f^{-1}}^\dagger B_f^\dagger{(L + \mathrm{i}\omega B)^{-1}}^\dagger Q^\dagger(L + \mathrm{i}\omega B)^{-1}B_f M_f^{-1}\widetilde{\boldsymbol{g}} = \lambda\widetilde{\boldsymbol{g}},$$

which can be re-written in terms of the forcing $\widetilde{\boldsymbol{f}}$ as

$$Q_f^{-1}B_f^\dagger{(L + \mathrm{i}\omega B)^{-1}}^\dagger Q^\dagger(L + \mathrm{i}\omega B)^{-1}B_f\widetilde{\boldsymbol{f}} = \lambda\widetilde{\boldsymbol{f}}. \tag{4.9}$$

The leading eigenvalue of (4.9) and its associated eigenvector, which respectively correspond to the optimal gain and optimal forcing, are computed by using the Lanczos solver implemented in SLEPc (Hernandez *et al.* 2005). The operator $(L + \mathrm{i}\omega B)^{-1}$ and its adjoint are applied by using the sparse linear algebra package MUMPS through its PETSc interface (Balay *et al.* 2008). Finally, the operator Q_f^{-1} is applied by using a Cholesky decomposition, if memory requirements permit, or otherwise by using an ILU-preconditioned conjugate gradient method.

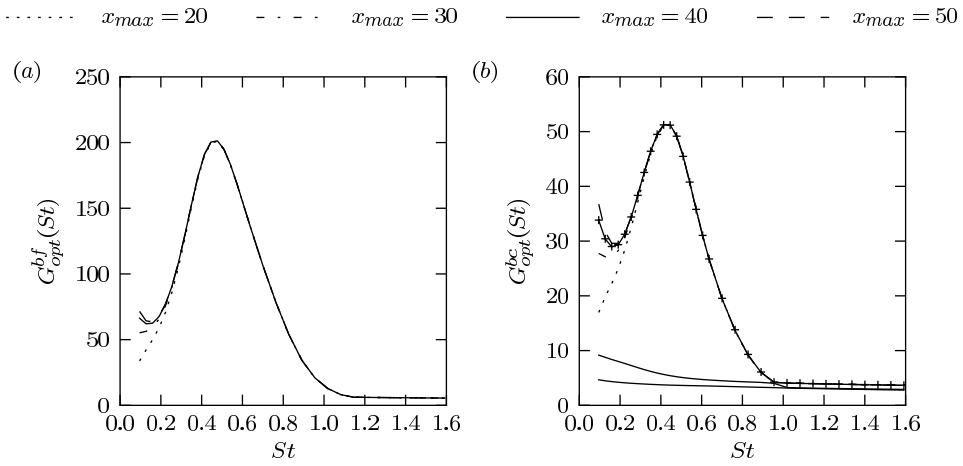

FIGURE 4. Optimal gain as a function of the Strouhal number for body (a) and boundary (b) forcing. The gains are computed for various domain lengths x_{max}. + symbols displayed in (b) correspond to gains computed for a finer mesh (mesh #2 in figure 1), showing convergence with respect to grid resolution. For boundary forcing on a domain of length $x_{max} = 40$, not only is the most amplified mode displayed but the three leading eigenvalues of (4.9) as well.

5. Results

5.1. *Optimal body forcing*

Optimal harmonic forcing by means of a distributed body force inside the jet pipe, as outlined in § 4.1, is computed first. The gain (4.2) is displayed in figure 4(a) as a function of the Strouhal number. Different line styles represent results obtained for various lengths of the computational domain, in order to assess the influence of domain truncation. Figure 5 displays the spatial distributions of axial velocity of forcing and flow response at selected Strouhal numbers, for a domain length $x_{max} = 40$. It is found from figure 4(a) that domain truncation only affects the gains at very low Strouhal numbers. The flow response structure in this regime extends far downstream, as can be seen in figure 5(a), and the truncation at the outflow therefore leads to a lower measure of the flow response norm. Neither the forcing distribution nor the captured part of the flow response appear to be significantly influenced by the downstream truncation. Similarly, it has been verified that a radial truncation at $r = 10$ has a negligible impact on the results.

The largest gain is observed at $St = 0.46$. The perturbations in the free jet exhibit a strong spatial growth in the shear layer just downstream of the nozzle exit; their amplitude peaks near the end of the potential core at $r = 8$ (figure 5(b)). In the adjacent decaying part of the wave packet, the radial amplitude distribution changes markedly, with its maximum now at the centreline. The wavepacket structure at higher frequencies displays similar characteristics, but the region of spatial growth is confined to an ever smaller distance from the nozzle.

The optimal distribution of the body force inside the pipe also exhibits consistent characteristics at all Strouhal numbers presented in figure 5. The amplitude is largest within the boundary layer at the pipe wall, and it is increasingly concentrated near the wall at higher Strouhal numbers. At the same time, the downstream spatial growth of the response increases with the Strouhal number, and its wavelength shortens. In all cases,

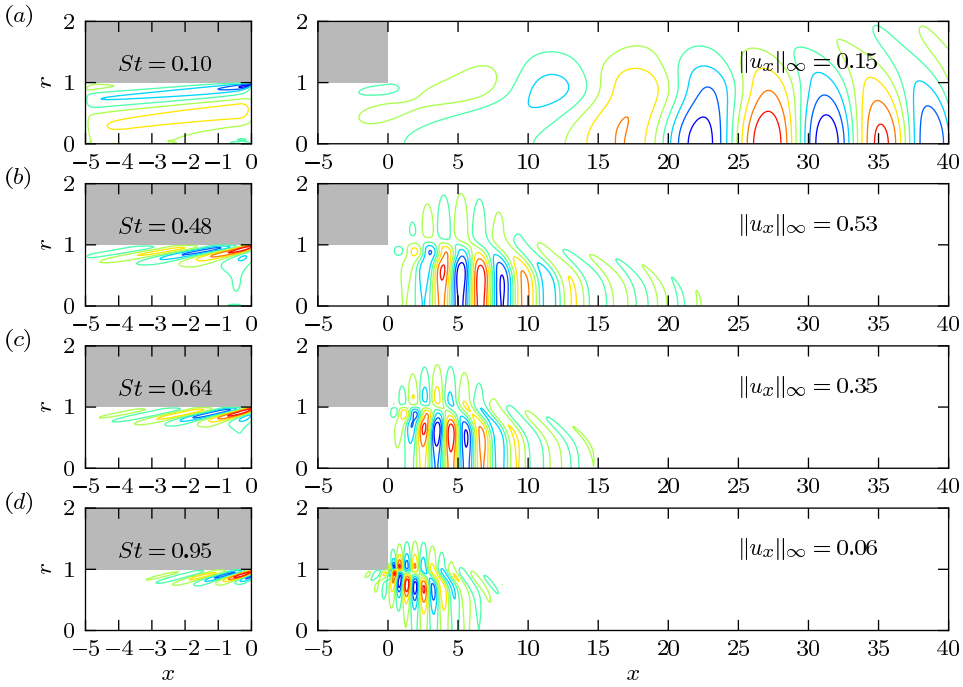

FIGURE 5. Spatial structures associated with the optimal body forcing at different Strouhal numbers, indicated in the figures. In the left column, the real parts of the axial component of the forcing is displayed. On the right, the figures show the axial component of the response velocity (real part). Computations were performed for $x_{max} = 40$.

the forcing structures are tilted upstream away from the wall, suggesting that the Orr mechanism contributes to the perturbation gain as in the case of boundary layer flow (Sipp & Marquet 2012).

Use of the L^2 norm as a measure of the amplification gain inevitably implies that spatially extended structures are given more weight than spatially localized structures, even though the latter may represent modes with high spatial amplification. This effect is undoubtedly responsible for the slight increase of G^{bf}_{opt} at very low Strouhal numbers. The infinity norm would provide a sensible and intuitive measure for the amplification of perturbations; unfortunately, this norm does not lend itself to the formulation of the optimization problem. It can however be determined *a posteriori* for the results obtained with the present approach. Values are given in figure 5 for the four cases represented. It is indeed found that the infinity norm follows the same trends as the gain defined by the L^2 norm, except for the increase at very low Strouhal numbers.

Figure 6(a) displays the maximum amplification curves obtained when the length of pipe included in the computational domain is increased from 5 to 10. It shows that this parameter affects the values of the gain but that the shape of the curve remains the same. In particular the optimal Strouhal number does not change, which confirms the relevance of the choice of geometric parameters used in this study. A more critical parameter in this analysis is the Reynolds number, as a model turbulent mean flow is used as a base state for the stability analysis so the choice is rather arbitrary: figure 6(b) indicates that the

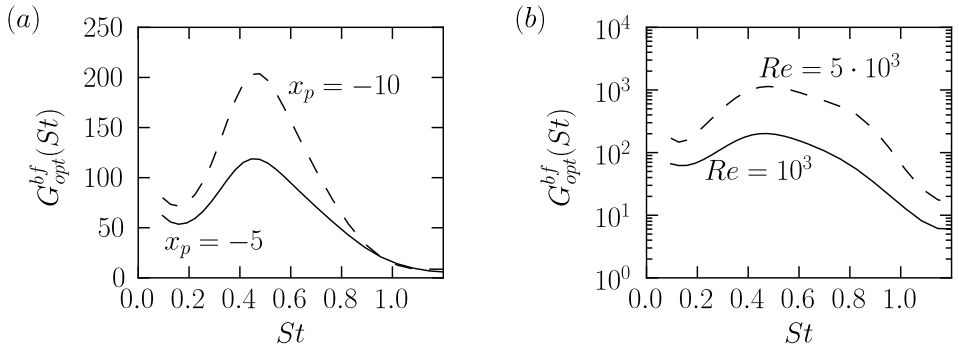

FIGURE 6. Optimal gains obtained for boundary forcing when (*a*) the length of pipe under included in the computational domain increases from 5 to 10 and (*b*) the Reynolds number increases from 10^3 to $5 \cdot 10^3$.

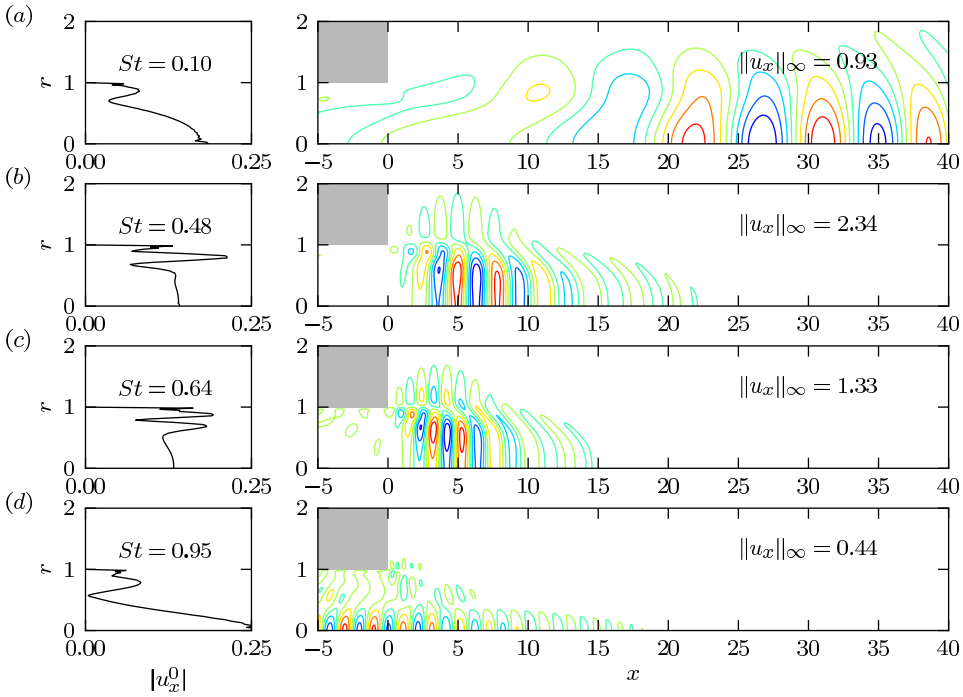

FIGURE 7. Spatial structures associated with the optimal boundary forcing at different Strouhal number, indicated in the figures. In the left column, the modulus of the inflow axial velocity component is displayed. On the right, the axial component of the response velocity is displayed (real part). Computations were performed for $x_{max} = 40$.

optimal excitation frequency remains the same when the Reynolds number is increased from 10^3 to $5 \cdot 10^3$.

5.2. *Optimal boundary forcing*

The perturbation gain obtained from the problem formulation based on forcing at the inflow boundary, as given in § 4.2, is presented in figure 4(b). The trends are very similar to those observed in the case of a distributed body force. The strongest amplification occurs at $St = 0.43$. Domain truncation has no influence, except at very low Strouhal numbers, and the results are converged with respect to mesh resolution. The radial distribution of the optimal forcing input is displayed in figure 7, alongside the flow response at the same four values of St as in the preceeding section. The flow response wavepackets are indeed nearly identical to those of figure 5, except for the highest Strouhal number shown. The forcing distributions display some unexpected features. At low St, the amplitude maximum is located on the centreline, whereas in the intermediate frequency range the highest forcing amplitudes occur in the pipe boundary layer. The no-slip condition requires the forcing to be zero at $r = 1$, but the amplitude is expected to jump to a finite value over a distance of the order of the thickness of the Stokes boundary layer, which scales as $(\omega Re)^{-1/2}$ (Batchelor 1967). Both forcing and flow response are of a different character at the highest Strouhal number shown in figure 7. Perturbations are induced around the centreline; they experience weak growth inside the pipe and immediately decay as they enter the free jet. A closer inspection of the gain curves reveals that the high-St regime is dominated by a formerly sub-optimal branch of singular values. Two additional branches are displayed in figure 4(b). Although barely visible, one of these branches becomes dominant around $St \approx 1$. The perturbation distribution shown in figure 7(d) belongs to this distinct branch.

5.3. *Comparison with local instability results*

The structure of the response wavepackets in figures 5 and 7 is readily understood from well-known local instability characteristics of jet flows (Jendoubi & Strykowski 1994; Lesshafft 2007). Strong spatial growth takes place in the potential core region, where the shear layer is thin compared to the instability wavelength. The perturbation amplitude of this local *shear-layer mode* is concentrated around $r = 1$. Downstream of the potential core, the shear layer mode stabilizes, and the *jet-column mode* takes over as the least stable, spatial local eigenmode. The amplitude of the jet-column mode in the self-similar base-flow region peaks on the jet axis. The gradual streamwise transition from a shear-layer mode to a jet-column mode is visualized in figure 8 for the wavepacket shown in figure 5(b). The thick line represents the local growth rate of the wavepacket, computed as $\frac{1}{2}\partial_x(\log E)$ with $E(x)$ as the perturbation kinetic energy at each streamwise station x integrated in the radial direction. The thin solid and dashed lines trace the spatial growth rates of the local shear-layer and jet-column modes, respectively, as functions of x. The growth rate of the global wavepacket quickly adapts to that of the shear-layer mode near $x = 0$, and it follows its decrease throughout the unstable interval. Downstream of $x \approx 5$, the global wavepacket gradually adjusts to the growth rate of the jet-column mode.

Contrary to what one might initially expect, the forcing structures displayed in figures 5 and 7 bear little resemblance to the local instability modes of the parallel flow inside the pipe. In fact, the optimization algorithm aims at finding the inflow condition that optimally excites shear layer structures such that the wave packet in the free-jet is generated with a maximum amplitude. To this end, the inflow condition consists of a superposition of local instability modes in order to exploit spatial transient amplification mechanisms (Andersson *et al.* 1999).

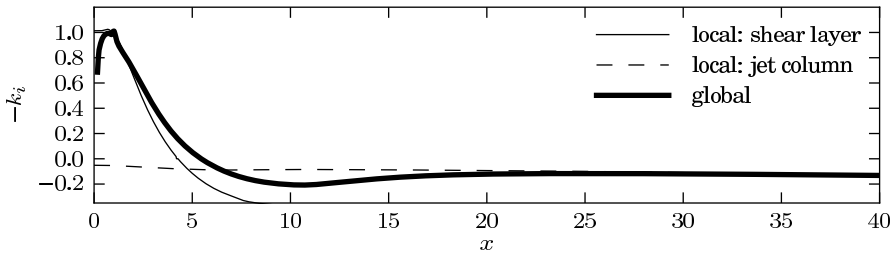

FIGURE 8. Spatial growth rate of the wavepacket envelope (thick line) corresponding to figure 5(b), compared to spatial growth rates of the local spatial shear-layer mode (thin line) and the jet-column mode (dashed line) at $St = 0.43$.

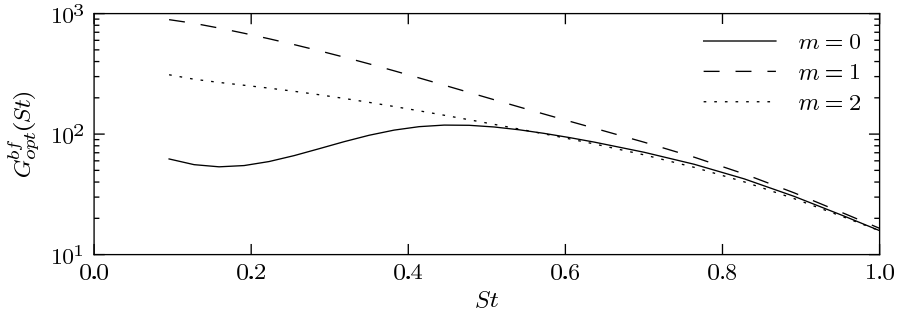

FIGURE 9. Optimal amplification of body forcing for various azimuthal wave-numbers m.

6. Conclusions

The linear dynamics of forced structures in a jet has been studied within a fully non-parallel framework, so that the effects of the base-flow spreading and of the presence of a solid jet pipe can be taken into account. Unlike in approaches using the WKBJ of PSE approximations where the frequency and inflow disturbance profile are imposed to solve for the flow evolution downstream, the present method only seeks the optimal spatial distribution of time-harmonic forcing at a given frequency.

It has been demonstrated that there is no least damped global mode that can resonate in the presence of frequency forcing. The preferred frequency obtained in the present analysis is therefore due to a pseudo-resonance rather than to a resonance as conjectures by Monkewitz (1989) and Huerre & Monkewitz (1990). The analysis of Cooper & Crighton (2000) relies on a tangent approximation of the local dispersion relation so as to obtain a "global mode" with a Gaussian enveloppe. Such an assumption is unlikely to hold in a full WKB approach or in the global analysis followed here. For this reason, one should not expect to recover the "global modes" of Cooper & Crighton in the present analysis.

Whether external forcing is modeled as an inflow condition or a body force, the amplification of external forcing has been found to be largest for a Strouhal number around 0.45. This preferred frequency is in good agreement with experimental observation at low forcing intensity (Moore 1977; Crow & Champagne 1971). Note however that, as shown in the latter reference, the preferred frequency depends on the amplitude of excitation through non-linear effects. Around this optimal frequency, the excitation generates a

wave-packet that develops in the free-jet shear layer. It is amplified through the potential core, where shear is important, and decays further downstream while it gets localized on the centreline. This behaviour is consistent with local stability results that show that, while shear-layer modes are spatially unstable in the potential core, the jet column mode becomes the least damped spatial eigenmode further downstream.

The shape of the optimal body forcing indicates that the Orr mechanism is at play to generate perturbations that grow in the jet pipe boundary layer and then optimally excite the free-jet wave-packet. The results are not very sensitive to the actual shape of the forcing term as similar results are obtained for body and boundary forcing. In both cases, a good agreement is found between the most amplified wave-packet and the experimentally observed preferred mode.

The framework of optimal forcing is therefore a suitable tool for the analysis of the non-modal instabilities developing in convection dominated amplifier flows.

Local spatial stability analysis indicates that helical perturbations, unlike axisymmetric ones, are spatially amplified downstream of the potential core, as shown e.g. by Batchelor & Gill (1962) and Michalke (1984). This is especially true in the low frequency range. Computations have been performed using the current framework for higher azimuthal wave numbers m. For $m \neq 0$, $G_{opt}(St)$ is a monotonically decreasing function of St, and the levels obtained at low frequencies are indeed larger for $m = 1, 2$ than for $m = 0$ (see figure 9). However this is not only due to a faster growth of the wave packet downstream of the nozzle, but also and most importantly to a spatial amplification over a longer streamwise distance, resulting in larger L^2 norms for the flow response. The growth of the wave-packet through the potential core is however similar for all values of m.

Experiments typically do not show a dominance of $m = 1$ helical modes in the self-similar region. Several reasons may explain this discrepancy between the results in figure 9 and observations, in particular the effects of turbulence and nonlinear saturation, which are not captured in the present analysis. In this light, the L^∞ norm might provide a more relevant and intuitive measure of the perturbation amplification. The use of such a formulation will be explored in future studies.

This work was supported by DGA grant number 2009.60.034.00.470.75.01 and by a fellowship from the EADS Foundation. Computational resources were provided by GENCI (Grant 2012-026451).

REFERENCES

Alizard, F., Cherubini, S. & Robinet, J.-C. 2009 Sensitivity and optimal forcing response in separated boundary layer flows. *Physics of Fluids* **21** (6), 064108.

Andersson, P., Berggren, M. & Henningson, D.S. 1999 Optimal disturbances and bypass transition in boundary layers. *Physics of Fluids* **11** (1), 134.

Balay, S., Buschelman, K., Eijkhout, V., Gropp, W.D., Kaushik, D., Knepley, M.G., McInnes, L. Curfman, Smith, B.F. & Zhang, H. 2008 PETSc users manual. *Tech. Rep.* ANL-95/11 - Revision 3.0.0. Argonne National Laboratory, available at http://www.mcs.anl.gov/petsc/petsc-as/.

Barkley, D 2006 Linear analysis of the cylinder wake mean flow. *Europhysics Letters* **75** (5), 750–756.

Batchelor, G.K. 1967 *An introduction to fluid dynamics*. Cambridge: Cambridge Univ. Press.

Batchelor, G. K. & Gill, A. E. 1962 Analysis of the stability of axisymmetric jets. *Journal of Fluid Mechanics* **14** (04), 529.

Cooper, A.J. & Crighton, D.G. 2000 Global modes and superdirective acoustic radiation in low-speed axisymmetric jets. *European Journal of Mechanics - B/Fluids* **19** (5), 559–574.

Crighton, D.G. & Gaster, M. 1976 Stability of slowly diverging jet flow. *Journal of Fluid Mechanics* **77** (02), 397.

Crow, S.C. & Champagne, F.H. 1971 Orderly structure in jet turbulence. *Journal of Fluid Mechanics* **48** (03), 547.

Dick, E. 2009 Introduction to finite element methods in computational fluid dynamics. In *Computational fluid dynamics: an introduction*, 3rd edn. Springer.

Garnaud, X. 2012 Modes, transient dynamics and forced response of circular jets. PhD thesis, Ecole Polytechnique.

Garnaud, X., Lesshafft, L. & Huerre, P 2011 Global linear stability of a model subsonic jet. *AIAA paper 2011-3608* .

Gudmundsson, K. & Colonius, T. 2011 Instability wave models for the near-field fluctuations of turbulent jets. *Journal of Fluid Mechanics* **689**, 97–128.

Hecht, F. 2011 Freefem++ manual, third edition, version 3.16-1. *Tech. Rep.*. Available at http://www.freefem.org/ff++.

Hernandez, V., Roman, J.E. & Vidal, V. 2005 SLEPc: a scalable and flexible toolkit for the solution of eigenvalue problems. *ACM Transactions on Mathematical Software* **31** (3), 351362.

Huerre, P. & Monkewitz, P.A. 1990 Local and global instabilities in spatially developing flows. *Annual Review of Fluid Mechanics* **22**, 473–537.

Jendoubi, S. & Strykowski, P.J. 1994 Absolute and convective instability of axisymmetric jets with external flow. *Physics of Fluids* **6** (9), 3000.

Lesshafft, L. 2007 Global modes and aerodynamic sound radiation in self-excited hot jets. PhD thesis, Ecole Polytechnique.

Marquet, O. & Sipp, D. 2010 Global sustained perturbations in a backward-facing step flow. In *Seventh IUTAM Symposium on Laminar-Turbulent Transition*.

Matsushima, T. & Marcus, P.S. 1995 A spectral method for polar coordinates. *Journal of Computational Physics* **120**, 365–374.

Michalke, A. 1984 Survey on jet instability theory. *Progress in Aerospace Science* **21**, 159–199.

Monkewitz, P.A. 1989 Feedback control of global oscillations in fluid systems. *AIAA Paper 89-0991* .

Monkewitz, P.A. & Sohn, K. 1988 Absolute instability in hot jets. *AIAA Journal* **26** (8), 911–916.

Monokrousos, A., Akervik, E., Brandt, L. & Henningson, D.S. 2010 Global three-dimensional optimal disturbances in the blasius boundary-layer flow using time-steppers. *Journal of Fluid Mechanics* **650**, 181.

Moore, C.J. 1977 The role of shear-layer instability waves in jet exhaust noise. *Journal of Fluid Mechanics* **80** (02), 321.

Nichols, J.W. & Lele, S.K. 2010 Global mode analysis of turbulent high-speed jets. Annual research briefs 2010. Center for Turbulence Research.

Nichols, J.W. & Lele, S.K. 2011*a* Global modes and transient response of a cold supersonic jet. *Journal of Fluid Mechanics* **669**, 225–241.

Nichols, J.W. & Lele, S.K. 2011*b* Non-normal global modes of high-speed jets. *International Journal of Spray and Combustion Dynamics* **3** (4), 285–302.

Pier, B. 2002 On the frequency selection of finite-amplitude vortex shedding in the cylinder wake. *Journal of Fluid Mechanics* **458**.

Ray, P.K., Cheung, L.C. & Lele, S.K. 2009 On the growth and propagation of linear instability waves in compressible turbulent jets. *Physics of Fluids* **21** (5), 054106.

Rodriguez, D., Samanta, A., Cavalieri, A.V.G, Colonius, T. & Jordan, P. 2011 Parabolized stability equation models for predicting large-scale mixing noise of turbulent round jets. In *Proceedings of the 17th AIAA/CEAS Aeroacoustics Conference*. Portland, Oregon.

Sipp, D. & Marquet, O. 2012 Characterization of noise amplifiers with global singular modes: the case of the leading-edge flat-plate boundary layer. *Theoretical and Computational Fluid Dynamics* .

Trefethen, L.N., Trefethen, A.E., Reddy, S.C. & Driscoll, T.A. 1993 Hydrodynamic stability without eigenvalues. *Science* **261** (5121), 578–584.

6.3 Effect of the azimuthal wave number

The effect of the azimuthal wave number m on the spatial development of instability waves in non-parallel incompressible jets has been studied by Strange and Crighton (1983) using a WKB analysis. In the compressible regime such an analysis has been performed using PSE by Ray et al. (2009). Their results showed that helical disturbances ($m = 1$) exhibit the largest growth, followed by modes 2 and 0. At low frequencies the gain is one order of magnitude larger for $m = 1$ than for $m = 0$; this ratio decreases with the frequency, and gains are of the same order of magnitude for the different values of m at $St \approx 1$. It should however be noted that even at low frequencies the spatial growth rates associated with axisymmetric and helical perturbations are comparable, the difference coming from the later development of the perturbation. In particular the helical perturbation continue growing downstream of the potential core, consistent with findings of Michalke (1984) and of chapter 5. The results of Gudmundsson and Colonius (2011) also show a similar trend.

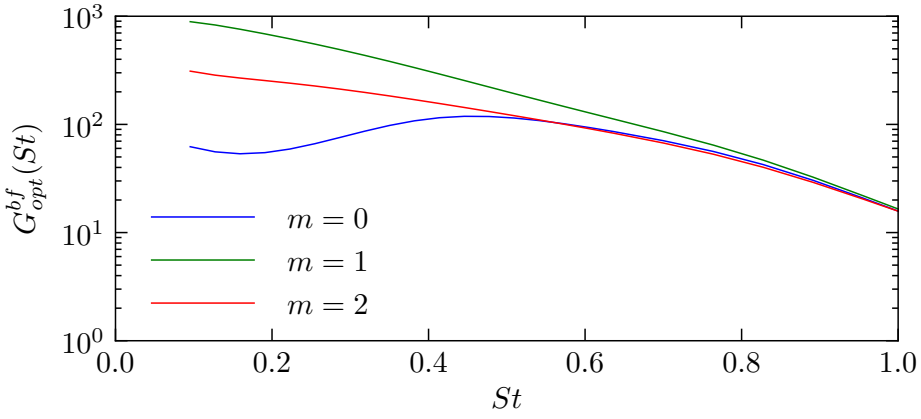

Figure 6.4: Optimal amplification of external body forcing for azimuthal wave-numbers $m = 0, 1, 2$.

The discussion in the paper was limited to axisymmetric forcing, but can be extended to any azimuthal wave-number m. The optimal gains in the case of body forcing are presented in figure 6.4 as a function of the Strouhal number. For non axisymmetric perturbations, the gain is a decreasing function of the frequency, and therefore shows no preferred frequency. While at low frequencies the gain is more than one order of magnitude larger for $m = 1$

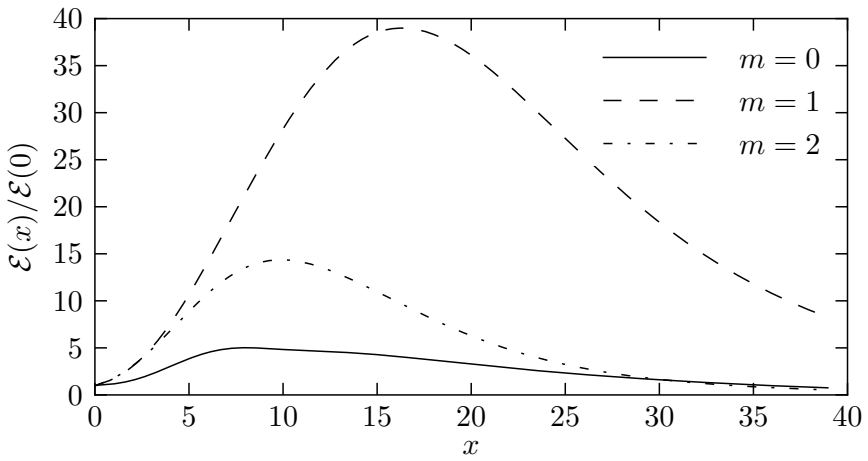

Figure 6.5: Streamwise evolution of the kinetic energy of the response, $\mathcal{E}(x) = \left(\int_0^\infty \boldsymbol{u}(r,x)^2 r\,\mathrm{d}r\right)^{1/2}$, for $St = 0.2$ and $m = 0, 1, 2$.

than for $m = 0$, this difference decreases with increasing frequency, and the same amplifications are observed for $m = 0, 1$ and 2 for $St \geq 1$. In order to describe the streamwise development of the flow response at low frequencies, the kinetic energy integrated along the radial direction is displayed in figure 6.5 as a function of the streamwise direction x. It appears that while the modes $m = 1, 2$ already grow faster than the modes $m = 0$ within the potential core, the order of magnitude of difference in the gain observed in figure 6.4 is a result of the growth of the helical mode beyond the end of the potential core, in a region where coherent structures are no longer observed.

6.4 Optimal forcing of the laminar base flow

Figure 6.6 displays the optimal body forcing amplification for the laminar base flow shown in figure 4.2. Compared to the case of the turbulent mean flow, pseudo-resonance is much stronger and takes place at a lower Strouhal number $St = 0.4$.
Although the Reynolds number is similar, much larger gains are obtained for the laminar flow as a consequence of the slow spreading of the base flow. Indeed, as shown in figure 6.7, the wave-packet is exponentially amplified over longer streamwise distances. The shape of the optimal forcing, however, is very similar to that found for the model mean flow, which is consistent with the fact that forcing should optimally excite the shear layer right downstream

of the jet pipe. At high frequencies the gains computed for the turbulent mean flow are higher than for the laminar state. This is due to the fact that the initial shear layer thickness in slightly smaller for the turbulent mean flow ($1/\theta = 23$ vs. 20 for the laminar steady flow).
It was shown in section 5.2 that the spectra obtained for laminar base states display a parabolic shear-layer branch due to numerical artifacts, and that the frequency of the least stable of these modes decreases with increasing domain length. On the contrary, the dashed curve in figure 6.6 shows that pseudo-resonance is not much affected by the numerical domain: indeed the differences seen at low frequency correspond to the different measures of the flow response, as explained earlier. The peak in the gain curve can therefore not be interpreted as a resonance with the branch of shear layer modes.

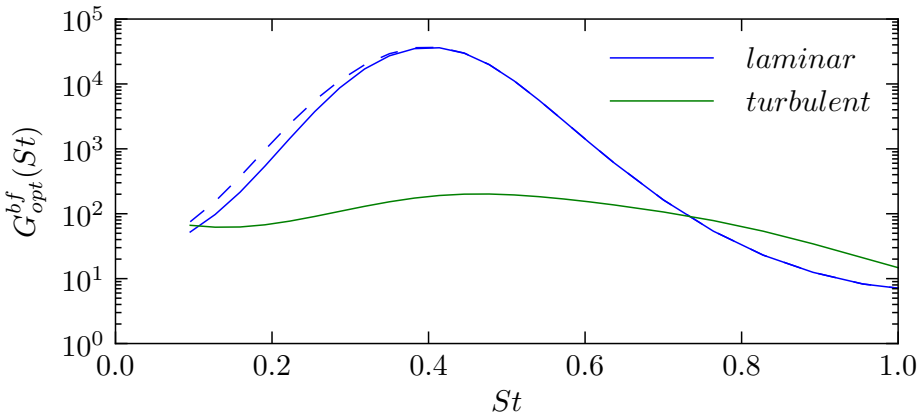

Figure 6.6: Optimal amplification of periodic body forcing for the laminar and turbulent mean flows. The dashed lime displays the results obtained for domain of length $x_\infty = 60$ ($x_\infty = 40$ is used otherwise).

6.5 A remark on the projection on stable eigenmodes.

6.5.1 Method

One way to estimate the resolvent norm for two dimensional flows – whether the objective is to compute the pseudo-spectrum or the receptivity to external forcing – is to project the dynamics onto a subset of the eigenmodes (Schmid

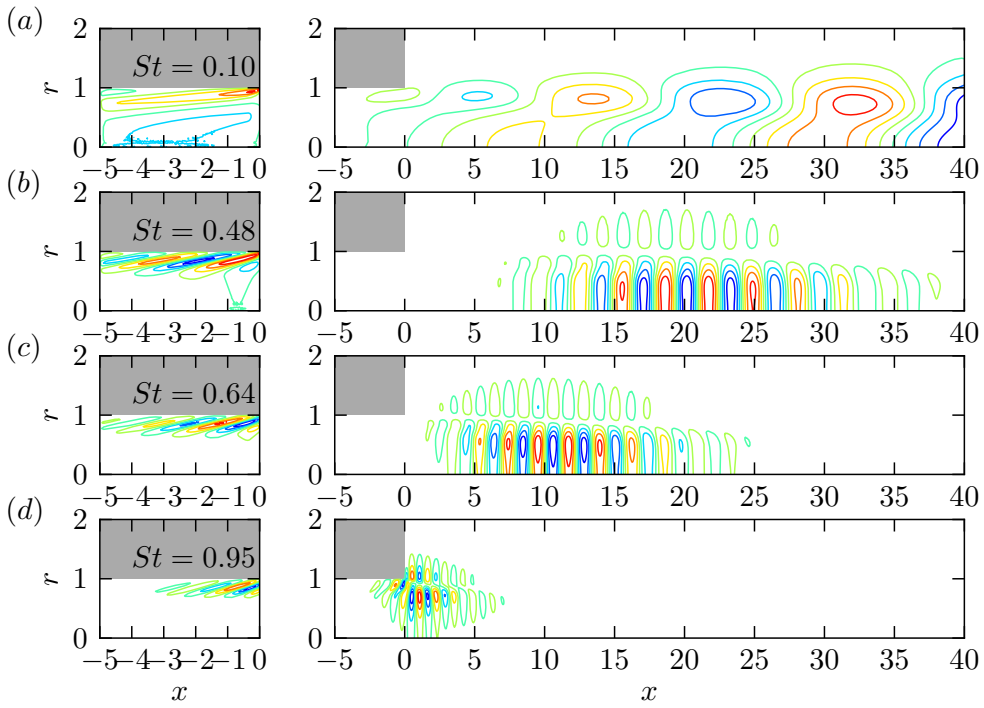

Figure 6.7: Axial velocity component of the optimal forcing (left column) and of the corresponding flow response (right column) at different Strouhal numbers for the laminar base state.

2007, Heaton et al. 2009, Nichols and Lele 2010; 2011b). Let $\boldsymbol{q}_j$ be the eigenmodes satisfying[4]

$$L\boldsymbol{q}_j = -\mathrm{i}\omega_j B\boldsymbol{q}_j, \tag{6.1}$$

and let the forcing and response belong to the space spanned by these modes:

$$\boldsymbol{q} = \alpha_j \boldsymbol{q}_j, \qquad \boldsymbol{f} = \beta_j \boldsymbol{q}_j. \tag{6.2}$$

Assuming that forcing is localized anywhere in the domain, the forcing and response are such that

$$-\mathrm{i}\omega B\boldsymbol{q} = L\boldsymbol{q} + B\boldsymbol{f}. \tag{6.3}$$

Using (6.1), (6.2) and (6.3), the coefficients α_j and β_j can be related by

$$-\mathrm{i}(\omega - \omega_j)\alpha_j = \beta_j. \tag{6.4}$$

[4]the summation convention is used

Let $\Lambda = \mathrm{diag}\,(\mathrm{i}(\omega - \omega_j)^{-1})$ such that $\boldsymbol{\alpha} = \Lambda\boldsymbol{\beta}$. The norm of the perturbation is given by

$$\begin{aligned}\|\boldsymbol{q}\|^2 &= \langle \boldsymbol{q}|\boldsymbol{q}\rangle \\ &= \langle \alpha_j \boldsymbol{q}_j|\alpha_k \boldsymbol{q}_k\rangle \\ &= \alpha_j^\dagger \langle \boldsymbol{q}_j|\boldsymbol{q}_k\rangle \alpha_k \\ &= \alpha_j^\dagger \underbrace{\boldsymbol{q}_j{}^\dagger Q \boldsymbol{q}_k}_{M_{jk}} \alpha_k \\ &= \boldsymbol{\alpha}^\dagger M \boldsymbol{\alpha}.\end{aligned}$$

As M is Hermitian positive definite it admits a Cholesky decomposition $M = LL^\dagger$. The amplification factor on the basis of eigenmodes is then given by

$$G(\omega) = \max_{\boldsymbol{\beta}} \frac{\boldsymbol{\beta}^\dagger \Lambda^\dagger M \Lambda \boldsymbol{\beta}}{\boldsymbol{\beta}^\dagger M \boldsymbol{\beta}} = \max_{\boldsymbol{\gamma}} \frac{\boldsymbol{\gamma}^\dagger L^{-1} \Lambda^\dagger L L^\dagger \Lambda L^{\dagger -1} \boldsymbol{\gamma}}{\boldsymbol{\gamma}^\dagger \boldsymbol{\gamma}} \tag{6.5}$$

The optimal gain is therefore the leading singular value of $L^\dagger \Lambda L^{\dagger -1}$.

Robustness *The method does not make use of the fact that the Cholesky factor L is triangular, therefore for robustness the Cholesky decomposition can be replaced by a factorization $U\Sigma^{1/2}\Sigma^{1/2}U^\dagger$ based on a SVD.*

6.5.2 Ginzburg-Landau problem

Let the method be first applied to the Ginzburg–Landau equation

$$\frac{\partial f}{\partial t} = -U_0 \frac{\partial f}{\partial x} - a(x) f + \nu(x) \frac{\partial^2 f}{\partial x^2}, \quad 0 \le x \le L, \tag{6.6a}$$

together with the boundary conditions

$$f(0,t) = 0, \qquad \frac{\partial^2 f}{\partial x^2}(L,t) = 0. \tag{6.6b}$$

In order to describe a situation where the dynamics are dominated by advection except in a limited region, the following parameters are considered:

$$U_0 = 1, \qquad a(x) = -a_0(1+\mathrm{i})\mathrm{e}^{-(x-10)^2}, \qquad \nu(x) = 0.2\mathrm{e}^{-\frac{(x-10)^2}{4}}.$$

The discrete operator L is obtained using high-order finite differences on a uniform mesh containing 150 uniformly distributed points on $0 \le x \le 30$. The spectrum of the discretized operator, displayed in figure 6.8(a) for $a_0 =$

1.8, shows that the dynamics are stable. The spectrum is composed of several distinct eigenmode branches; most of these are a result of the discretization and do not represent eigenmodes of the continuous problem. Close to the origin, a nearly-neutral isolated eigenvalue and a branch of more stable eigenmodes are found. Figure 6.8(b) displays the corresponding eigenmodes that grow exponentially downstream of the instability region, as shown in chapter 5. For this problem with only 150 degrees of freedom, the resolvent norm can be computed directly using a singular value decomposition of $L - \mathrm{i}\omega\mathrm{Id}$. The approach described in section 6.5.1 is however also followed here, and the transfer function is approximated by projection the dynamics on the N least stable eigenmodes. Figure 6.9 shows that although the discrete system has only 150 modes, even 100 of them do not capture the resolvent norm correctly for $\mathrm{i}\omega \in \mathbb{R}$. Furthermore, the projected and directly computed resolvent norms do not match even if all eigenmodes are taken into account due to truncation errors.
Consequently, eigenmodes are not only unsuitable to individually describe convection dominated dynamics, but even a collection of them is.

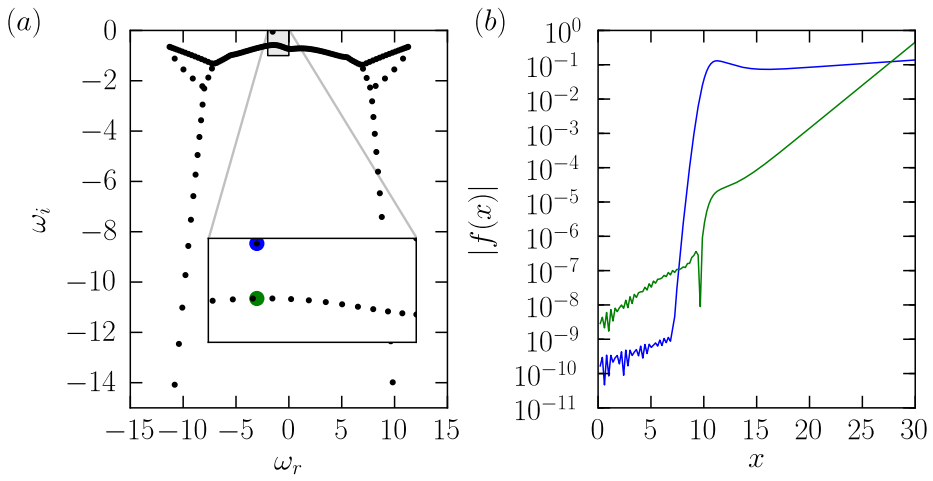

Figure 6.8: Ginzburg–Landau problem (6.6) for $a_0 = 1.8$. (a): eigenvalue spectrum. (b): Eigenvectors corresponding with eigenvalues $\omega = -1.53 - 0.05\mathrm{i}$ and $-1.38 - 0.58\mathrm{i}$.

6.5.3 Application to the incompressible jet problem

Figure 6.10 presents the optimal gain computed using the methodology of the paper together with the gain computed from the approximation based on

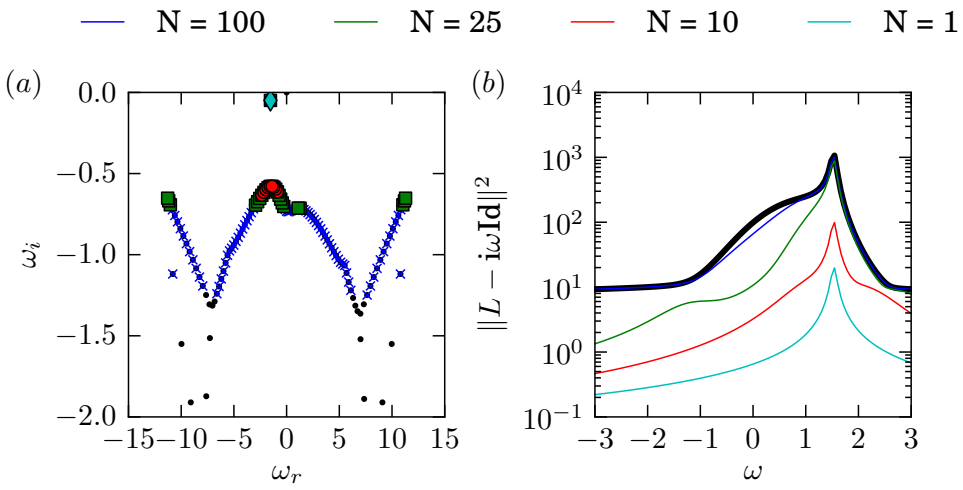

Figure 6.9: Resolvent form of the Ginzburg–Landau problem (6.6) for $a_0 = 1.8$, computed directly and using N eigenmodes. (a): portion of the eigenvalue spectrum for the projection of the dynamics. (b): Resolvent norm. The thick curve corresponds to the direct computation. 150 discretization points were used.

some of the least stable eigenmodes (see chapter 5). No agreement is found, neither quantitatively nor qualitatively, reinforcing the idea that the modal representation of the jet dynamics cannot reproduce the flow non-normal dynamics. In order to evaluate how non-normal effects are captured by the 300 modes used here, the resolvent norm approximation on the subspace spanned by the eigenmodes is displayed in figure 6.11. The distribution of contours close to the free-stream branch of eigenmodes confirms the quasi-normal behavior of this branch. Next to the shear-layer branch, the contours of the pseudo-spectrum move away from the modes as the frequency of the modes increases, a feature which is consistent with non-normal effects. This phenomenon is however clearly under-represented as a negligible effect is felt on the real ω axis, thereby resulting in a poor approximation to the amplification of time-harmonic forcing.

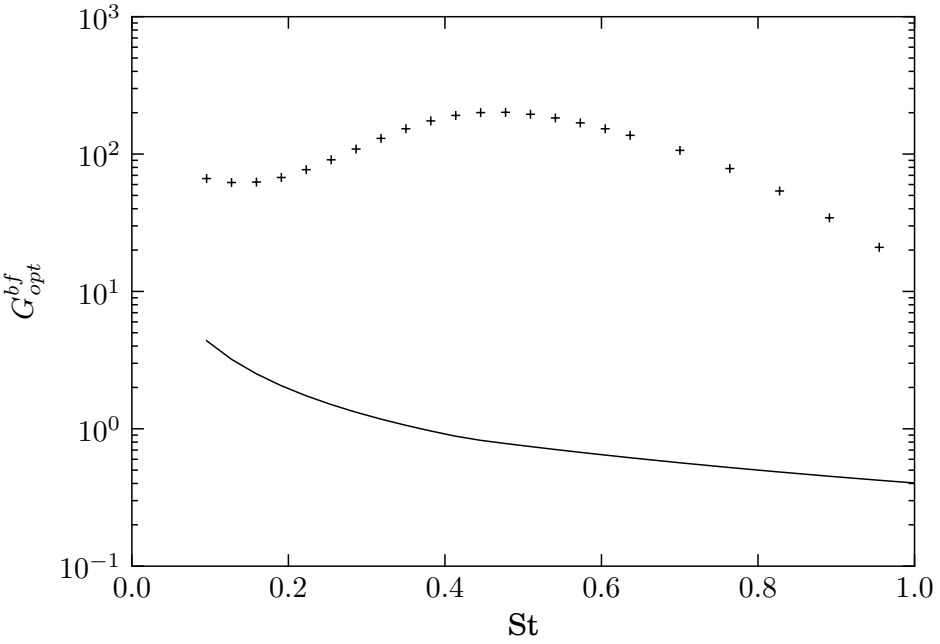

Figure 6.10: Amplification of external forcing computed using the full system (+ symbols) and a projection on 300 eigenmodes (solid line).

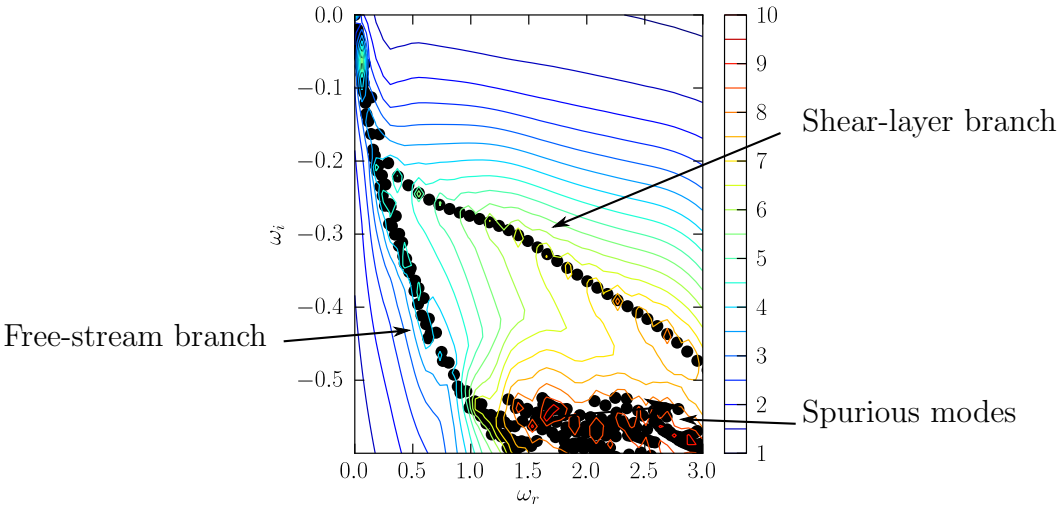

Figure 6.11: Spectrum used for the approximation of the resolvent norm (black dots) and contours of the resolvent norm (pseudo-spectrum) in logarithmic scale for a projection onto the modes.

Chapter 7

Optimal forcing of subsonic jets

7.1 Introduction

The results of the receptivity analysis for incompressible jets was presented in chapter 6. This formalism provided a suitable explanation for the pseudo-resonance of isothermal jets observed experimentally and numerically. The analysis of different types of forcing, on the boundary and inside the domain, showed that the framework is robust in identifying both the preferred frequency and the corresponding vortical structures in the jet shear layer. Previous works have shown that large scale coherent structures, and in particular the preferred mode, are responsible for most of the acoustic radiation close to the jet axis.

Crighton and Huerre (1990) modeled acoustic radiation from a traveling wave as a Helmholtz problem forced on a boundary by a traveling wave with a slowly varying envelope. These authors showed that, under certain conditions on the shape of the wave-packet, the superdirective sound emission from instability structures measured by Laufer and Yen (1983) could be recovered. Obrist (2009) extended this study to include the effects of the cross-stream envelope shape of a 2D wave-packet on the acoustic directivity pattern. This analysis shows that subsonic wave-packets may radiate sound preferably at oblique angles from the jet axis. Reba et al. (2010) modeled the instability wave in a jet using the Parabolized Stability Equations. The near-field pressure fluctuations obtained with this model are then used to compute the far field radiation through a Kirchhoff-surface approach. In order to improve the quality of the far field prediction at lower Mach numbers in a PSE approach, Rodriguez et al. (2011) did not compute the noise radiation from the near field pressure on a cone, but from the velocity distribution in the jet through an acoustic analogy.

In the present chapter, the aim is to apply the same formalism as in chapter 6 in order to determine the most efficient forcing of the linearized compressible Navier–Stokes equations *without approximation*, in order to simultaneously obtain the near- and far-field fluctuations.

7.2 Forcing and measure of the response

7.2.1 Forcing

In chapter 6, external forcing was modeled either as a body force acting in the domain or as an inflow boundary condition. Good agreement was found with respect to both the most amplified frequency and the structures observed in the free-jet region. In the present compressible setting, the geometry of the computational domain differs from the case of incompressible simulations (see chapter 2), in particular through the use of sponge layers at the far field boundaries. Furthermore, the length of the pipe included in the computational domain is roughly ten times larger in the compressible case. As a consequence – in contrast with the geometry used in the incompressible computations – modeling the forcing as an inflow condition would carry a limited physical meaning, as forcing would be applied inside a sponge layer and it would be strongly filtered by the pipe flow dynamics. Only body forcing is therefore considered, and it is restricted to the interior of the jet pipe.

Using the same notations as in chapter 6, the behavior of the discrete time-harmonic response is symbolically written as

$$-\mathrm{i}\omega\widetilde{\boldsymbol{q}} = L\widetilde{\boldsymbol{q}} + B\widetilde{\boldsymbol{f}}, \tag{7.1}$$

where B expresses the localization of the forcing.

7.2.2 Measure of the response

In order to measure the energy of perturbations in a compressible flow, the approach of Chu (1965) and Hanifi et al. (1996) is followed, as briefly outlined below. Let the energy be measured as

$$\mathcal{E} = \int_\Omega A\rho^2 + B\boldsymbol{u}^2 + CT^2 \, d\boldsymbol{x}. \tag{7.2}$$

The objective is to determine coefficients A, B and C such that in the far field, where the flow is uniform, the propagation of acoustic waves does not

contribute to the energy. The Euler equations linearized for a fluid at rest read

$$\begin{aligned}\frac{\partial \rho}{\partial t} + \rho_0 \boldsymbol{\nabla} \cdot \boldsymbol{u} &= 0,\\ \rho_0 \frac{\partial \boldsymbol{u}}{\partial t} &= -\boldsymbol{\nabla} p,\\ \rho_0 \frac{\partial T}{\partial t} &= -\gamma(\gamma-1) Ma^2 p_0 \boldsymbol{\nabla} \cdot \boldsymbol{u},\\ \frac{p}{p_0} &= \frac{\rho}{\rho_0} + \frac{T}{T_0},\end{aligned}$$

so that in this case

$$\begin{aligned}\frac{\partial \mathcal{E}}{\partial t} &= -2 \int_\Omega \left(A \rho_0 \rho \boldsymbol{\nabla} \cdot \boldsymbol{u} + \frac{B}{\rho_0} \boldsymbol{u} \cdot \boldsymbol{\nabla} p + CT \frac{p_0}{\rho_0} \gamma(\gamma-1) Ma^2 \boldsymbol{\nabla} \cdot \boldsymbol{u} \right) \mathrm{d}\boldsymbol{x}\\ &= -2 \int_\Omega (A \rho_0 \rho - \frac{B}{\rho_0} p + CT \frac{p_0}{\rho_0} \gamma(\gamma-1) Ma^2) \boldsymbol{\nabla} \cdot \boldsymbol{u} \, \mathrm{d}\boldsymbol{x} + 2 \int_{\partial\Omega} B \boldsymbol{u} \cdot \boldsymbol{n} p \, \mathrm{d}\boldsymbol{x}.\end{aligned}$$

For $B = \rho_0$, choosing A and C such that

$$A = \frac{p_0}{\rho_0}, \qquad\qquad C = \frac{\rho_0^2}{\gamma^2(\gamma-1) Ma^4 p_0},$$

the compression work associated with acoustic waves does not contribute to $\mathcal{E}$. The following norm is therefore used in order to measure the amplitude of time harmonic forcing terms and flow responses:

$$\mathcal{E}(\widetilde{\boldsymbol{q}}) = \int_{\widetilde{\Omega}} \left(\rho_0 \widetilde{\boldsymbol{u}}^2 + \frac{p_0}{\rho_0} \widetilde{|\rho|}^2 + \frac{\rho_0^2}{\gamma^2(\gamma-1) Ma^4 p_0} |\widetilde{T}|^2 \right) r \, \mathrm{d}r \, \mathrm{d}x. \tag{7.3}$$

In order to avoid numerical artifacts at the outer boundaries of the computational domain where the grid is stretched, the integral is taken only on the physical domain $\widetilde{\Omega}$ and not in the sponge layers.

Since the optimal forcing formalism does not require the measure of the flow response to be a norm, the response can also be measured in terms of its acoustic radiation. For this purpose, the acoustic power across radiated across a control surface Σ is considered. Physically, the acoustic power is then given as

$$F = \int_\Sigma \widehat{p}\widehat{u}_n r \, \mathrm{d}l, \tag{7.4}$$

where $\widetilde{p}$ and $\widehat{u}_n$ denote the "real" pressure field and velocity perturbations

normal to Σ, i.e.

$$\begin{aligned} F &= \int_\Sigma \Re(p)\Re(u_n) r \,\mathrm{d}l \\ &= \int_\Sigma \frac{\widetilde{p}\mathrm{e}^{-\mathrm{i}\omega t} + \widetilde{p}^\dagger \mathrm{e}^{\mathrm{i}\omega t}}{2} \frac{\widetilde{u}_n \mathrm{e}^{-\mathrm{i}\omega t} + \widetilde{u}_n^\dagger \mathrm{e}^{\mathrm{i}\omega t}}{2} r \,\mathrm{d}l \\ &= \frac{1}{4}\int_\Sigma \left(\widetilde{p}\widetilde{u}_n^\dagger + \widetilde{p}^\dagger \widetilde{u}_n + \widetilde{p}\widetilde{u}_n \mathrm{e}^{-2\mathrm{i}\omega t} + \widetilde{p}^\dagger \widetilde{u}_n^\dagger \mathrm{e}^{2\mathrm{i}\omega t}\right) r \,\mathrm{d}l. \end{aligned}$$

The average power over one period is therefore given by

$$\langle F \rangle = \frac{1}{4}\int_\Sigma \left(\widetilde{p}\widetilde{u}_n^\dagger + \widetilde{p}^\dagger \widetilde{u}_n\right) r \,\mathrm{d}l \equiv \mathcal{F}(\widetilde{\boldsymbol{q}}). \tag{7.5}$$

This is obviously not a norm, but since forcing is restricted to the inside of the jet pipe it can be expected to be a positive value. Note that the averaging procedure could be applied in exactly the same way for the compressible norm in (7.3).

In the present chapter, the control surface Σ is taken to be a cylinder of radius $R = 10$. Note that if Σ is a circle large enough so that perturbations are purely acoustic, then the velocity fluctuations are given by $u = Ma \cdot p$, so that

$$F(\widetilde{\boldsymbol{q}}) = \frac{1}{2}\int_\Sigma Ma|\widetilde{p}|^2 r \,\mathrm{d}l.$$

Whether the compressible norm or the acoustic power are used as an objective functional for the maximization procedure, the amplitude of the perturbation is always measured in terms of the norm (7.3) (the integration domain is this time $\widetilde{\Omega}_f$, the portion of jet pipe included in the physical domain).

7.3 Numerical procedure

As it was mentioned before in chapter 3, direct solvers would be too costly for the discretization of compressible flows, so the numerical procedure used implemented in chapter 6 cannot be used here. The formalism being the same, the optimal forcing is given by

$$\widetilde{\boldsymbol{f}}_{opt} = \arg\max_{\widetilde{\boldsymbol{f}}} \frac{\widetilde{\boldsymbol{f}}^\dagger B^\dagger (L + \mathrm{i}\omega \mathrm{Id})^{-1^\dagger} Q (L + \mathrm{i}\omega \mathrm{Id})^{-1} B \widetilde{\boldsymbol{f}}}{\widetilde{\boldsymbol{f}}^\dagger Q_f \widetilde{\boldsymbol{f}}}, \tag{7.6}$$

where Q corresponds to the discretization of either (7.3) (situation referred to as the energy problem, or problem E) or (7.5) (situation referred to as

the acoustic problem, or problem A). Q_f corresponds to the discretization of (7.3) on $\widetilde{\Omega}_f$; since it is positive definite, it admits a Cholesky decomposition, $Q_f = M_f^\dagger M_f$. From (7.6) it appears that the optimal forcing can be computed from the leading eigenvector $\widetilde{\boldsymbol{g}}$ of

$$\underbrace{M_f^{\dagger -1} B^\dagger (L + \mathrm{i}\omega \mathrm{Id})^{-1\dagger} Q (L + \mathrm{i}\omega \mathrm{Id})^{-1} B M_f^{-1}}_{\mathcal{L}_\omega} \widetilde{\boldsymbol{g}} = \lambda \widetilde{\boldsymbol{g}} \tag{7.7}$$

As a finite difference discretization is employed, both M_f and M_f^{-1} are easily computed by hand. Consequently, in order to iteratively compute the leading eigenvector $\widetilde{\boldsymbol{g}}$ (using a Lanczos method), the only costly part in applying $\mathcal{L}_\omega$ is the application of $(L+\mathrm{i}\omega\mathrm{Id})^{-1}$ and its adjoint. Based on the observation that solving $(L + \mathrm{i}\omega\mathrm{Id})\boldsymbol{x} = \boldsymbol{y}$ corresponds to finding the time harmonic response $\boldsymbol{x}$ to a forcing $\boldsymbol{y}$, $(L + \mathrm{i}\omega\mathrm{Id})^{-1}$ can be approximately applied through a time stepping of the forced linearized Navier–Stokes equations over a sufficiently long time interval so that transient effects die out. In Monokrousos et al. (2010) the solution is then Fourier-transformed in time to extract the solution to $(L+\mathrm{i}\omega\mathrm{Id})\boldsymbol{x} = \boldsymbol{y}$. A variation of the method is used here: instead of solving

$$\dot{\boldsymbol{x}} = L\boldsymbol{x} + B\boldsymbol{y}\mathrm{e}^{-\mathrm{i}\omega t}$$

until convergence to a time harmonic state is achieved, the equivalent system

$$\dot{\boldsymbol{x}} = (L + \mathrm{i}\omega\mathrm{Id})\boldsymbol{x} + B\boldsymbol{y} \tag{7.8}$$

is integrated in time until a steady solution is found, which can be speeded-up by the use of a local time step. The time of integration is determined a priori, such that the same operator $\mathcal{P}_\omega \approx (L+\mathrm{i}\omega\mathrm{Id})^{-1}$ is applied at each iteration of the Krylov solver. The main difference between the present numerical procedure and that of Monokrousos et al. (2010) lies in the approximate solution of the adjoint system. In order to ensure a fast and reliable convergence of the Lanczos method, $(L^\dagger - \mathrm{i}\omega\mathrm{Id})^{-1}$ is approximated using $\mathcal{P}_\omega^\dagger$: for this purpose the number of time steps used for applying $\mathcal{P}_\omega$ and $\mathcal{P}_\omega^\dagger$ is the same, and the time stepping algorithm used for $\mathcal{P}_\omega^\dagger$ is distinct from the standard Runge-Kutta method implemented for $\mathcal{P}_\omega$, as described in chapter 2.

7.4 Results

7.4.1 Optimal energy responses: near field

Optimal forcing have been computed for the model flow described in chapter 4 at a Mach number $Ma = 0.75$, first for the energy problem. The

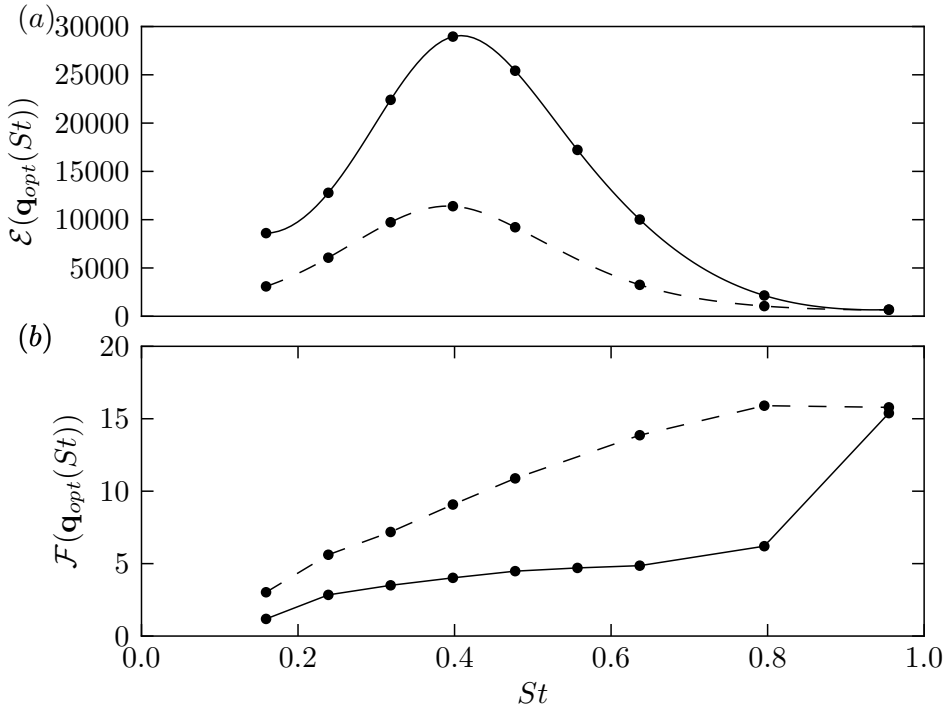

Figure 7.1: Energy and acoustic power of the responses $\boldsymbol{q}_{opt}$ to axisymmetric ($m = 0$) forcing of unit energy ($\mathcal{E}(\boldsymbol{f}_{opt}) = 1$) for a compressible jet at $Ma = 0.75$. Results obtained for a maximization of the energy are displayed as solid lines, and dashed lines are used for the responses maximizing the acoustic power. (a): energy. (b): acoustic power across a cylinder of radius $R = 10$. For consistency between (a) and (b), the gain in energy is displayed in (a) while the gain in amplitude (i.e. the square root of the results presented here) was used in chapters 5 and 6.

computed gains in energy are displayed in figure 7.1(a) as a function of the Strouhal number. Although a quantitative comparison with the gains described in chapter 6 would be meaningless as the norms used in both cases differ, results are quantitatively very similar. The most amplified frequency is found to be $St = 0.40$ and the corresponding gain *in amplitude* is larger than 170. The vorticity fields of the flow response to the optimal forcing at various frequencies are displayed in figure 7.2. Consistent with a phase velocity that remains of the same order, the typical size of the structures reduces as the frequency increases, and so does the extent of the wave-packet. While right downstream of the jet pipe the vorticity field exhibits lobes of

positive and negative signs on each side of the shear layer – characterizing a Kelvin-Helmholtz instability – only one structure is observed along the radial direction further downstream. These structures are reminiscent of the results for global modes and optimal perturbations in chapter 5 and are consistent with structures being advected downstream.

The forcing structures, to be further described later, are also similar to those found in the incompressible case.

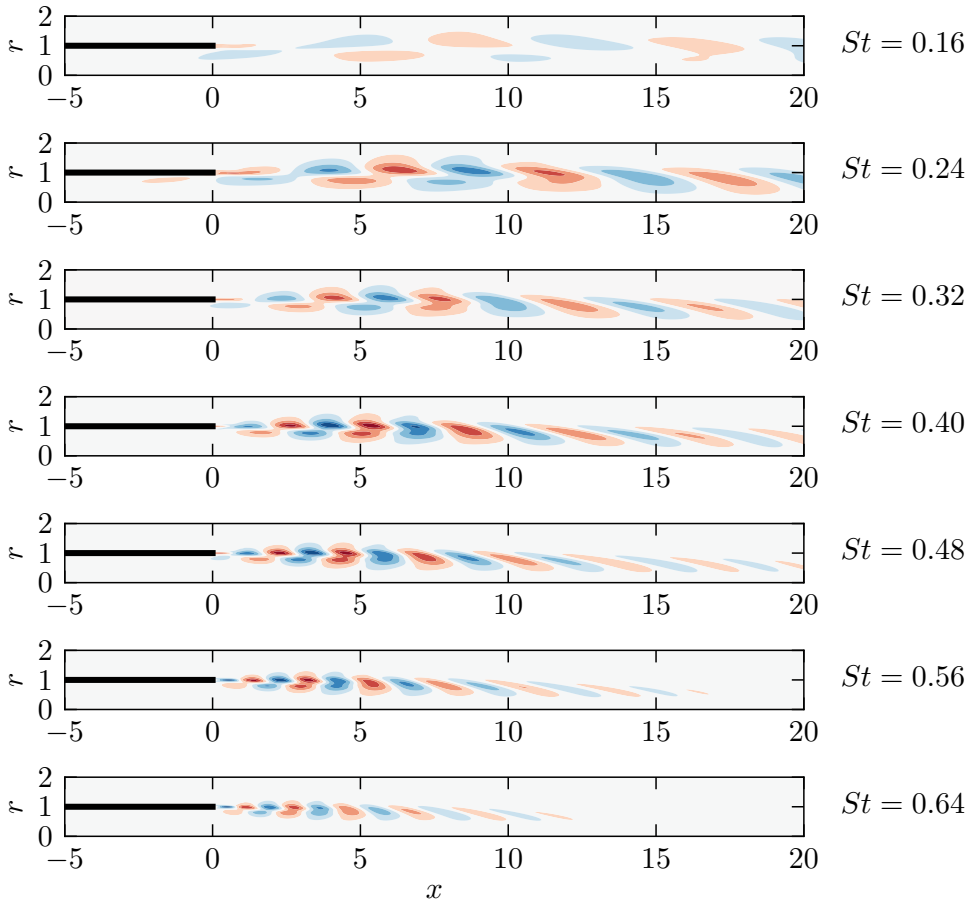

Figure 7.2: Azimuthal vorticity fields ($(\boldsymbol{\nabla}\times\boldsymbol{u})\cdot\boldsymbol{e}_\theta$) for optimal axisymmetric ($m=0$) responses in a compressible jet at $Ma=0.75$ (problem E).

The transition of the flow response from a shear-layer to a jet-column perturbation is also observed in the PSE results of Rodriguez et al. (2011).

These authors however report a flow response that extends over a much larger region in the streamwise direction. In addition to a different methodology, this could also be attributed to a different base flow and Reynolds number.

7.4.2 Acoustic radiation of the responses of maximum energy

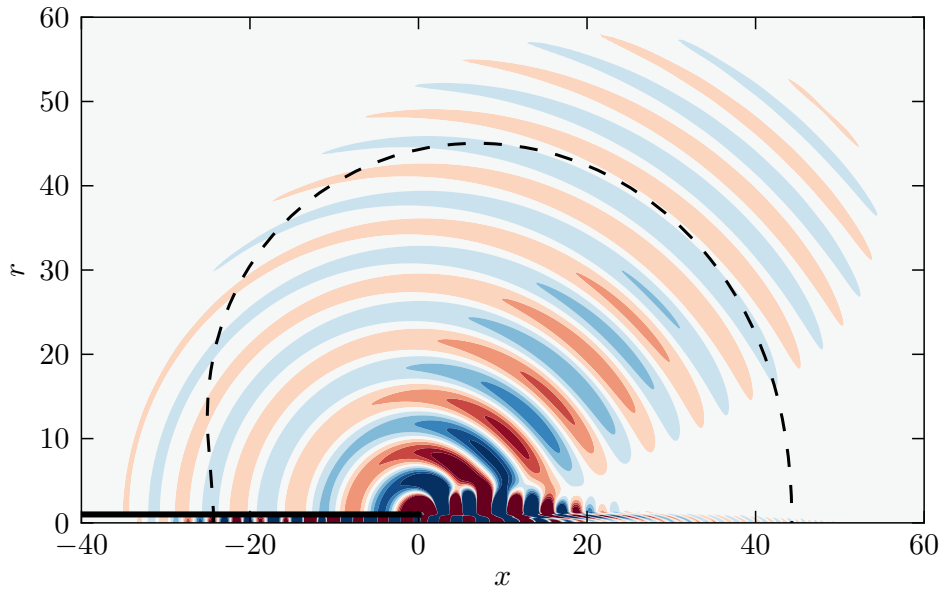

Figure 7.3: Dilatation field ($\boldsymbol{\nabla} \cdot \boldsymbol{u}$) for the optimal axisymmetric response in a compressible jet at $Ma = 0.75$ and $St = 0.4$. The limits of the sponge layer are represented in dashed lines.

While with an incompressible analysis an acoustic analogy is necessary to get information about the acoustic features of the most amplified forced structures, the present compressible analysis gives direct access to the acoustic radiation. The acoustic field of the response at the preferred frequency is displayed in figure 7.3. As for any other excitation frequency, the dilatation field shows that acoustic waves are emitted from a region right downstream of the jet pipe; these waves propagate outwards with a maximum amplitude at an angle varying from 20° to 55° from the jet axis. In order to characterize

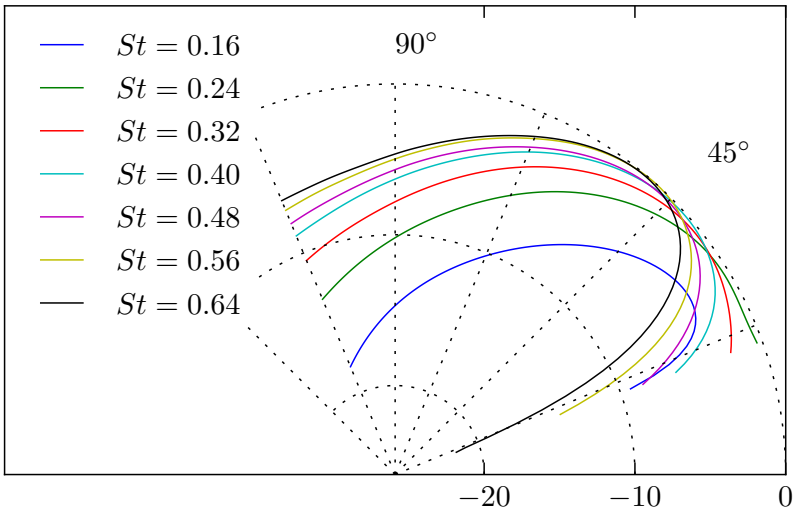

Figure 7.4: Directivity of the acoustic radiation for optimal axisymmetric ($m = 0$) perturbations at different frequencies ($Ma = 0.75$). The amplitude of the dilatation field $|\boldsymbol{\nabla} \cdot \boldsymbol{u}(\rho\cos(\vartheta), \rho\sin(\vartheta))|$ is displayed on a circle of radius $\rho = 20$ as a function of the angle ϑ (in dB).

the directivity of noise emission, the amplitude of the dilatation field on a circle of radius 20 centered at the origin is displayed in figure 7.4. Except for the lower Strouhal number, $St = 0.16$, it appears that the maximum amplitude of the radiated field is approximately constant for all excitation frequencies. Figure 7.1(b), shows that the radiated power actually increases slowly with the frequency. The angle of maximum variation increases from 20° for $St = 0.24$ to 55° for $St = 0.64$. This observation is in agreement with experimental measurements (Lush 1971, Bogey et al. 2007) that show that the peak frequency in the acoustic spectrum increases with the angle of observation with respect to the jet axis.

7.4.3 Optimal acoustic radiation

Optimizing the forcing for maximum acoustic radiation (problem A) identifies the same flow responses as the optimization of the norm of the flow response. Results are presented in figure 7.5 for a Strouhal number of 0.48; on the left column are displayed fields obtained for the energy problem and on the right fields for the acoustic problem. The same color scales are used on both sides.

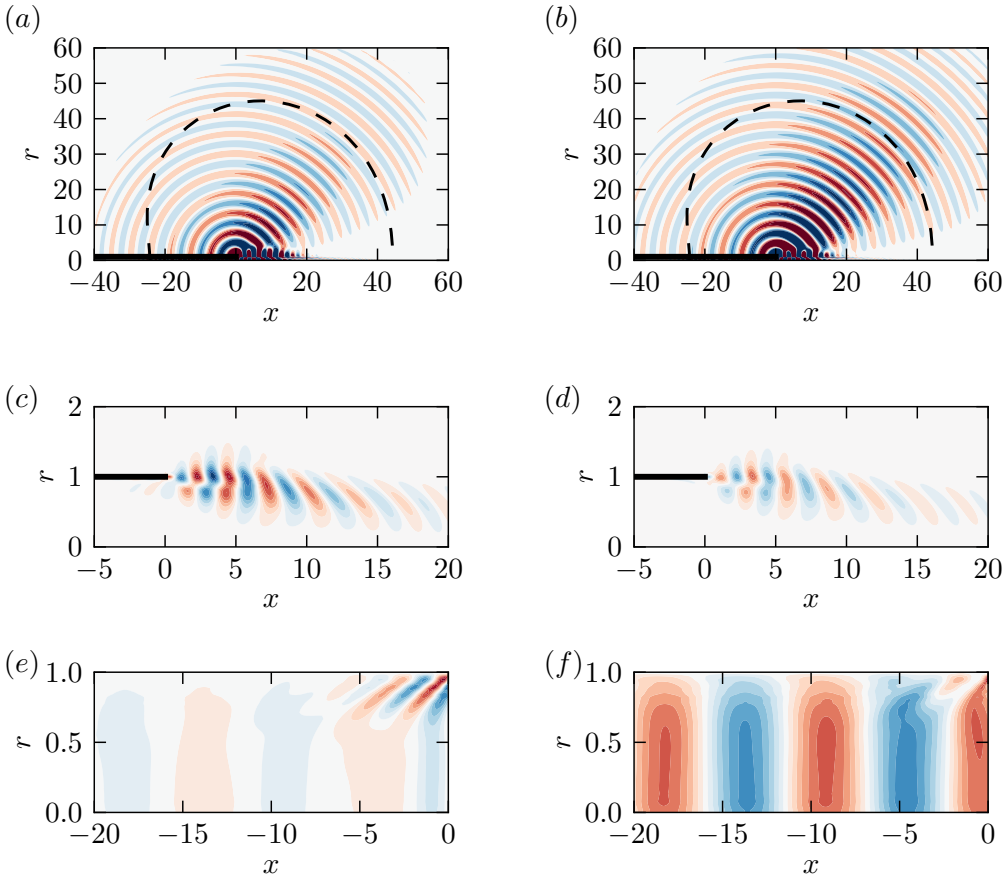

Figure 7.5: Optimal axisymmetric ($m = 0$) forcing and flow responses for $Ma = 0.75$ and $St = 0.48$. On the left, results are presented for an optimization of the energy norm (7.3). Figures on the right display results computed for the maximization of the acoustic power (7.5). (a, b) : dilatation $\boldsymbol{\nabla} \cdot \boldsymbol{u}$, (c, d) : azimuthal vorticity $(\boldsymbol{\nabla} \times \boldsymbol{u}) \cdot \boldsymbol{e}_\theta$, (e, f) : forcing applied to the axial velocity. The same color scales are used in the left and right columns for vorticity and dilatation fields.

Figures 7.5$(a - d)$ show that both the dilatation and vorticity fields present very similar distributions. As expected the intensity of the dilatation field is larger for maximum acoustic power and the intensity of the vorticity field is larger for maximum energy norm, but they lie within a factor of 2 of each other, as can be observed in figure 7.1(a, b).

The shapes of the forcing, presented in figures 7.5$(e - f)$, are however significantly different for the two objective functionals. Upstream tilted boundary-layer structures are observed in case E, similar to the incompress-

ible results presented in chapter 6. Such a forcing optimally excites the shear layer structures downstream of the nozzle. In case A on the contrary, the optimal forcing identified by the formalism takes the form of an acoustic wave that is scattered at the end of the jet pipe – thus contributing to the acoustic response – and that also efficiently excites shear layer structures in the free-jet.

The similarity of the results obtained in cases E and A show the robustness of the optimal forcing formalism in identifying relevant structures in the jet.

7.4.4 Transients

The transient dynamics of forced perturbations is considered. For each excitation frequency the optimal forcing $\boldsymbol{f}_{opt}$ (normalized such that $\mathcal{E}(\boldsymbol{f}_{opt}) = 1$) is used to compute the temporal evolution of a perturbation set to zero at $t = 0$. As shown in figure 7.6(a, c) the norm of the perturbation monotonically increases in time until it reached an asymptotic value for both acoustic and vortical forcing. In order to evaluate the typical time where transient dynamics dominate over the time harmonic response, the time T_{sat} is defined for each forcing as $\mathcal{E}(\boldsymbol{q}(T_{sat}))^{1/2} = 95\%\mathcal{E}(\boldsymbol{q}(\infty))^{1/2}$. Figures 7.6$(b, d)$ shows that at low frequency the time harmonic regime is nearly attained after 5 forcing periods. At higher frequencies it takes of the order of 20 periods to reach the time harmonic response, which is surprising as the extent of the response in the streamwise direction decreases with the frequency.

7.5 Conclusions and outlook

The acoustic radiation for instability wave in compressible jets has been analyzed in terms of the optimal time harmonic forcing. Computations have been performed in order to identify the external disturbances that generate flow disturbances with the maximum energy or acoustic radiation. As for incompressible jets in chapter 6, the results of this chapter identify a preferred Strouhal number of around 0.4 for axisymmetric forcing. Optimal forcing terms that maximize acoustic radiation take the form of acoustic waves propagating through the jet pipe; while it is expected that the energy of the flow response is lower in this case than when the latter is maximized, results show that an acoustic forcing terms also efficiently excites vortical structures in the jet. This shows the receptivity of jet flows to acoustic disturbances.

The acoustic field of the optimal responses, for both objective functionals, show that sound waves are emitted at a preferred angle ϑ for the jet axis

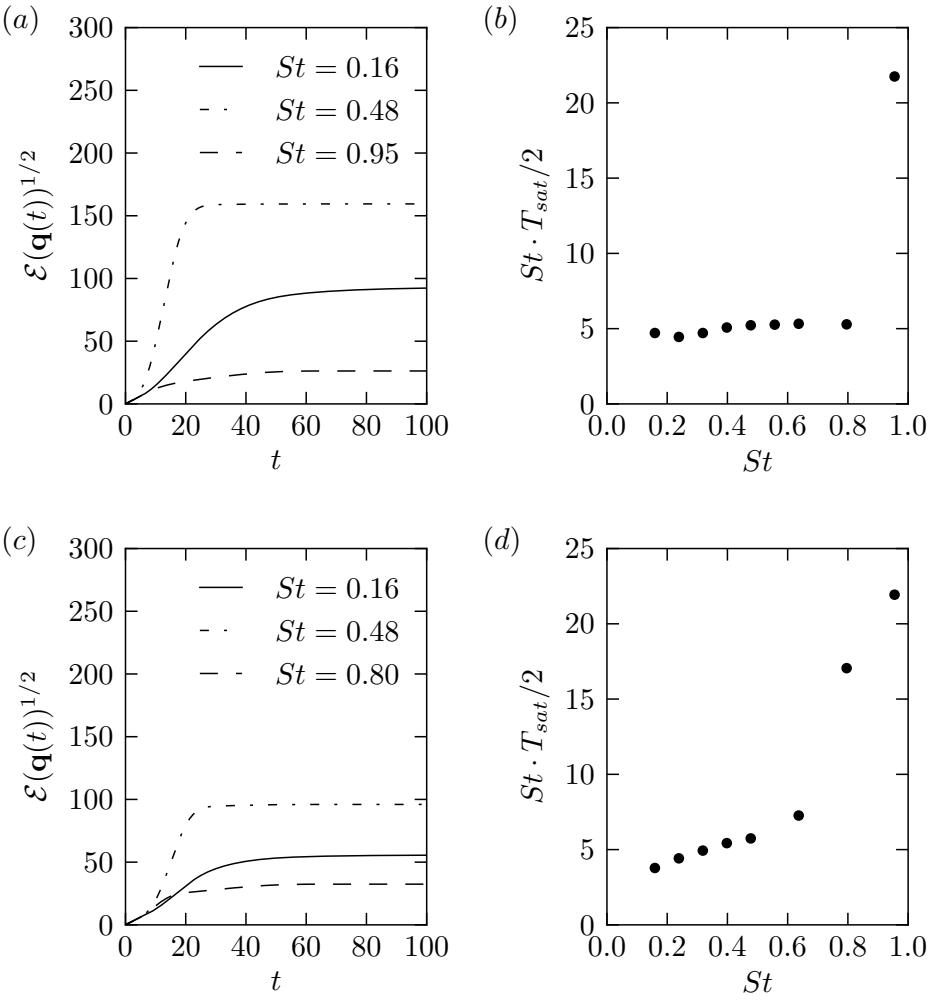

Figure 7.6: Transient evolution of the perturbation until the time harmonic regime is reached for case E (top row) and A (bottom row). (a, c): temporal evolution of the amplitude of the response. (b, d): number of periods required for the norm of the response to reach 95% of its asymptotic value.

that increases from 20° to 55° as the frequency of excitation increases. It is however unclear in this approach which portion of the sound is radiated by the instability wave and which portion directly comes from the forcing. Indeed Lighthill's equation becomes

$$\frac{\partial^2 \rho}{\partial t^2} - c_\infty^2 \boldsymbol{\nabla}^2 \rho = \frac{\partial^2}{\partial x_i \partial x_j} \left(\rho u_i u_j + (p - c_\infty^2 \rho) \delta_{i,j} \right) + \frac{\partial f_\rho}{\partial t} + \frac{\partial f_{\rho u_i}}{\partial x_i}$$

when forcing is applied. The contribution of the last two terms in the above

equation to the acoustic field will therefore need to be assessed before conclusions can be drawn about the acoustic field radiated by the jet preferred mode.

Chapter 8

Conclusions and outlook

The relevance of different tools commonly used for the study of linear stability features in a global framework have been assessed for the description of large scale coherent motion in jet flows.

Optimal perturbations in jet flows, presented in chapter 5, are in most situations localized in the boundary layer of the pipe, next to the nozzle. The perturbations grow as they are convected downstream: they are amplified first by the Orr mechanism and then by the shear layer instability in the potential core. In the self-similar region a slow decay or amplification of the wave-packet is observed depending on the azimuthal wave number. In such a situation it has been shown that a modal representation fails to capture the dynamics of perturbations for both numerical and physical reasons. The eigenspectrum does not display any least stable frequency that could explain the preferred mode, and even a superposition of all of the computed modes cannot reproduce the transient features.

In chapter 6 the *axisymmetric* preferred mode of the jet was described in terms of the optimal flow forcing in an incompressible setting. The transfer function, which describes the maximum amplification of external forcing at a given frequency, exhibits a clear maximum at $St \approx 0.4$ for both boundary and body forcing. The flow response is very similar for both types of external disturbances. Results demonstrate that as the forcing frequency increases the spatial extent of vortical structures in the flow decreases but that the initial growth of the wave-packet just downstream of the nozzle increases. The preferred mode may therefore be seen as a compromise between fast spatial growth rates and the large spatial extent of the structures. Comparison with local stability analysis reveals that the spatial structure of the flow response gradually changes from a local *shear-layer* mode next to the nozzle to a local *jet-column* mode downstream of the potential core.

Non-axisymmetric optimal gains do not exhibit a preferred frequency

since helical low frequency perturbations remain amplified over very large streamwise regions. As the amplitude of the flow response is measured in terms of its L^2 norm over the whole computational domain, such helical forcings appear to be the most amplified. An analysis of the spatial development of the flow response, however, demonstrates that results are consistent with those of Strange and Crighton (1983).

Compressibility effects have been investigated in chapter 7. It has been shown that acoustic waves efficiently excite shear layer structures, and that wavepackets are responsible for a directive sound emission. Further investigation will, however, be necessary in order to draw clearer conclusions.

In order to perform the linear stability analyses, existing solvers have been adapted to provide memory-efficient and scalable methods that may be applied to more complex two- or three-dimensional discretizations. In particular, in a direct extension of this study, the optimal forcing analysis will be performed on the turbulent mean flows computed by DNS in Sandberg et al. (2012), in order to compare the preferred structures obtained for the linearized equations to features of a randomly forced flow.

A missing ingredient in our analysis is the modeling of the effect of fine scale turbulence on coherent structures, as presented by Reynolds and Hussain (1972). Several methods are possible, ranging from a simple eddy viscosity model (Pujals et al. 2009) to the linearization of a turbulence model (Crouch et al. 2007). Such an approach however is uncertain due to the poor prediction of coherent structures and their radiated sound by RANS models.

Bibliography

E. Akervik, U. Ehrenstein, F. Gallaire, and D. S. Henningson. Global two-dimensional stability measures of the flat plate boundary-layer flow. *European Journal of Mechanics - B/Fluids*, 27(5):501–513, 2008.

P. R. Amestoy, I. S. Duff, and J. Y. L'Excellent. Multifrontal parallel distributed symmetric and unsymmetric solvers. *Computational Methods in Applied Mathematics*, 184(2-4):501–520, 2000.

C. Bailly, C. Bogey, and O. Marsden. Progress in direct noise computation. *International Journal of Aeroacoustics*, 9(1):123–144, 2010.

S. Balay, K. Buschelman, V. Eijkhout, W. D. Gropp, D. Kaushik, M. G. Knepley, L. Curfman McInnes, B. F. Smith, and H. Zhang. PETSc users manual. Technical Report ANL-95/11 - Revision 3.0.0, Argonne National Laboratory, 2008. Available at http://www.mcs.anl.gov/petsc/petsc-as/.

A. Barbagallo, D. Sipp, and P. J. Schmid. Closed-loop control of an open cavity flow using reduced-order models. *Journal of Fluid Mechanics*, 641: 1–50, 2009.

D. Barkley, M. G. M. Gomes, and R. D. Henderson. Three-dimensional instability in flow over a backward-facing step. *Journal of Fluid Mechanics*, 473, 2002.

J. Berland, C. Bogey, O. Marsden, and C. Bailly. High-order, low dispersive and low dissipative explicit schemes for multiple-scale and boundary problems. *Journal of Computational Physics*, 224(2):637–662, 2007.

C. Bogey and C. Bailly. Three-dimensional non-reflective boundary conditions for acoustic simulations: far field formulation and validation test cases. *Acta Acustica*, 88:463–471, 2002.

C. Bogey and C. Bailly. A family of low dispersive and low dissipative explicit schemes for flow and noise computations. *Journal of Computational Physics*, 194(1):194–214, 2004.

C. Bogey and C. Bailly. Computation of a high reynolds number jet and its radiated noise using large eddy simulation based on explicit filtering. *Computers and Fluids*, 35(10):1344–1358, 2006.

C. Bogey and C. Bailly. Influence of nozzle-exit boundary-layer conditions on the flow and acoustic fields of initially laminar jets. *Journal of Fluid Mechanics*, 663:507–538, 2010.

C. Bogey, S. Barré, V. Fleury, C. Bailly, and D. Juvé. Experimental study of the spectral properties of near-field and far-field jet noise. *International Journal of Aeroacoustics*, 6(2):73–92, 2007.

C. Bogey, O. Marsden, and C. Bailly. Large-eddy simulation of the flow and acoustic fields of a reynolds number 10[sup 5] subsonic jet with tripped exit boundary layers. *Physics of Fluids*, 23(3):035104, 2011.

B.-T. Chu. On the energy transfer to small disturbances in fluid flow (Part i). *Acta Mechanica*, 1(3):215–234, 1965.

C. Cossu and J. Chomaz. Global measures of local convective instabilities. *Physical Review Letters*, 78(23):4387–4390, 1997.

D. G. Crighton. Jet noise and the effects of jet forcing. In J. Jimenez, editor, *The Role of Coherent Structures in Modelling Turbulence and Mixing*, volume 136, pages 340–362. Springer Berlin Heidelberg, Berlin, Heidelberg, 1981.

D. G. Crighton and M. Gaster. Stability of slowly diverging jet flow. *Journal of Fluid Mechanics*, 77(02):397, 1976.

D. G. Crighton and P. Huerre. Shear-layer pressure fluctuations and superdirective acoustic sources. *Journal of Fluid Mechanics*, 220:355–368, 1990.

J. D. Crouch, A. Garbaruk, and D. Magidov. Predicting the onset of flow unsteadiness based on global instability. *Journal of Computational Physics*, 224(2):924–940, June 2007.

S. C. Crow and F. H. Champagne. Orderly structure in jet turbulence. *Journal of Fluid Mechanics*, 48(03):547, 1971.

T. A. Davis. UMFPACK version 5.5.0 user guide. Technical report, 2009. Available at http://www.cise.ufl.edu/research/sparse/umfpack/.

M. Fosas de Pando, D. Sipp, and P. J. Schmid. Efficient evaluation of the direct and adjoint linearized dynamics from compressible flow solvers. *submitted to Journal of Computational Physics*, 2012.

U. Ehrenstein and F. Gallaire. On two-dimensional temporal modes in spatially evolving open flows: the flat-plate boundary layer. *Journal of Fluid Mechanics*, 536:209–218, 2005.

B. F. Farrell and P. J. Ioannou. Stochastic forcing of the linearized Navier-Stokes equations. *Physics of Fluids A: Fluid Dynamics*, 5(11):2600, 1993.

J. B. Freund. Noise sources in a low-Reynolds-number turbulent jet at mach 0.9. *Journal of Fluid Mechanics*, 438:277–305, 2001.

N. J. Georgiadis and J. R. DeBonis. NavierStokes analysis methods for turbulent jet flows with application to aircraft exhaust nozzles. *Progress in Aerospace Sciences*, 42(5-6):377–418, 2006.

G. H. Golub and C. F. Van Loan. *Matrix computations, third edition*. The John Hopkins University Press, 1996.

J. M. Gordillo and M. Perez-Saborid. Transient effects in the signaling problem. *Physics of Fluids*, 14(12):4329, 2002.

K. Gudmundsson and T. Colonius. Parabolized stability equation models for turbulent jets and their radiated sound. *AIAA paper 2009-3380*, 2009.

K. Gudmundsson and T. Colonius. Instability wave models for the near-field fluctuations of turbulent jets. *Journal of Fluid Mechanics*, 689:97–128, 2011.

J.-L. Guermond, R. Pasquetti, and B. Popov. Entropy viscosity method for nonlinear conservation laws. *Journal of Computational Physics*, 230(11): 4248–4267, 2011.

E. Gutmark and C. M. Ho. Preferred modes and the spreading rates of jets. *Physics of Fluids*, 26(10):2932, 1983.

A. Hanifi, P. J. Schmid, and D. S. Henningson. Transient growth in compressible boundary layer flow. *Physics of Fluids*, 8(3):826–837, 1996.

C. J. Heaton, J. W. Nichols, and P. J. Schmid. Global linear stability of the non-parallel batchelor vortex. *Journal of Fluid Mechanics*, 629:139, 2009.

F. Hecht. Freefem++ manual, third edition, version 3.16-1. Technical report, 2011. Available at http://www.freefem.org/ff++.

T. Herbert. Parabolized stability equations. *Annual Review of Fluid Mechanics*, 29(1):245–283, 1997.

C. M. Ho and P. Huerre. Perturbed free shear layers. *Annual Review of Fluid Mechanics*, 16(1):365–422, 1984.

P. Huerre and P. A. Monkewitz. Absolute and convective instabilities in free shear layers. *Journal of Fluid Mechanics*, 159:151–168, 1985.

P. Huerre and P. A. Monkewitz. Local and global instabilities in spatially developing flows. *Annual Review of Fluid Mechanics*, 22:473–537, 1990.

Y. Hwang and C. Cossu. Linear non-normal energy amplification of harmonic and stochastic forcing in the turbulent channel flow. *Journal of Fluid Mechanics*, 664:51–73, 2010.

E. Johnsen and T. Colonius. Implementation of WENO schemes in compressible multicomponent flow problems. *Journal of Computational Physics*, 219 (2):715–732, December 2006.

S. A. Karabasov. Understanding jet noise. *Philosophical Transactions of the Royal Society A: Mathematical, Physical and Engineering Sciences*, 368 (1924):3593–3608, 2010.

V. Kibens. Discrete noise spectrum generated by acoustically excited jet. *AIAA Journal*, 18(4):434–441, 1980.

V. Kitsios, L. Cordier, J.-P. Bonnet, A. Ooi, and J. Soria. Development of a nonlinear eddy-viscosity closure for the triple-decomposition stability analysis of a turbulent channel. *Journal of Fluid Mechanics*, 664:74–107, October 2010.

J. Laufer and P. A. Monkewitz. On turbulent jet flows - a new perspective. *AIAA Paper. No. 80-0962*, 1980.

J. Laufer and T.-C. Yen. Noise generation by a low-Mach-number jet. *Journal of Fluid Mechanics*, 134(-1):1, 1983.

S. K. Lele. Compact finite difference schemes with spectral-like resolution. *Journal of Computational Physics*, 103(1):16–42, 1992.

L. Lesshafft. *Global modes and aerodynamic sound radiation in self-excited hot jets*. PhD thesis, Ecole Polytechnique, 2007.

L. Lesshafft, P. Huerre, P. Sagaut, and M. Terracol. Nonlinear global modes in hot jets. *Journal of Fluid Mechanics*, 554:393–409, 2006.

P. A. Lush. Measurements of subsonic jet noise and comparison with theory. *Journal of Fluid Mechanics*, 46(03):477, 1971.

C. J. Mack and P. J. Schmid. A preconditioned krylov technique for global hydrodynamic stability analysis of large-scale compressible flows. *Journal of Computational Physics*, 229(3):541–560, 2010.

C. J. Mack, P. J. Schmid, and J. L. Sesterhenn. Global stability of swept flow around a parabolic body: connecting attachment-line and crossflow modes. *Journal of Fluid Mechanics*, 611:205–214, 2008.

O. Marquet and D. Sipp. Global sustained perturbations in a backward-facing step flow. In *Seventh IUTAM Symposium on Laminar-Turbulent Transition*, 2010.

O. Marquet, D. Sipp, and L. Jacquin. Sensitivity analysis and passive control of cylinder flow. *Journal of Fluid Mechanics*, 615:221–252, 2008.

P. Meliga, J.-M. Chomaz, and D. Sipp. Global mode interaction and pattern selection in the wake of a disk: a weakly nonlinear expansion. *Journal of Fluid Mechanics*, 633:159, August 2009.

P. Meliga, D. Sipp, and J.-M. Chomaz. Effect of compressibility on the global stability of axisymmetric wake flows. *Journal of Fluid Mechanics*, 660:499–526, August 2010.

A. Michalke. On the inviscid instability of the hyperbolictangent velocity profile. *Journal of Fluid Mechanics*, 19(04):543, 1964.

A. Michalke. On spatially growing disturbances in an inviscid shear layer. *Journal of Fluid Mechanics*, 23(03):521, 1965.

A. Michalke. Instability of compressible circular free jet regarding influence of boundary layer thickness of a jet. *Zeitschrift fur flugwissenschaften*, 19 (8-9):319–328, 1971. English translation in NASA TM 75190, 1977.

A. Michalke. Survey on jet instability theory. *Progress in Aerospace Science*, 21:159–199, 1984.

P. A. Monkewitz. Feedback control of global oscillations in fluid systems. *AIAA Paper 89-0991*, 1989.

P. A. Monkewitz and K. Sohn. Absolute instability in hot jets. *AIAA Journal*, 26(8):911–916, August 1988.

A. Monokrousos, E. Akervik, L. Brandt, and D. S. Henningson. Global three-dimensional optimal disturbances in the blasius boundary-layer flow using time-steppers. *Journal of Fluid Mechanics*, 650:181, 2010.

C. J. Moore. The role of shear-layer instability waves in jet exhaust noise. *Journal of Fluid Mechanics*, 80(02):321, 1977.

J. W. Nichols and S. K. Lele. Global mode analysis of turbulent high-speed jets. Annual research briefs 2010, Center for Turbulence Research, 2010.

J. W. Nichols and S. K. Lele. Non-normal global modes of high-speed jets. *International Journal of Spray and Combustion Dynamics*, 3(4):285–302, 2011a.

J. W. Nichols and S. K. Lele. Global modes and transient response of a cold supersonic jet. *Journal of Fluid Mechanics*, 669:225–241, January 2011b.

R. Nong and D. C. Sorensen. A parameter free ADI-like method for the numerical solution of large scale lyapunov equations. Technical Report TR09-16, Rice University, 2009.

D. Obrist. Directivity of acoustic emissions from wave packets to the far field. *Journal of Fluid Mechanics*, 640:165, 2009.

D. E. Parekh, A. Leonard, and W. C. Reynolds. Bifurcating jets at high reynolds numbers. Technical Report TF-35, Department of Mechanical Engineering, Stanford University., 1988.

E. Piot, G. Casalis, F. Muller, and C. Bailly. Investigation of the PSE approach for subsonic and supersonic hot jets. detailed comparisons with LES and linearized euler equations results. *International Journal of Aeroacoustics*, 5(4):361–393, 2006.

P. Plaschko. Helical instabilities of slowly divergent jets. *Journal of Fluid Mechanics*, 92(02):209, 1979.

T. J. Poinsot and S. K. Lele. Boundary conditions for direct simulations of compressible viscous flows. *Journal of Computational Physics*, 101(1): 104–129, 1992.

R. R. Prasad and K. R. Sreenivasan. The measurement and interpretation of fractal dimensions of the scalar interface in turbulent flows. *Physics of Fluids A: Fluid Dynamics*, 2(5):792, 1990.

G. Pujals, M. Garcia-Villalba, C. Cossu, and S. Depardon. A note on optimal transient growth in turbulent channel flows. *Physics of Fluids*, 21(1): 015109, 2009.

P. K. Ray, L. C. Cheung, and S. K. Lele. On the growth and propagation of linear instability waves in compressible turbulent jets. *Physics of Fluids*, 21(5):054106, 2009.

R. Reba, S. Narayanan, and T. Colonius. Wave-packet models for large-scale mixing noise. *International Journal of Aeroacoustics*, 9(4):533–558, 2010.

S. C. Reddy and D. S. Henningson. Energy growth in viscous channel flows. *Journal of Fluid Mechanics*, 252(-1):209–238, 1993.

S. C. Reddy and L. N. Trefethen. Pseudospectra of the Convection-Diffusion operator. *SIAM Journal on Applied Mathematics*, 54(6):1634, 1994.

W. C. Reynolds and A.K.M.F. Hussain. The mechanics of an organized wave in turbulent shear flow. part 3. theoretical models and comparisons with experiments. *Journal of Fluid Mechanics*, 54(02):263, 1972.

D. Rodriguez, A. Samanta, A.V.G Cavalieri, T. Colonius, and P. Jordan. Parabolized stability equation models for predicting large-scale mixing noise of turbulent round jets. In *Proceedings of the 17th AIAA/CEAS Aeroacoustics Conference*, Portland, Oregon, 2011.

J. E. Roman, E. Romero, and A. Tomas. SLEPc users manual. Technical Report DSIC-II/24/02, Universidad Politecnica de Valencia, 2010. Available at http://www.grycap.upv.es/slepc.

R. D. Sandberg. Governing equations for a new compressible Navier-Stokes solver in general cylindrical coordinates. Technical Report AFM-07/07, University of Southampton, 2007. Available at http://eprints.soton.ac.uk/49523/.

R. D. Sandberg, N. D. Sandham, and V. Suponitsky. DNS of compressible pipe flow exiting into a coflow. *International Journal of Heat and Fluid Flow*, 2012.

H. Schlichting. *Boundary-layer theory*. McGraw-Hill, New York, 1955.

P. J. Schmid. Nonmodal stability theory. *Annual Review of Fluid Mechanics*, 39(1):129–162, 2007.

J. Sesterhenn. A characteristic-type formulation of the Navier-Stokes equations for high order upwind schemes. *Computers and Fluids*, 30(1):37 – 67, 2000.

Z. Sirkes and E. Tziperman. Finite difference of adjoint or adjoint of finite difference? *Monthly Weather Review*, 125(12):3373–3378, 1997.

K. Sohn. Absolute instability in hot jets. M. s. thesis, UCLA, 1986.

P. J. R. Strange and D. G. Crighton. Spinning modes on axisymmetric jets. part 1. *Journal of Fluid Mechanics*, 134(-1):231, 1983.

C. K. W. Tam and J. C. Webb. Dispersion-Relation-Preserving finite difference schemes for computational acoustics. *Journal of Computational Physics*, 107(2):262–281, 1993.

L. N. Trefethen and M. Embree. *Spectra And Pseudospectra: The Behavior of Nonnormal Matrices And Operators*. Princeton University Press, 2005.

L. N. Trefethen, A. E. Trefethen, S. C. Reddy, and T. A. Driscoll. Hydrodynamic stability without eigenvalues. *Science*, 261(5121):578–584, July 1993.

L. Tuckerman. Polar coordinates, available at http://www.pmmh.espci.fr/~laurette/explanatory.html, 2012.

H.C Yee, N.D Sandham, and M.J Djomehri. Low-Dissipative High-Order Shock-Capturing methods using Characteristic-Based filters. *Journal of Computational Physics*, 150:199–238, March 1999.